QUANTUM COHERENT TRANSPORT PHENOMENA IN EPITAXIAL HALIDE PEROVSKITE THIN FILMS

By

Liangji Zhang

A DISSERTATION

Submitted to
Michigan State University
in partial fulfillment of the requirements
for the degree of

Physics – Doctor of Philosophy

2022

ABSTRACT

QUANTUM COHERENT TRANSPORT PHENOMENA IN EPITAXIAL HALIDE PEROVSKITE THIN FILMS

By

Liangji Zhang

The subject of this dissertation is the experimental study of quantum coherent transport phenomena in epitaxial single-crystal halide perovskite thin films. The experiments consist of low-temperature (down to 10 mK) magnetotransport measurements at high magnetic field (up to 14 T).

The recent advent of epitaxial thin film growth of inorganic halide perovskites has made it possible to investigate the quantum behavior of charge carriers in these materials in low-dimensional form. We present results on epitaxial single-domain cesium tin iodide ($CsSnI_3$) thin films that clearly demonstrate quantum transport in this material for the first time. The observed low-field magnetoresistance shows signatures of weak anti-localization (WAL) that reveals coherent quantum interference effects and spin-orbit coupling. A micron-scale ($\approx 5\ \mu$m) low-temperature phase coherence length for charge carriers in the system is extracted from these WAL measurements.

Additionally, we present low-temperature quantum magnetotransport measurements on thin film devices made of epitaxial single-crystal $CsSnBr_3$, which exhibit two-dimensional Mott variable range hopping (VRH) and a large negative magnetoresistance. These findings are described by the Nguyen-Spivak-Shkovskii (NSS) model for quantum interference between different directed hopping paths, and we extract the temperature-dependent hopping length of charge carriers, their localization length, and a lower bound for their phase coherence length of $\sim$100 nm at low temperatures. These results from $CsSnI_3$ and $CsSnBr_3$ devices demonstrate that epitaxial halide perovskite devices are emerging as a material class for low-dimensional quantum coherent transport devices.

In addition to the works that are described above, I have also been involved in several additional projects, such as experiments on low-dimensional electron systems and superconducting qubit experiments, which will not be described in this dissertation.

This thesis is dedicated to the people who have supported me throughout my education.

ACKNOWLEDGMENTS

I am deeply grateful to my advisor Professor Johannes Pollanen for his remarkable mentorship during my entire graduate study. He brought me into the wonderful low-temperature quantum physics world. More importantly, he inspired and nurtured me to be a reliable, hardworking, and open-minded person, which I will never forget in the future. His encouragements and support helped me overcome every single barrier in my research and my daily life.

I would like to express gratitude towards Professor Richard Lunt, Professor Jia Leo Li, Professor Brian Skinner and Professor Norman Birge for their kind guidance and collaborations, which greatly broadened my knowledge and gave me a fruitful PhD life.

I would like to give a special thanks to Dr. Justin Lane, his help and wisdom always kept me away from the problems I met in my research, and he was always willing to help me out whenever I needed.

I would like to say thank you to Dr. Kostyantyn Nasyedkin and Dr. Niyaz Beysengulov for helping with my research. I will not forget the time we work together. It was really enjoyable. Thank you for passing your experience in physics to me.

I would like to say thank you Joe Kitzman for editing my dissertation. Your passion in physics always motivated me in the later days of my graduate study.

I would like to say thank you to Dr. Heejun Byeon for his guidance in helping me the graduate course study and giving me valuable advice in my life.

I am grateful to all LHQS group colleagues, Camille Mikolas, Austin Schleusner, Camryn Undershute, Dr. Mazin Khasawneh and all others. Thank you for your help — I am really glad that I got to work with you. I will also not forget to thank the wonderful staff members in the physics department who help the LHQSers, Dr. Baokang Bi, Dr. Reza Loloee, Kim Crosslan, Cathy Cords and Jessica Cords.

Moreover, I will say thank you to my committee members, Professor Carlo Piermarocchi, Professor Marcos Caballero, Professor Tyler Cocker and Professor Kirsten Tollefson for your

careful guidance and support.

Last, I would like to thank my parents for always supporting me in my life. Finally, I would like to thank Yan Cong, for your endless support and company.

The projects described in this dissertation were supported by: the National Science Foundation under grant number DMR-1807573, the Cowen Family Endowment, and the Center for Integrated Nanotechnologies at Sandia National Laboratory.

TABLE OF CONTENTS

LIST OF TABLES

LIST OF FIGURES

CHAPTER 1

INTRODUCTION: TRANSPORT IN TWO-DIMENSIONAL ELECTRON SYSTEMS

1.1 Motivation of this Dissertation

The systematic study of electrons in low-dimensional systems and their collective behavior is one of the most active and interesting topics in condensed matter physics. Two-dimensional electron systems (2DESs), in which electrons are free to move in two spatial dimensions but tightly confined in the third, have been realized in a wide variety of different high-quality materials. Examples of these materials include gallium arsenide/aluminum gallium arsenide (GaAs/AlGaAs) heterostructures [85], zinc oxide (ZnO/ZnMgO) heterostructures [63], metal-oxide-semiconductor field-effect transistors (MOSFET) in silicon [100], graphene [35] and electrons floating on the surface of liquid helium [2]. Numerous intriguing physical phenomena have been realized in these 2DESs when a large magnetic field is applied to these systems at low temperatures. These phenomena include quantum interference driven localization [37], quantum oscillations [26], as well as various quantum Hall effects (QHE) [19]. Ultimately these phenomena and their classic signatures in electrical and magnetotransport experiments are keys to understanding the underlying quantum-mechanical behavior of electrons confined to these low-dimensional systems.

Halide perovskites, which have emerged over the past decade as a fundamentally intriguing class of semiconductors, with a wide variety of potential applications, offer a new material platform for the study of 2DESs. However most work to-date has been performed with bulk crystals or polycrystalline thin film halide perovskite samples. Extending these studies to the low-temperature quantum properties of halide perovskite 2DESs has been limited by the ability to grow high quality thin films. Additionally, as we know from the case of graphene, which consists of a single layer of carbon atoms that come from exfoliating graphite, “high-quality" two-dimensional layers often show exotic physics different from their parent materials. To overcome the limitation of material imperfections such as grain boundaries and ionic defects common in conventional solution-

processed polycrystalline halide perovskites, single-crystal epitaxial growth of halide perovskites has been recently introduced [130, 129] and opens the door to investigate 2DES in this material class for the first time.

This dissertation focuses on low-temperature and high-magnetic field electrical transport measurements on these new types of epitaxial halide perovskite devices. The measurements reveal clear signatures of quantum coherent charge carrier transport in these materials at low temperature, and open the door to future quantum experiments and devices based on epitaxial halide perovskite and their potential as next generation 2DES materials.

1.2 Organization of this Dissertation

Chapter 1 (this chapter) gives a brief road map of the fundamental physical concepts associated with quantum transport and serves to provide motivation for the work described in the following chapters. This chapter describes the most striking phenomena observed in our halide perovskite devices, namely the coherent diffusive and hopping transport of charge carriers in these materials. Additionally this chapter will introduce the integer quantum Hall effect (IQHE) and the fractional quantum Hall effect (FQHE), which serve to motivate possible future 2DES physics that may one day be investigated in halide perovskite as material quality continues to improve.

Chapter 2 focuses on the epitaxial growth, crystal structure and air-sensitive nature of epitaxial single-crystal halide perovskites thin film devices used in our experiments. Additionally, various characterization methods for the thin film samples will be described.

Chapter 3 describes the measurement setup and experimental techniques used to perform low-temperature magnetotransport measurements on the thin film devices. These include low-frequency lock-in-based AC transport measurements, halide perovskite device wire-up and how to keep halide perovskite devices from structurally degrading in air under ambient conditions. A general introduction to dilution refrigeration, needed to achieve milli-Kelvin (mK) temperatures, as well as the operation of a superconducting high-field magnet will also be presented.

Chapter 4 details results demonstrating quantum interference and quantum diffusive transport

of charges in quasi-2D halide perovskites. Specifically, a comprehensive discussion of weak localization (WL) and weak anti-localization (WAL) will be given in this chapter to explain the quantum coherent transport observed in thin film epitaxial single-crystal cesium tin iodide ($CsSnI_3$) devices. Much of this chapter is based on the results presented in the following paper, *Extraordinary phase coherence length in epitaxial halide perovskites, iScience*, **24**, 102912 (2021) [94].

Chapter 5 focuses on results of coherent transport in another halide perovskite compound. In particular this chapter will discuss variable range hopping (VRH) transport and the Nguyen-Spivak-Shkovskii (NSS) model to explain the observed giant negative magnetoresistance in thin film epitaxial single-crystal cesium tin bromide ($CsSnBr_3$) devices. Much of this chapter will cover the results presented in the following article, *Coherent Hopping Transport and Giant Negative Magnetoresistance in Epitaxial $CsSnBr_3$, ACS Applied Electronic Materials*, **3**, 2948 (2021) [135].

Finally, Chapter 6 will summarize the main results of this thesis work and emphasize their context in the landscape of quantum coherent transport measurements on 2DESs. Additionally, several potential future directions of research on epitaxial halide perovskites will be provided.

1.3 Fundamental Concepts

This section reviews some fundamental concepts associated with low-dimensional semiconductors and electrical transport in the presence of a magnetic field. Understanding these concepts and the related physics will be key for providing context for our present and future experiments with halide perovskites. Moreover, knowledge of these concepts will also lay the ground work for understanding the low-dimensional systems based on halide perovskites in this dissertation.

1.3.1 Band Structure and Doping

In this subsection, we will briefly describe the electronic band structure of solids and doping of semiconductors, and then focus on some properties unique to 2D semiconductors. This is motivated by the fact that the epitaxial single-crystal halide perovskite thin films we work with are intrinsic semiconductors that can be doped with charge carriers to reveal a variety of transport phenomena.

Going beyond this brief introduction, a more detailed discussion of the physics of semiconductors can be found in Refs. [19, 59].

We will first start with one of the most important concepts in semiconductors, which is Fermi level, denoted as μ. This quantity describes the top of the collection of electron energy levels in a solid. Because the Pauli exclusion principle for fermions restricts the occupation number of a state to be either zero or one, then the average occupation for a state with energy E is governed by the Fermi-Dirac distribution function $f(E)$, which is given by [59]:

$$f(E) = \frac{1}{1 + \exp\left(\frac{E-\mu}{k_B T}\right)}, \tag{1.1}$$

where k_B is the Boltzmann constant and T is the temperature.

In the band theory of solids, the conductor, semiconductor, and insulator are often distinguished from each other by plotting the available, or unavailable, energy bands for electrons in these materials [59]. These energy bands are separated by gaps in energy for which no wave-like electron orbitals exist. Such forbidden regions are referred to as band gaps. At $T = 0$ K in a semiconductor (or an insulator), the Fermi level resides in such a band gap (see Figure 1.1 (a)). The difference between a semiconductor, an insulator, and a metal is that a semiconductor has a relatively small band gap compared with an insulator, whereas a metal has no band gap at all.

In an undoped semiconductor at absolute zero, the band below the band gap (and Fermi level) is called the valence band, and all the states in this band are filled with charge carriers, and the top of the valence band is denoted E_v in Figure 1.1 (a). The band of electron states above band gap is called the conduction band and, in the absence of charge doping, it is completely vacant. The bottom of the conduction band will be denoted E_c and therefore the magnitude of band gap is $E_G = E_c - E_v$ [59].

Of particular interest to our work with halide perovskites is the behavior of the semiconductor, because in their pure form these materials are intrinsic (or undoped) semiconductors. The electrical properties of an intrinsic semiconductor can be greatly modified with the incorporation of impurities or vacancies into their crystal structure via a process called doping, which is used to

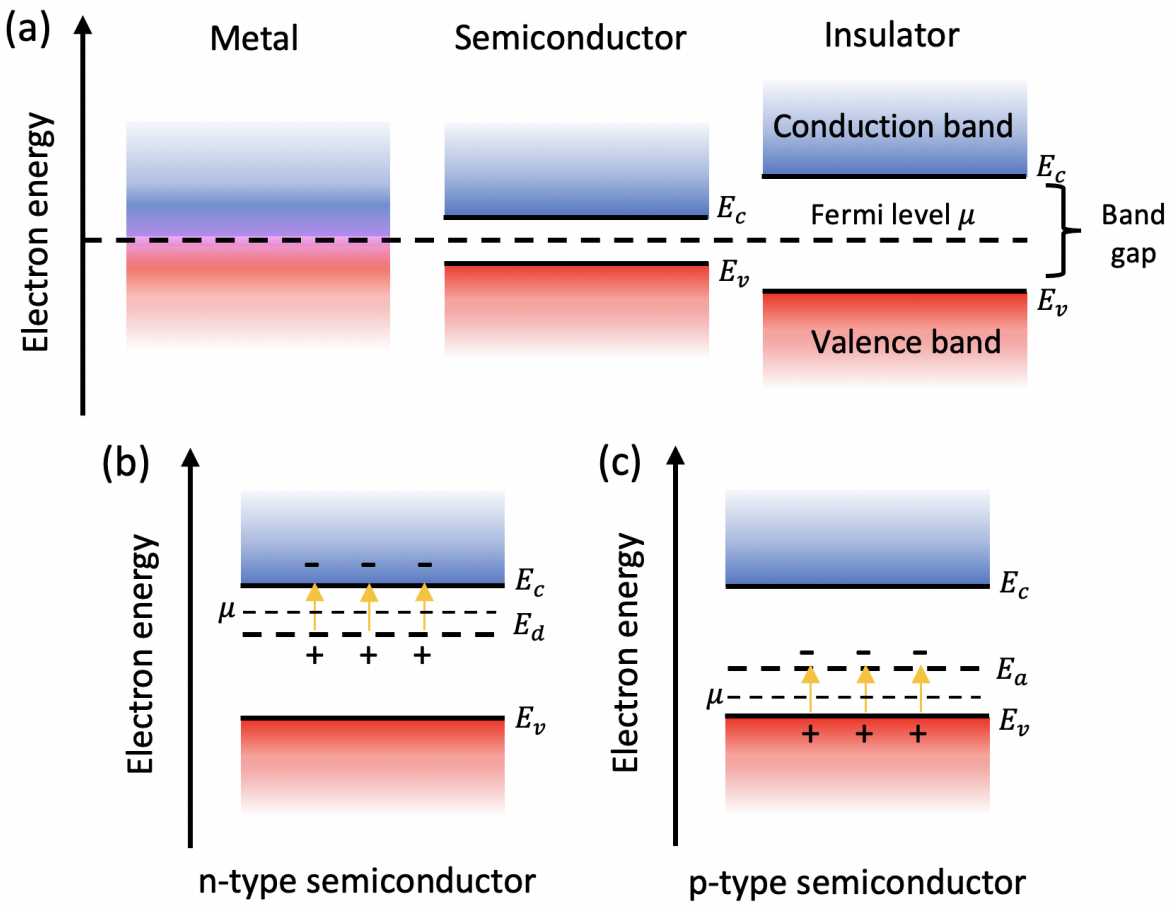

Figure 1.1: (a) Schematic band structures of a metal, semiconductor, and insulator in the absence of doping. (b) Band structure of n-type semiconductor. (c) Band structure of p-type semiconductor. E_c, E_v, μ, E_d and E_a are the bottom of the conduction band, the top of the valence band, the Fermi level, the energy level of the donor dopants E_d and the energy level of the acceptor dopants E_a respectively.

change the concentration of free charge carriers in the system. Adding, either intentionally or not, different types of dopants can produce different effects on the electrical behavior of semiconductors. Specifically, so-called "donor" impurities or dopants are elements which give additional electrons to the material. In this case, electrical current carriers are negatively charged and the semiconductor is called an n-type semiconductor (see Figure 1.1 (b)). Common examples of the donor dopants in the semiconductor silicon are phosphorus, arsenic, antimony, and lithium. A second class of dopant acts as an "acceptor" and removes electrons from the material. Semiconductors with acceptors as dopants are called p-type and charge carriers in these materials are positively charged holes

(see Figure 1.1 (c)). The common examples of acceptor dopants in silicon are boron, aluminum, gallium, and indium. A schematic figure of the band structures of doped semiconductors is shown in Figure 1.1 (b) and (c), which show that in n-type materials there are electron energy levels of the donor dopants E_d near the top of the band gap that can be relatively easily excited into the conduction band, for example, by thermal energy or light [19]. In a p-type material on the other hand, excess "holes" can be excited into the valence band (from the energy level of the acceptor dopants E_a) to create mobile positive charge carriers in the material [19].

The properties of semiconductors are also strongly affected by their dimensionality and because the halide perovskite materials we will be discussing in this dissertation are thin films we will now introduce some relevant properties of two-dimensional (2D) semiconductors. We will begin by describing the density of states (DOS) $g_{2D}(E)$ of the 2D semiconductor, which we will model as an infinite quantum well in the direction normal to the 2D plane. In this model the DOS is given by [111]:

$$g_{2D}(E) = \frac{m^*}{\pi\hbar^2}, \tag{1.2}$$

where m^* is the electron effective mass and $\hbar$ is the reduced Planck's constant. Equation 1.2 shows that the DOS in 2D is independent of the energy. Additionally, the Fermi level μ in a 2D semiconductor can be controlled by varying the areal charge carrier density (e.g. via doping or electrostatic gating). In particular, the density dependence of the Fermi level is given by [111]:

$$\mu(n) = \frac{\hbar^2\pi n}{m^*}, \tag{1.3}$$

where n is the 2D charge carrier density. As we will see, these quantities will be of relevance when discussing the QHE in Subsection 2.2.3 as well as for understanding the role of charge carrier doping in our halide perovskite semiconducting samples.

1.3.2 Conductivity and Resistivity in Two Dimensions

Before discussing the quantum mechanical transport behavior of 2DESs in a magnetic field, it is important to briefly discuss the classical current flow in a 2DES. According to the Drude

model[1][23], in classical magnetotransport, Ohm's law is:

$$\vec{j} = \hat{\sigma}\vec{E}\,, \tag{1.4}$$

where the electrical conductivity $\hat{\sigma}$ in Ohm's law is a tensor in the most general case, $\vec{j}$ and $\vec{E}$ are current density and electric field. In a 2D system in the xy-plane with a magnetic field $\vec{B}$ along the z-axis, the conductivity tensor $\hat{\sigma}$ of the system is [19]:

$$\hat{\sigma} = \begin{pmatrix} \sigma_{xx} & \sigma_{xy} \\ -\sigma_{xy} & \sigma_{xx} \end{pmatrix} = \frac{\sigma_0}{1+\omega_B^2\tau^2} \begin{pmatrix} 1 & \omega_B\tau \\ -\omega_B\tau & 1 \end{pmatrix}. \tag{1.5}$$

In Equation 1.5, $\sigma_0 = \frac{ne^2\tau}{m^*}$ is the DC Drude conductivity in the absence of the magnetic field, $\omega_B = \frac{eB}{m^*}$ is the classical cyclotron frequency, n is the number of charge carriers per unit area, τ is their average scattering relaxation time and e is the elementary charge. The resistivity tensor is the inverse of the conductivity tensor, so it can be written as:

$$\hat{\rho} = \hat{\sigma}^{-1} = \begin{pmatrix} \rho_{xx} & \rho_{xy} \\ -\rho_{xy} & \rho_{xx} \end{pmatrix} = \frac{1}{\sigma_0} \begin{pmatrix} 1 & \omega_B\tau \\ -\omega_B\tau & 1 \end{pmatrix}. \tag{1.6}$$

In Equation 1.5 and 1.6, σ_{xx} and σ_{xy} are respectively, the longitudinal and transverse (or Hall) conductivities. Similarly, ρ_{xx} and ρ_{xy} are referred to as longitudinal and transverse (or Hall) resistivities. To obtain all of these tensor components from measurements, 2DES samples are often fabricated in a Hall bar geometry (see Figure 1.2). The resistivity components ρ_{xx} and ρ_{xy} can be derived from measured values of the longitudinal and transverse voltages V_{xx} and V_{xy}:

$$\rho_{xx} = \left(\frac{W}{L}\right)\frac{V_{xx}}{I}\,,\ R_{xx} = \frac{V_{xx}}{I} \tag{1.7}$$

$$\rho_{xy} = R_{xy} = \frac{V_{xy}}{I}, \tag{1.8}$$

where R_{xx} and R_{xy} are the longitudinal and transverse (Hall) resistances, and L and W are the length and width of the sample, and I is the current that flows through the sample. As can be seen

[1]For a detailed description of the Drude model and its limitations, see Section 4.2

from the expressions above, in two dimensions, the resistance R and resistivity ρ both have units of Ω. The tensor components of the conductivity can then be derived from the resistivities as:

$$\sigma_{xx} = \frac{\rho_{xx}}{\rho_{xx}^2 + \rho_{xy}^2} \quad ; \quad \sigma_{xy} = \frac{\rho_{xy}}{\rho_{xx}^2 + \rho_{xy}^2}, \tag{1.9}$$

where σ_{xx} and σ_{xy} have units of $1/\Omega$.

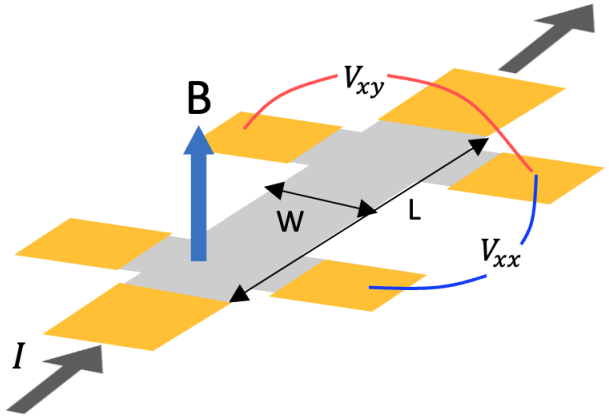

Figure 1.2: A 2D device in a Hall bar geometry of length L and width W. The applied external magnetic field B is normal to sample surface (grey area). V_{xx} and V_{xy} are the longitudinal and transverse (or Hall) voltages which develop when a current I is passed through the sample between contacts (gold areas). I is the current that passes through the device.

1.4 Quantum Effects in Two-Dimensional Electron Systems (2DESs)

In high-quality 2DESs, as the amount of disorder and impurities is reduced, a wide variety of quantum coherent and electron-electron interaction induced effects begin to reveal themselves. Below we have listed some of these that we have observed in our halide perovskite thin film devices as well as some that we hope to observe in the future as material quality continues to improve.

1.4.1 Coherent Transport in the Quantum Diffusive Regime

In a 2D system with a relatively high level of disorder, electrons (or holes) move semi-classically and the system is in the quantum diffusive transport regime. In this regime the phase coherence length

of the electron wavefunction is greater than the mean free path of the electron between elastic scattering events. The electrons travel and collide elastically with randomly located impurities within the crystal and due to the quantum mechanical nature of phase coherence, the probability of the electron which returns to its origin essentially gets double-counted in a phenomenon known as weak localization (WL) [10]. If spin-orbit coupling is present in the system, the interference is destructive in nature and leads to a phenomenon referred to as weak anti-localization (WAL). The physics of these quantum coherent localization effects will be discussed in more detail in Chapter 4 where we will present results demonstrating WAL in epitaxial single-crystal $CsSnI_3$ thin films.

1.4.2 Coherent Hopping Transport

By decreasing the overall charge carrier concentration one can transition from 2D quantum diffusive transport to a regime in which electrons move via quantum mechanical tunneling between otherwise disconnected and localized impurity states. This type of transport is typically referred to as "hopping" transport. When electron-electron interactions can be ignored systems in this regime of transport show so-called 2D Mott variable range hopping (VRH) where the electron is transported by phonon-assisted hopping (tunneling) between localized states. When the electron's phase coherence length is comparable with the hopping length, coherent hopping transport along different hopping trajectories can be revealed in the form of a large negative magnetoresistance. The physics of this type of coherent hopping transport will be discussed in more detail in Chapter 5 where we will present results demonstrating clear signatures of its presence in epitaxial single-crystal $CsSnBr_3$ thin films.

1.4.3 Integer Quantum Hall Effect

As material quality and device control continues to improve, additional phenomena can be expected at low temperatures and high magnetic fields. Among these phenomena the Integer Quantum Hall Effect (IQHE) draws our attention because the IQHE was one of the initial drivers of our interest in researching 2DES based on epitaxial single-crystal halide perovskites thin films. While the

appearance of quantum oscillations and the formation of Landau levels has yet to be observed in the these materials it remains and interesting prospect for future research. In this section, we will give an introduction to the IQHE and how it can be realized in system with sufficiently low disorder level.

1.4.3.1 Landau Quantization

In the following, we will discuss Landau quantization, which is the quantization of the energy and cyclotron orbits of charge carriers in high-quality 2DES at low temperatures and when the system is subjected to a large external magnetic field. Landau quantization is the key to explain the observed quantized Hall resistance in the IQHE.

If we do not consider the spin of the charge carrier, the Hamiltonian of a single electron confined to 2D in a perpendicular magnetic field is:

$$\hat{H} = \frac{1}{2m}\left|\hat{p} + e\hat{A}\right|^2, \quad \hat{A} = By\hat{x}, \tag{1.10}$$

where $\hat{A}$ is the vector potential in the Landau gauge [66], and the magnetic field $\hat{B} = \nabla \times \hat{A}$. If we choose an in-plane momentum state k_x we can construct the electron wavefunction as:

$$\psi(x, y) = \exp(ik_x x)Y(y). \tag{1.11}$$

If we apply Equation 1.11 and Equation 1.10 to the Schrodinger equation $\hat{H}\psi = E\psi$, we obtain:

$$\frac{1}{2m}\left[-\hbar^2\frac{\mathrm{d}^2}{\mathrm{d}y^2} + (eB)^2\left(y - \frac{\hbar k_x}{eB}\right)^2\right]Y = EY. \tag{1.12}$$

Equation 1.12 represents the Schrodinger equation for a one-dimensional harmonic oscillator having a frequency ω_c and center $y_0 = \frac{\hbar k_x}{eB}$. The DOS of the electron system collapses from a constant versus energy (see Equation 1.2) to a series of Dirac δ-functions corresponding to Landau levels. The eigenenergies of these Landau levels are [66]:

$$E_n = \hbar\omega_c\left(n + \frac{1}{2}\right), \quad n = 1, 2, 3\cdots. \tag{1.13}$$

The frequency of the orbital motion ω_c is the cyclotron frequency:

$$\omega_c = \frac{eB}{m}, \tag{1.14}$$

and the center y_0 is related to the magnetic length l_B (see Equation 1.15), which is the characteristic length scale associated with the electron in this model.

$$y_0 = \frac{\hbar k_x}{eB} = k_x l_B^2, \quad l_B = \sqrt{\frac{\hbar}{eB}}\ . \tag{1.15}$$

1.4.3.2 Localized States and Extended States

In the previous subsection we did not take into account the effect of disorder on the formation of Landau levels or on the 2DES in general. However, as we will see throughout this thesis, disorder is present, to one extent or another, in all of the real physical systems used to realize 2DESs. We will start with a discussion of "localized" states because disorder can lead to spatial fluctuations in the electron density and the formation of a spatially varying potential landscape throughout the area of the 2DES. The localized states, which were originally introduced by Philip W. Anderson [1] are states whose wave functions are mostly located in a confined region of space that is produced by a short-range potential. Outside of this region, the envelope of the wave function decays exponentially, and adjacent localized states are not overlapping with each other. In contrast, "extended" states are states in which charge carriers may be found anywhere within a relatively large region in a material and the charge carrier wavefunctions are largely delocalized.

In a real 2DES material system one will typically have a coexistence of localized and extended states whose spatial distribution is determined by the disorder potential. The general idea is if we apply magnetic field to spin-less 2DES, the continuum of states that exists in zero field quantizes into Landau levels. In the presence of disorder, these Landau levels are broadened and they can be divided into two categories. The states close to the center of the Landau levels are extended states, and they can carry electrical current macroscopically across the 2DES. The states that are on the tails of the Landau levels are localized states (see Figure 1.3). These localized states do not carry

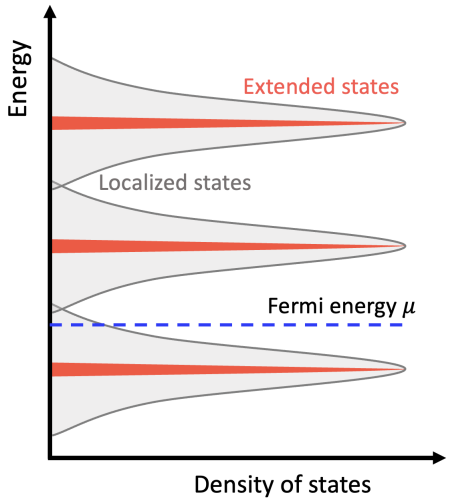

Figure 1.3: The disorder broadened DOS of a 2DES in a strong magnetic field. The extended states are depicted in red at the center of the Landau levels which can carry current, and the localized states are shown in gray which cannot carry current.

current across the sample at zero temperature and correspond to electrons that are spatially trapped due to the underlying disorder potential.

1.4.3.3 Edge States and the Integer Quantum Hall Effect

In this section, we will discuss how the formation of Landau levels can be observed in the IQHE, and the role of localized states (produced by disorder) on this effect. The discussion of the IQHE in this section is based on measurements from a gallium arsenide/aluminum gallium arsenide (GaAs/AlGaAs) heterostructure and a bi-layer graphene (BLG) device [2].

Integer Quantum Hall Effect (IQHE) is a "single electron" phenomenon, i.e. electron-electron interactions do not, in principle, play a role. As discussed previously, when the externally applied magnetic field is normal to the plane of the 2DES, the DOS of the 2DES becomes quantized. Semi-classically one can think of the electrons in the 2DES as moving in circles around the field

[2]The GaAs/AlGaAs heterostructure and BLG device data presented here are from early experiments in this Ph.D. to characterize the experimental system and techniques as well as experiments investigating the role of high-frequency and microwave absorption in BLG. A more detailed description of the experiments on BLG are presented in Appendix A.

direction. Close to the edge of the sample, the electrons collide with the boundary (see Figure 1.4). The confinement provided by the edge of the 2DES in the y-direction (here the y-direction is normal to the current flow which is along the x-direction, as shown in 1.4) can be treated as a hard wall potential $V(y)$. If we present the Landau levels as a function of the y-position across the sample as shown in Figure 1.5, the potential $V(y)$ raises the energy of the Landau level steeply at the 2DES's edge since the electrons cannot leave the sample. The Landau level energy near the edge will be $E_n = \hbar\omega_c \left(n + \frac{1}{2}\right) + V(y)$. Depending on the density of electrons and the magnetic field, some Landau levels will cross the Fermi energy leading to current carrying edge channels. The bulk of the 2DES, in contrast, will be an insulator because all the states in the interior band are filled and the Fermi level is in a gap between well separated Landau levels.

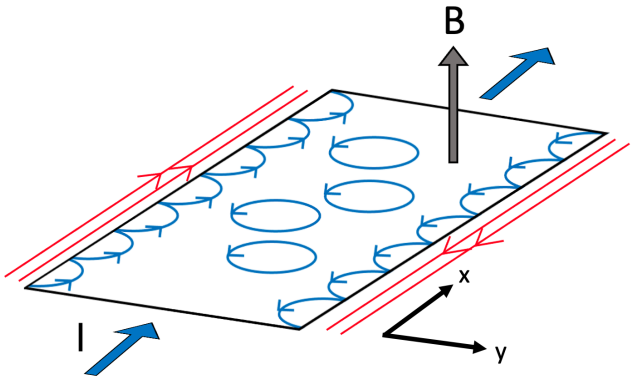

Figure 1.4: Semi-classical illustration of the IQHE edge states in a 2DES. The applied magnetic field B is normal to 2DES. At each edge, two current carrying edge channels (red lines) originate from the crossing of the Fermi level and two Landau levels as shown in Figure 1.5.

Furthermore, these edge states carry current in a chiral fashion. If we inspect the direction of the electron flow shown in Figure 1.4, the motion of each electron is counterclockwise as dictated by the field. When an electron hits the edge of the sample, it produces a skipping motion in which it moves along the edge in only a single direction. These skipping trajectories are the edge channels described above. The number of edge channels is determined by the number of crossings between the Landau levels and Fermi level at each edge (see Figure 1.5). The bulk of the 2DES is an insulator as the electrons in it will perform cyclotron motion without in a particular direction along

the sample. Additionally, the electrons have opposite direction on the two edges of the sample because they have the same chirality. This ensures the net current through the system is zero when no external electric field applied.

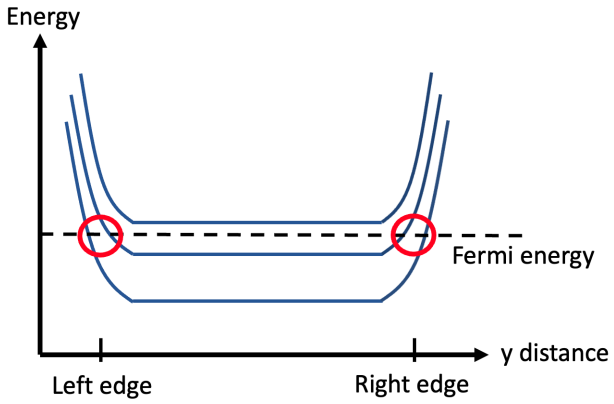

Figure 1.5: Illustration of Landau level energy versus distance in y-direction of the sample. The energy of the Landau levels rises due to the confinement at the edges of the sample. Red circles indicate the crossings between the Fermi level and the Landau levels, which produces current carrying chiral edge states (two edge states are present in this example).

The formation of Landau levels and edge states in the 2DES leads to the IQHE and a quantized value of the Hall resistance. In Figure 1.6 (a), we present data of the longitudinal resistance R_{xx} and Hall resistance R_{xy} of a GaAs/AlGaAs 2DES as a function of the applied magnetic field at $T = 12$ mK. In this figure, R_{xy} takes on quantized values:

$$R_{xy} = \frac{h}{e^2}\left(\frac{1}{\nu}\right), \quad \nu = \pm 1, \pm 2, \pm 3 \cdots . \tag{1.16}$$

The Landau level filling factor ν counts the number of conducting edge states and it has been measured to be integer values with extraordinary accuracy (one part in 10^9) [61, 122]. The quantity $\frac{h}{e^2}$ is called the quantum of resistance, and it is now used as the metrological standard of resistance [61]. The centers of the plateaus in R_{xy} occur at the following values of the magnetic field:

$$B = \frac{n}{\nu}\left(\frac{h}{e}\right) = \frac{n}{\nu}\Phi_0 \,, \tag{1.17}$$

where n the electron density and $\Phi_0 = \frac{h}{e}$ is the flux quantum. We also observe the dissipationless transport of electricity by the edge states in the system when $R_{xx} = 0$ and R_{xy} indicates integer

Landau level filling. As shown in Figure 1.6 (a), there is a marked increase of R_{xx} as the magnetic field moves a Landau level through the Fermi level as shown in Figure 1.6 (b) and (c). When R_{xy} corresponds to a quantized plateau, electrons prefer to travel along closed equipotential lines that enclose small potential valleys produced by disorder corresponding to localized states in the bulk of the 2DES. These bulk regions are not connected to the edge and do not contribute to the measured current. Consequently, R_{xx} remains zero and R_{xy} remains unchanged despite the change of the magnetic field B. If we keep decreasing the magnetic field to the region labeled A shown in Figure 1.6 (b), the size of potential valley increases as the Fermi level μ enters an extended state (see Figure 1.6 (b)). At some point, a potential valley connects both edges of the 2DES, as shown in Figure 1.6 (d), and an electron injected from the left may travel across the sample along an edge state [36]. Due to the chirality of the transport, the electron will backscatter to the left contact, causing an increase in the longitudinal resistance. Meanwhile, the Hall resistance R_{xy} will no longer be quantized but "jump" to the next (lower) plateau, a situation called a plateau transition.

An additional example of the IQHE is presented in Figure 1.7 (a) for the case of bi-layer graphene (BLG) (see Appendix A). In this figure, we plot the longitudinal conductivity σ_{xx} and the Hall conductivity σ_{xy} (in units of $\frac{h}{e^2}$) as a function of gate voltage V_T at a fixed magnetic field of $B = 13.2$ T. Two integer plateaus $\nu = -1$ and $\nu = -2$ can be observed by controlling V_T, which is equivalent to controlling the overall electron density n in the 2DES (see Equation 1.17), which is equivalent to controlling the Fermi level μ (see Equation 1.3).

1.4.4 Fractional Quantum Hall Effect and Composite Fermions

As the material quality reaches its highest level, with the least amount of defects and impurities, the potentials introduced by disorder no longer dominate the behavior of electrons in the 2DES and one can hope to observe the collective phenomena induced by Coulomb interactions between the charge carriers in the 2D system. One of these phenomena, which we will discuss in the following, is the fractional quantum Hall effect (FQHE), which in certain situations can be explained by the formation of quasi-particles called composite fermions (CFs).

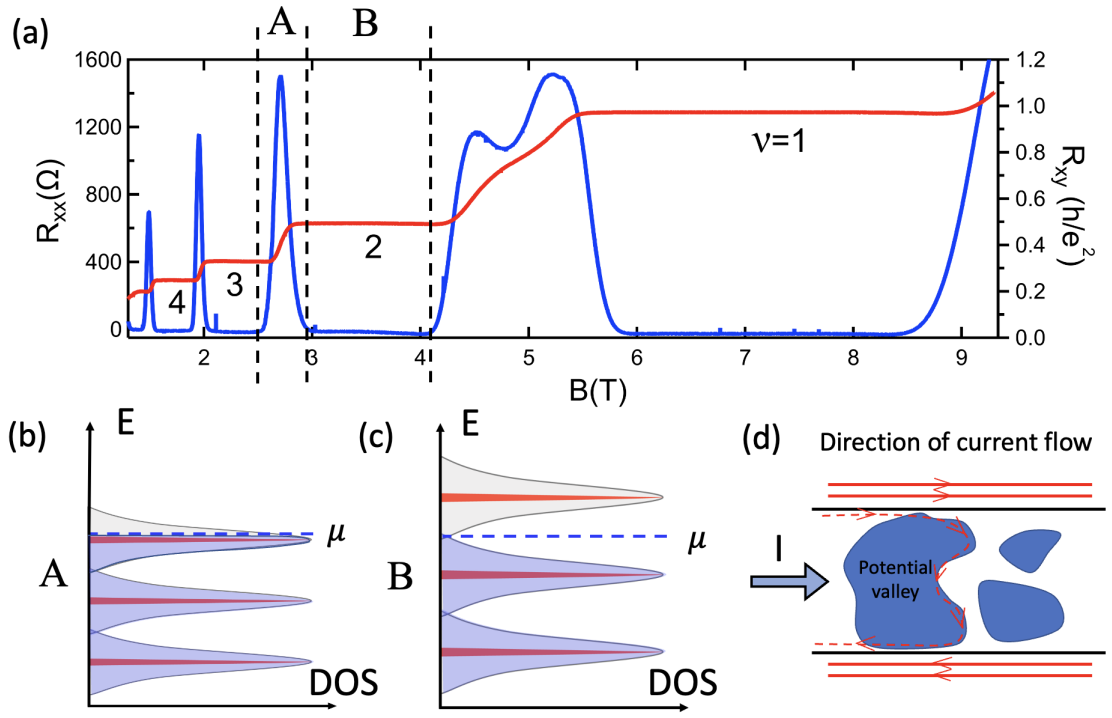

Figure 1.6: (a) IQHE data from a GaAs/AlGaAs heterostructure at $T = 12$ mK. Each plateau (indicated by Landau filling factors) in the Hall resistance R_{xy} is accompanied by a vanishing longitudinal resistance R_{xx} (blue). The values of R_{xy} (red) in this figure are in units of $\frac{h}{e^2}$, where $\frac{h}{e^2} \simeq 25812\ \Omega$. (b) and (c) DOS diagram corresponding to regions A and B in panel (a) of this figure. (d) The direction of electron flow in the 2DES.

Our discussion of the FQHE will be presented in the context of our early measurements on high-quality BLG devices (for additional details see Appendix A). The IQHE discussed in the previous subsection can be used to explain the origin of integer plateaus such as those shown at $\nu = -1, -2$ in Figure 1.7 (a). However, the features near $V_T = -0.4$ V (see 1.7 (b)) cannot be easily understood in the context of the IQHE. In Figure 1.7 (b) we see small plateaus at fractional values of ν (i.e. $\nu = -\frac{1}{3}, -\frac{2}{5}, -\frac{3}{5}, -\frac{2}{3}$ and so on) centered around $\nu = -\frac{1}{2}$. All of the features are examples of the FQHE, which was first observed in GaAs heterostructure by Stormer and Tsui [124] and theoretically explained by Laughlin [70]. As discussed previously, the IQHE can be understood by considering free electrons. In contrast, to explain the FQHE, one need to take interactions between electrons into account. This makes the problem much more challenging but also much

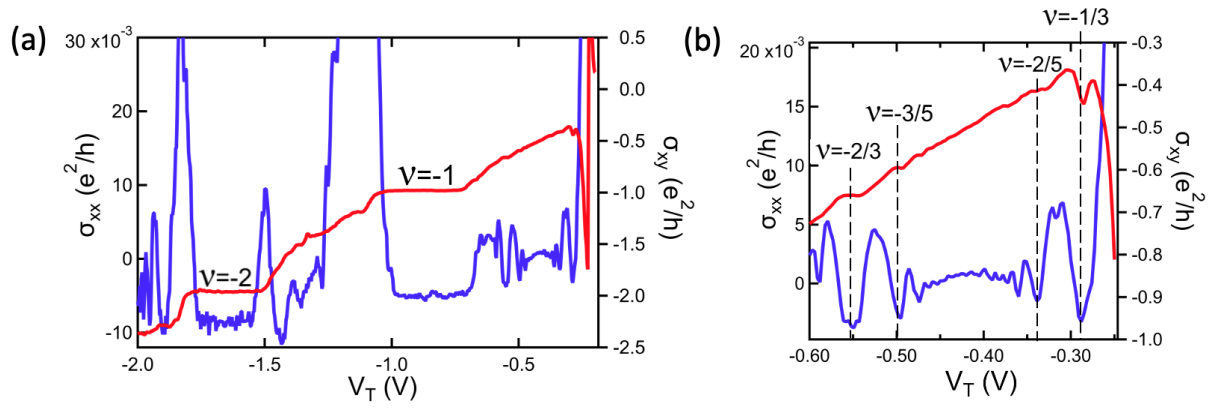

Figure 1.7: IQHE and FQHE data of tBLG device. Both σ_{xx} and σ_{xy} data are in $\frac{e^2}{h}$ units (see Equation 1.9). The data is taken when the device temperature is at 13 mK. The contact gate voltage $V_c = -4V$ reduces the contact resistance. Bottom gate voltage $V_B = 0V$. (a) $-2V \leq V_T \leq -0.25V$, the IQHE is observed. (b) Same data trace as in (a) but zoomed in at $-0.6V \leq V_T \leq -0.2V$, where the FQHE is observed.

more intriguing.

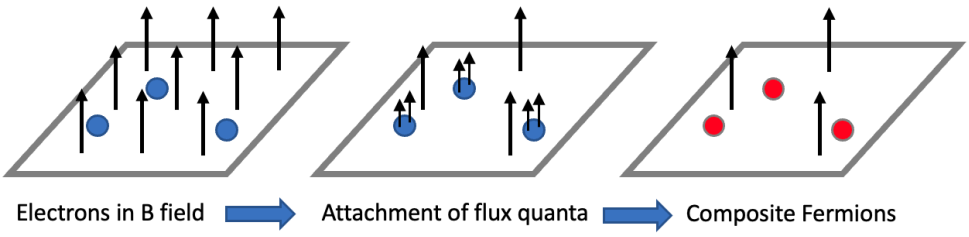

Figure 1.8: Transformation of electrons in a magnetic field into CFs in an effective field [123].

The fractional filling factors in the FQHE can be explained using the composite fermion (CF) model, developed by Jainendra Jain [51]. The premise of this model is the concept of the CF, in which electrons combine with flux quanta to create quasiparticles. The FQHE can largely be understood as the IQHE of CFs. Figure 1.8 is a set of schematic diagrams to show conceptually how CFs are formed. In a 2DES subject to an external magnetic field, as the field moves the Fermi level below the lowest Landau level $\nu = 1$, each electron (blue dot) will "absorb" two flux quanta (up arrows) and form a CF (red dot). Due to the flux attachment, the effective magnetic field experienced by each CF is reduced to one flux quanta, which corresponds to a effective magnetic

field $\frac{1}{3}$ of the original value. In this case the filling factor for the electron is $\nu = \frac{1}{3}$ or $\nu^* = 1$ for the CF [122]:

$$|\nu| = \frac{|\nu^*|}{m|\nu^*| \pm 1}\,, \tag{1.18}$$

where m here is an even number and ν^* is the integer filling factor for CFs and ν is the filling factor for electrons. The plus (minus) sign in Equation 1.18 shows the integer Hall sequence sitting to the right (left) side of $|\nu| = \frac{1}{2}$. This equation fits the data we observed in Figure 1.7 (b). The CF model is also in good agreement with the numerical studies made by Laughlin [70] and it provides a useful, and unified way, to model different classes of quantum Hall states.

As we will discuss in Chapter 6, as the quality of the halide perovskite 2DESs continues to improve, we can hope to ultimately reveal signatures of the IQHE and FQHE in this new class of quantum electronic materials.

CHAPTER 2

EPITAXIAL SINGLE-CRYSTAL HALIDE PEROVSKITES: A NOVEL PLATFORM FOR QUANTUM PHYSICS

2.1 Introduction

In the past 10 years, hybrid organic-inorganic halide perovskites have attracted immense attention as an exceptional new class of semiconductors for solar harvesting [62], light emission [48], quantum dots [106] and thin film electronics [21]. Although efficiencies of solar cells based on hybrid organic-inorganic perovskites have exceeded 22%, the toxicity of lead devices and lead manufacturing, in addition to the instability of organic components, have been the two key barriers to their wide application [7, 38]. In recent years, tin-based inorganic halide perovskites $CsSnX_3$ (where X=I, Br, Cl) have been considered promising materials to replace the hybrid organic-inorganic halide perovskites, since tin is nearly one thousand times less toxic than lead, plus CsX has similar toxicity to NaCl and KCl. These materials are semiconductors when undoped as shown in Table 2.1 for $CsSnI_3$, [40], $CsSnBr_3$ and [101] $CsSnCl_3$. In fact, $CsSnX_3$ has been used recently for lasers [129] and light-emitting diodes [53], given its high-quality and flexible crystal structure. However, we also note that the photovoltaic and electronic applications of typical solution-grown $CsSnX_3$ have been less encouraging and demonstrated relatively low efficiency [15]. The limited applications of these materials is partially be due to the relatively low material quality caused by the presence of structural defects. Even though progress has been made using inorganic halide perovskites, which are considered as "defect-tolerant" when grown from solution, there is still a need to transition these materials from polycrystalline layers to epitaxial single-crystal layers for improved device quality and performance.

These material improvement also open the door to the possibility to study delicate and emergent quantum many-electron phenomena, such as those described in the previous chapter, in epitaxial halide perovskite devices. In fact, perovskite films have previously been shown to exhibit various

quantum phenomena at low temperatures, such as superconductivity [107] and ferroelectricity [17]. These observations indicate the potential of these materials to host other quantum coherent transport phenomena if the devices are made of sufficiently disorder-free materials. The group lead by our collaborator Professor Richard Lunt, here at MSU in the Department of Chemical Engineering and Materials Science, is actively working on making single-crystalline thin film devices with enhanced performance and quality. In particular one avenue of their research is to reduce the defect levels in halide perovskites to enhance inorganic perovskite properties for electronic applications. Moreover, the heteroepitaxy of these perovskite films allows for devices with precise film thicknesses, controllable structure, phase and orientation, integration into quantum wells, and opens the door to more complicated quantum devices such as nanowires. Professor Lunt's group has demonstrated the ability to precisely grow epitaxial single-crystal halide perovskite thin films using a vapor phase epitaxial growth method [127], which opens the door to new materials for low-dimensional quantum electronic devices. To explore this research direction we have performed low-temperature magnetotransport measurements using devices made from these epitaxial single-crystal halide perovskite thin films. Before discussing the low-temperature quantum coherent transport phenomena we have observed in epitaxial single-crystal halide perovskites thin films in Chapters 4 and 5, this chapter focuses on introducing the essential physical and electrical properties of this class of semiconducting materials.

2.2 Epitaxial Single-Crystal Halide Perovskites Thin Films

High-quality epitaxial thin film growth of halide perovskites, as well as halide perovskite quantum wells has recently been studied in [130, 129, 127, 126]. "Epitaxial" growth of one crystalline material on another is a type of growth in which the crystal being grown mimics the orientation of the substrate, i.e. the two crystals attempt "lattice-matching". More specifically, the vapor phase epitaxy [14] of the $CsSnI_3$ and $CsSnBr_3$ thin film devices studied in this dissertation was achieved on lattice-matched metal halide crystals with a congruent ionic bonding technique. Vapor phase epitaxy is a physical vapor deposition process where multiple source materials are heated in

baffled tungsten boats producing a high vapor pressure stream in a thermal evaporator. Then, the evaporated materials traverse a vacuum chamber and coat a single-crystal halide substrate. This epitaxial growth is monitored *in situ* using a Reflection High-Energy Electron Diffraction (RHEED) system to study the evolution of surface structures and to confirm a desired growth result. The resulting $CsSnI_3$ and $CsSnBr_3$ thin films have similar crystal structures as their substrates [127]. More detailed discussion about the vapor phase epitaxy of our halide perovskites thin film devices can be found in the following dissertation [14].

In this section, several important aspects of the epitaxial single-crystal halide perovskites thin films grown by Professor Lunt's group are discussed. These include the procedures for thin film growth, the crystal structures of the materials, which can be analyzed via x-ray scattering and transmission electron microscopy (TEM). These characterizations demonstrate the high quality of the epitaxial single-crystal thin film device produced, which were then used in studying quantum coherent transport phenomena at low-temperature and high magnetic field.

2.2.1 Crystal Growth and Crystal Structures

In this subsection, we will briefly describe some of the most important steps used by our collaborator in growing epitaxial layers of single-crystal $CsSnI_3$ and $CsSnBr_3$ used in this dissertation, as well as the crystal structures of the thin films.

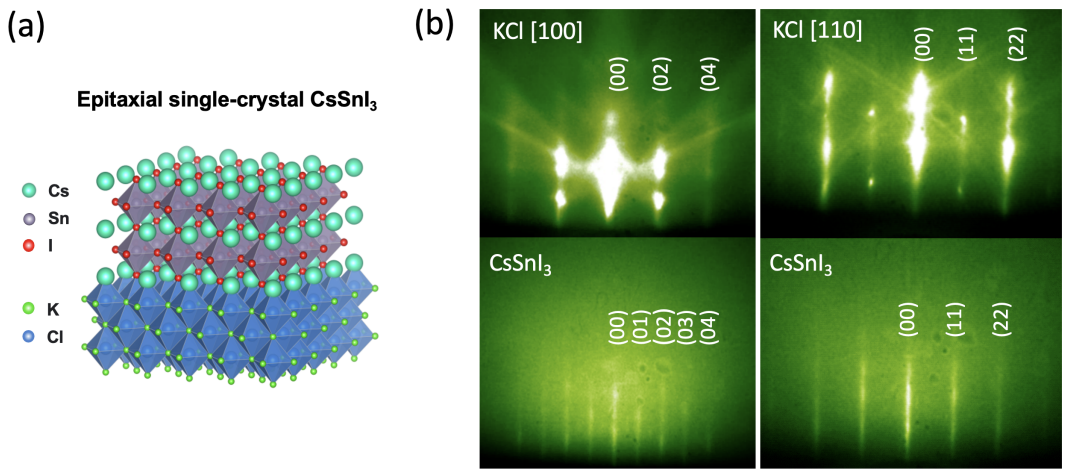

Figure 2.1: (a) Crystal structure of epitaxial $CsSnI_3$ on a single-crystal potassium chloride (KCl) substrate (cyan is Cs, gray is Sn, red is I, green is K, blue is Cl) [39]. (b) RHEED pattern of the KCl substrate (top panels) and $CsSnI_3$ thin film showing well-defined crystalline streaks in both the KCl and epitaxially grown $CsSnI_3$.

Epitaxial single-crystal $CsSnI_3$ thin films: The epitaxial $CsSnI_3$ crystalline film samples were grown in a custom Angstrom Engineering thermal evaporator by co-evaporation from two tungsten boats containing precursor materials (CsI and SnI_2, in a ratio of 1:1), with each source having an independently calibrated quartz-crystal-microbalance rate monitor and source shutter. A 50 nm thick $CsSnI_3$ film was deposited stoichiometrically at a rate of 0.007 nm/s on a cleaved [100] surface of a potassium chloride (KCl) single-crystal substrate. The growth was performed at pressures less than some 3×10^{-6} Torr and a temperature of 22°C. Crystal analysis was performed using *in situ* real-time RHEED [49] to determine structure and film quality (see Figure 2.1). The RHEED scans were performed at 30.0 kV and an emission current of less than 50 nA to reduce damage and charging on the perovskite film during growth. With these measurement conditions, no damage was observed over typical deposition times of up to 1-2 hr. Gold contacts (50 nm thick) for the electrical transport measurements were deposited on the perovskite layers using electron-beam evaporation at a rate of 0.02 nm/s through a mechanical shadow mask located in the same deposition chamber, with the same temperature and base pressure.

The resulting $CsSnI_3$ epitaxial film is pseudomorphic to the KCl substrate as shown in Figure 2.1

Table 2.1: Crystallographic data of various phases of $CsSnI_3$. Modified from [126] and [39]. Simulated bandgaps were calculated in Materials Studio 7.0 using the CASTEP module with the B3LYP functional. At room temperature, only the orthorhombic and epi-tetragonal phases have been observed for $CsSnI_3$, along with a large bandgap orthorhombic phase (not included).

Phase	Cubic (High *T*)	Tetragonal (High *T*)	Orthorhombic (Room *T*)	Epi-tetragonal (Room *T*, this work)
Crystal Structure Cs Sn I	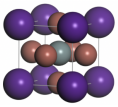	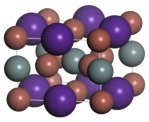	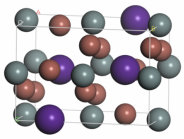	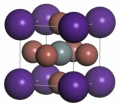
Lattice Parameters (nm)	*a*=0.6206	*a*=*b*=0.8718, *c*=0.6191	*a*=0.8689, *b*=1.2378, *c*=0.8638	*a*=*b*=0.622±0.007, *c*=0.612±0.002
Experimental Bandgap (eV)	-	-	1.31	1.85
Simulated Bandgap (eV)	0.76	0.41	1.40	2.07

(a). This is confirmed by rotation-dependent RHEED patterns (Figure 2.1 (b)), since the crystalline streaks in $CsSnI_3$ greatly resembles those of single-crystal KCl. Moreover, the streaky patterns observed are indicative of smooth growth compared with spotty patterns seen in rougher films (which will be discussed further in Subsection 2.2.3). The crystal structure of our epitaxial $CsSnI_3$ thin film at room temperature is similar to the high temperature cubic phase but tetragonally distorted to epitaxial tetragonal (epi-tetragronal) phase due to the in-plane tensile strain produced by the lattice mismatch. The lattice mismatch between the epi-tetragronal phase of our $CsSnI_3$ and face-centered-cubic (FCC) of KCl substrate is 2% [126]. The RHEED data (Figure 2.1 (b)) also show a clear change in the symmetry from FCC substrate to a primitive perovskite cell by the emergence of (01) streaks between the (02) streaks of the substrate. More information about the epi-tetragonal phase (and other phases) of $CsSnI_3$ used in this work is shown in Table 2.1. Epi-tetragronal $CsSnI_3$ is a direct band gap semiconductor when it is undoped, with an experimentally determined bandgap of 1.85 eV, and its calculated band structure is shown in Figure 2.2.

Epitaxial single-crystal $CsSnBr_3$ thin films: For epitaxial single-crystal $CsSnBr_3$ thin film

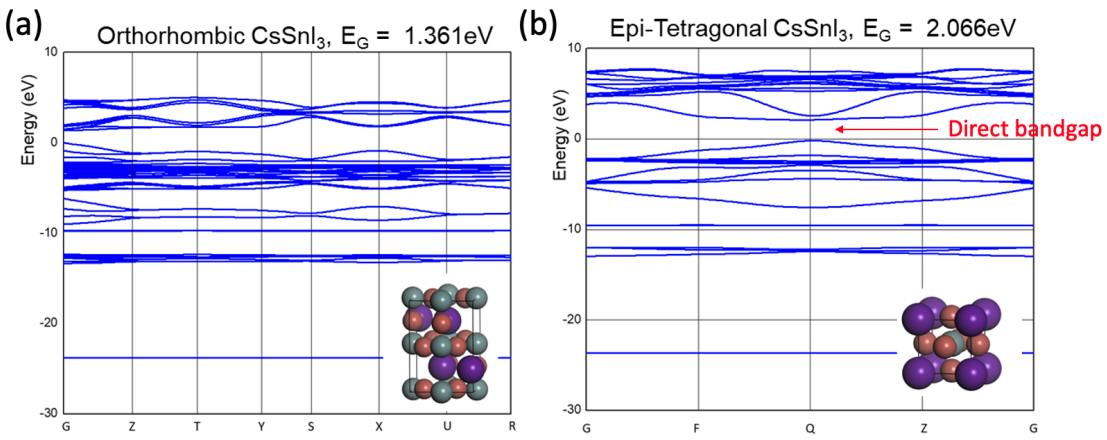

Figure 2.2: Calculated electronic band structures of $CsSnI_3$. Calculated band structures for the (a) orthorhombic and (b) epi-tetragonal phases of $CsSnI_3$. The data were calculated in Materials Studio 7.0 using the B3LYP DFT functional in the CASTEP module.

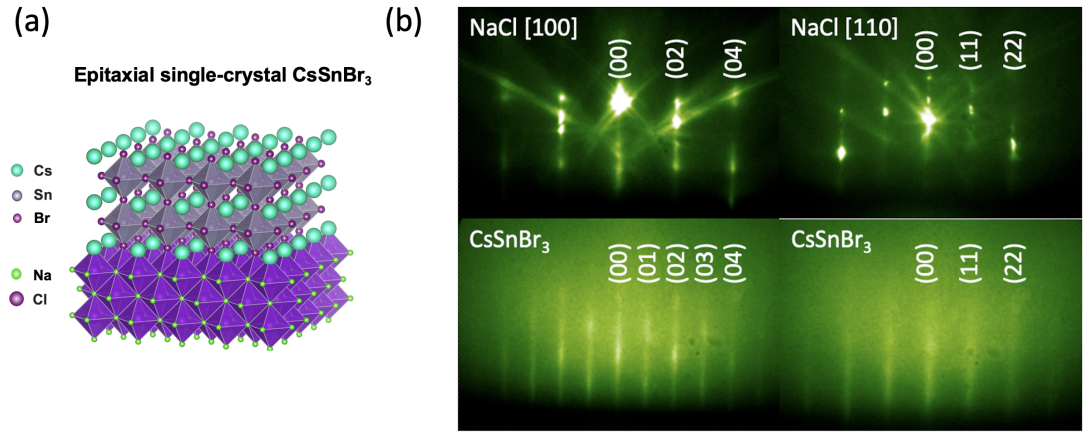

Figure 2.3: (a) Crystal structure of $CsSnBr_3$ on NaCl (cyan is Cs, gray is Sn, dark purple is Br, green is Na, purple is Cl). (b) RHEED pattern of the NaCl substrate (top panels) and $CsSnBr_3$ thin film showing crystalline streaks in both the NaCl and epitaxially grown $CsSnBr_3$ that vary as expected with rotation.

samples, a 20 nm thick epitaxial film of $CsSnBr_3$ was deposited stoichiometrically on a cleaved [100] surface of a sodium chloride (NaCl) single-crystal substrate. The growth of the epitaxial layer was performed at pressures less than 3×10^{-6} Torr and a temperature of 22°C. The schematic structure of the epilayer and *in situ* real-time RHEED of the grown epilayer are shown in Figure 2.3

(b), and the crystal structure of the thin film is shown in Figure 2.3 (a). The $CsSnBr_3$ epitaxial film is also pseudomorphic to the substrate (NaCl) as we have seen from $CsSnI_3$ (KCl). The additional (01) streaks (see Figure 2.3 (b)) emerge for $CsSnBr_3$ due to the primitive cell versus the face-centered cubic cell of the substrate. The lattice mismatch between the cubic phase of our $CsSnBr_3$ to NaCl substrate is 2.8% [127]. In addition, the undoped cubic phase of $CsSnBr_3$ at room-temperature is a also a direct band gap semiconductor with a experimentally determined band gap of 1.75 eV [40].

2.2.2 Transmission Electron Microscopes Images and X-ray Characterization

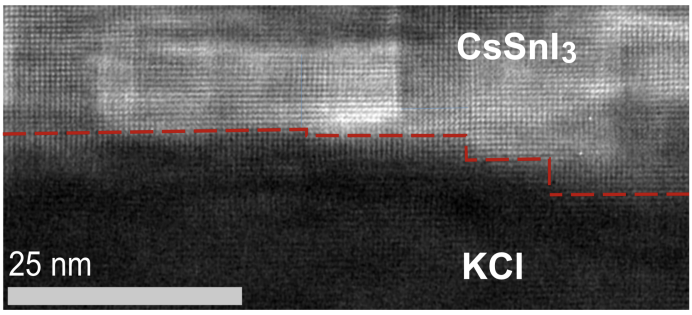

Figure 2.4: TEM image of $CsSnI_3$ epilayer on KCl. The dashed red line indicates the interface between the $CsSnI_3$ epilayer and the KCl substrate. Note that the areas of differing brightness likely arise from local variations in the thickness of the TEM slice.

To provide further evidence that the films made by the methods discussed in the previous subsection are both epitaxial and pseudomorphic, several additional characterizations of the $CsSnI_3$ devices have been made. Figure 2.4 is the widest view Transmission Electron Microscopes (TEM) image of the $CsSnI_3$ and KCl interface. This figure shows highly crystalline $CsSnI_3$ adlayer growth upon a terraced substrate surface without clear grain boundaries. The presence of the slight lattice mismatch at the step edges is due to the 2% tetragonal distortion of the lattice constant (c-parameter). This distortion creates a local strain around the step edge that has been shown to induce a slight tilt of the film across the substrate, which is common and has been observed in other epitaxial systems [93]. Thus, these steps in the interface are not sources of grains but rather

an inhomogeneous strain localized around the step edges. This is consistent with our observation of slight anisotropic alpha-angle shifts in x-ray pole figure scans, which will be discussed below (see Figure 2.5).

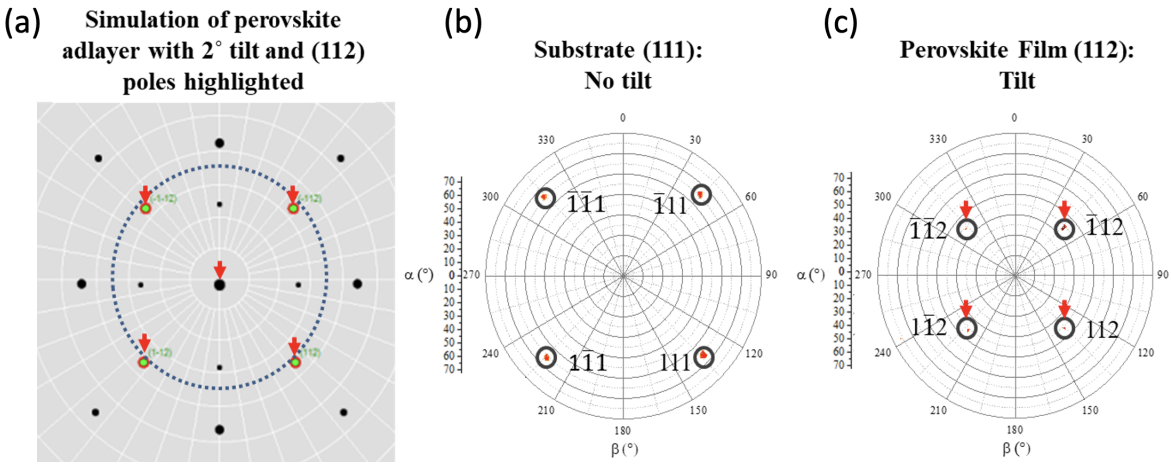

Figure 2.5: Pole figure data and epitaxial tilt. A simulated pole figure (a) of the $CsSnI_3$ adlayer compared to experimental pole figure scans of the substrate (b) and perovskite (c). The red arrows indicate the direction of the pole shift (lengths exaggerated).

Before describing Figure 2.5, we will give a brief introduction to the pole figure measurement. Unlike x-ray diffraction (XRD), which determines atomic and molecular structure of a crystal, pole figure measurement is used to study the orientation distribution of crystallographic lattice planes and textures. Each pole figure corresponds to a unique orientation of a sample plane. The way to collect a pole figure is to perform a stereographic projection, in which the the crystal structure of the sample needs to be well known so that the diffraction angle of the x-ray corresponding to the lattice plane can be set for the scan. The diffracted intensity is collected by varying two geometrical parameters: the tilt angle from the sample surface normal direction (α) and the rotation angle around the sample surface normal direction (β). The collected data is plotted as a function of α and β [14]. For our $CsSnI_3$ sample the pole figure scans in Figure 2.5 contain poles that are shifted away from their ordinarily radially-symmetric positions, as seen in both the simulated and experimental pole figures. This tilt is not observed in the pole figure of the underlying KCl substrate, indicating

that the tilt is indeed caused by an angled surface of the film and not from a tilted substrate.

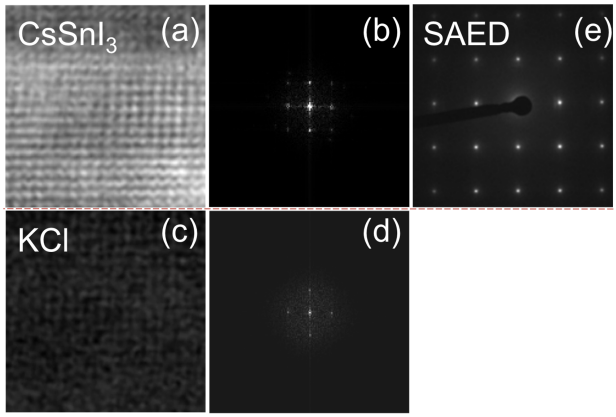

Figure 2.6: TEM images and associated FFT analysis for the $CsSnI_3$ adlayer ((a) and (b)). TEM images and associated FFT analysis of the KCl substrate ((c) and (d)). Selected Area Electron Diffraction (SAED) for the $CsSnI_3$ epilayer (e).

Figure 2.6 illustrates the TEM analysis and Selected Area Electron Diffraction (SAED) of a $CsSnI_3$ epilayer. We note that tetragonal distortion of the $CsSnI_3$ layer should be observed in the Fast Fourier Transform (FFT) images but is difficult to see from the pattern due to the relatively small amount of tetragonal distortion. In fact, the tetragonal distortion can be more clearly extracted from the TEM image by counting rows of atoms horizontally versus vertically. Layer shown in panel (e) clearly show the tetragonal distortion that leads to the tensile reduction in the crystal c-direction.

2.2.3 Growth Ratio and Rate

This subsection describes how the precursor growth ratio and growth rate can influence the resulting epitaxial thin films, and to provide more evidence supporting the high-quality of our epitaxial thin films. We will start by discussing the impact of different growth precursor ratios. As described in section 2.2.1, the Cs:Sn ratio used for growing epitaxial single-crystal $CsSnI_3$ thin film on KCl is nominally 1:1. The successful epitaxial growth with this ratio has been confirmed by the RHEED pattern in Figure 2.1 (b). If growth is performed with a different ratio of Cs:Sn, we do not get

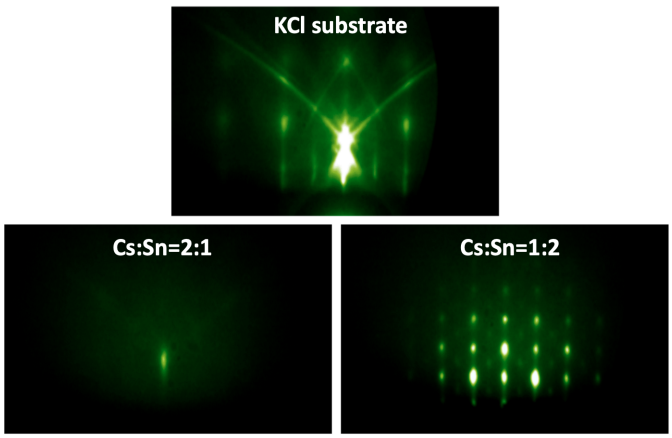

Figure 2.7: RHEED scans of $CsSnI_3$ on KCl with varying precursor ratios of $CsI:SnI_2$ showing changes in crystal structure and quality as growth leaves the stoichiometric ratio of 1:1. The scans show the KCl substrate (top) and the epitaxial film at several hundred angstroms (bottom).

the desired result, which is confirmed in Figure 2.7. A 2:1 growth ratio results in an essentially amorphous film, and can be seen in the complete lack of clear streaks or spots in the RHEED pattern due to the presence of a large number of Sn vacancies in the resulting material. A 1:2 growth favors the incorporation of Cs vacancies and results in a rough crystalline film that is likely $CsSn_2I_5$, analogous to a similar bromide compound ($CsSn_2Br_5$) seen in Ref. [127].

In addition, the growth rate of the thin film is another important factor for producing epitaxial thin films. Figure 2.8 shows the RHEED scan of a $CsSnI_3$ thin film whose growth is performed at a higher growth rate (0.1 nm/sec) compare with the film (0.007 nm/sec) shown in Figure 2.1. The bottom images are different rotations of the final film, showing spotty (rough) patterns. The low growth quality at high rates likely stems from imbalance of the lower reaction rate with high deposition rate that leads to an accumulation of vacancies and non-uniform (island) growth. The presence of half order spots indicates a larger unit cell that may result from the presence of Cs vacancies similar to the 1:2 growth shown in Figure 2.7.

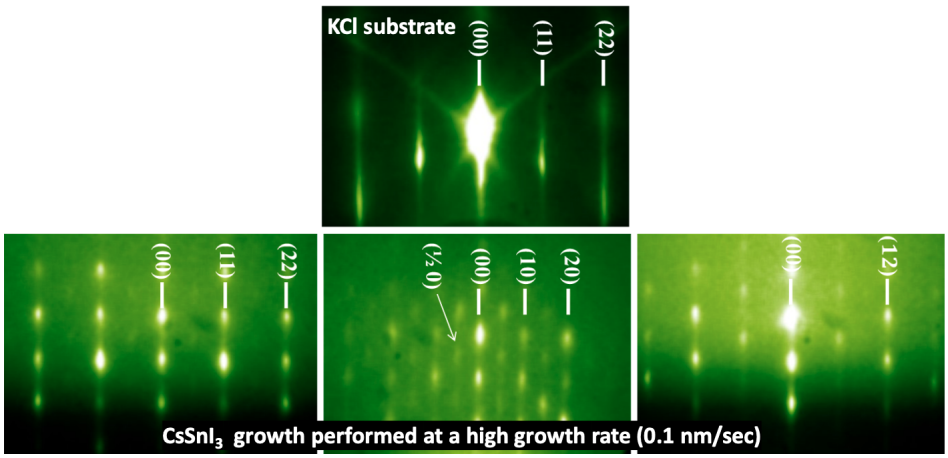

Figure 2.8: RHEED scans of KCl (top image) with the $CsSnI_3$ growth (bottom images) performed at a high growth rate (0.1 nm/sec). The bottom images are different rotations of the final film, showing spotty (rough) patterns. The low growth quality at high rates likely stems from imbalance of the lower reaction rate with high deposition rate that leads to an accumulation of vacancies and non-uniform (island) growth. The presence of half order spots indicates a larger unit cell that may result from the presence of Cs vacancies similar to the 1:2 growth shown in Figure 2.7.

2.3 Air-Stability of Halide Perovskites

This section discusses the stability of the halide perovskites in air. It is well known that upon exposure to air $CsSnI_3$ transforms into Cs_2SnI_6, and this transformation would prevent us from studying the low-temperature quantum coherent transport of $CsSnI_3$ unless careful precautions are taken (see Section 3.5). Therefore, knowing how quickly the material degrades after exposure to air is important for developing protocols for device handling, transferring and wiring up. Below we describe several methods we have used to characterize the air sensitivity of our devices.

First, we characterized the air sensitivity of our epitaxial devices $CsSnI_3$ using XRD (see Figure 2.10 (a)) to monitor the changes in crystal structure. The first observation of change in the XRD peaks (indicating the transition of $CsSnI_3$ to Cs_2SnI_6) begins to occur after approximately 3 hours in air. Additionally, simply monitoring the $CsSnI_3$ device color as we expose it to the air is an effective characterization of the device degradation. As shown in Figure 2.10 (b), there is a clear color change (from brown $CsSnI_3$ to transparent Cs_2SnI_6) of the sample after several hours

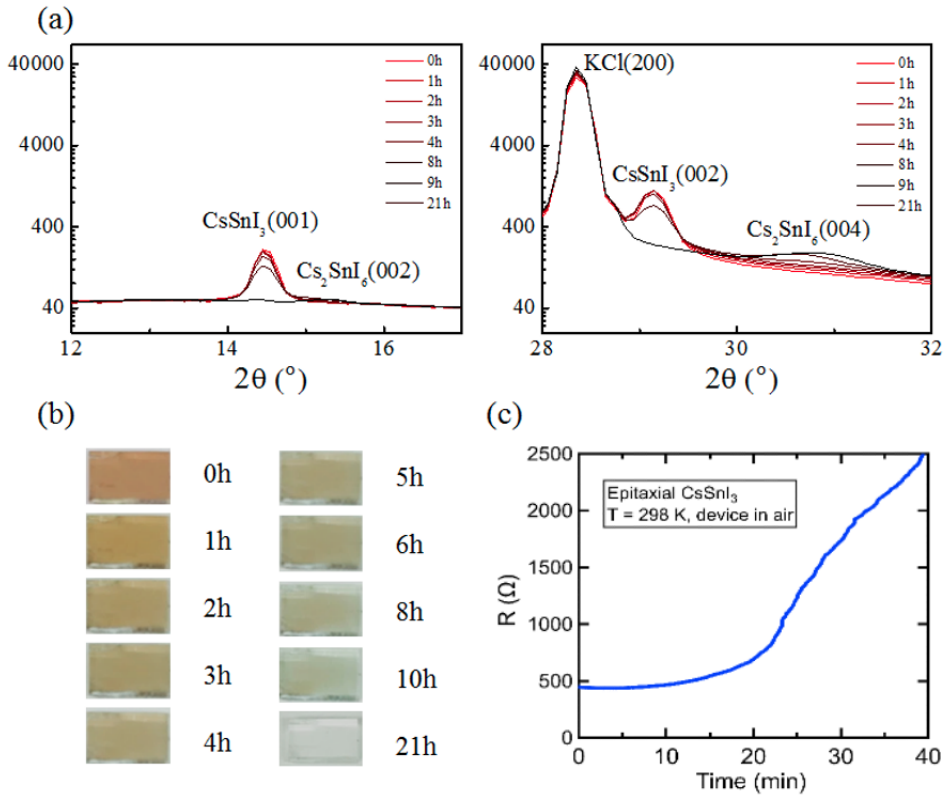

Figure 2.9: (a) XRD scans of a 50 nm epitaxial $CsSnI_3$ film degrading over time while exposed to air. At 3 hours, the perovskite peaks begin to disappear and the degradation product, Cs_2SnI_6, appears. (b) Optical images of the degrading perovskite sample, showing the transformation from the brown $CsSnI_3$ to the transparent Cs_2SnI_6. (c) Resistance R versus time of an epitaxial $CsSnI_3$ film device exposed to the air. Changes in the resistance begin to occur after $\sim$ 20 min, likely due to the degradation at the interface first and a greater sensitivity in the resistance measurement overall. After several hours the resistance of the device becomes > 50 MΩ.

of exposure to air.

Furthermore, the results of room-temperature resistance measurements (see Figure 2.10 (c)) of the $CsSnI_3$ epitaxial layers are a precise measure of material degradation in air. During the first 15-20 minutes, the device resistance does not change significantly. With continued exposure we clearly observe an increase in the device resistance as time increases, which continues until it is > 50 MΩ. We attribute this behavior to the known transformation of $CsSnI_3$ into Cs_2SnI_6 upon exposure to the air [79]. These results demonstrate that the device resistance serves as non-invasive probe for monitoring the stability of the epitaxial layer and for confirming that it has not transformed

to Cs_2SnI_6.

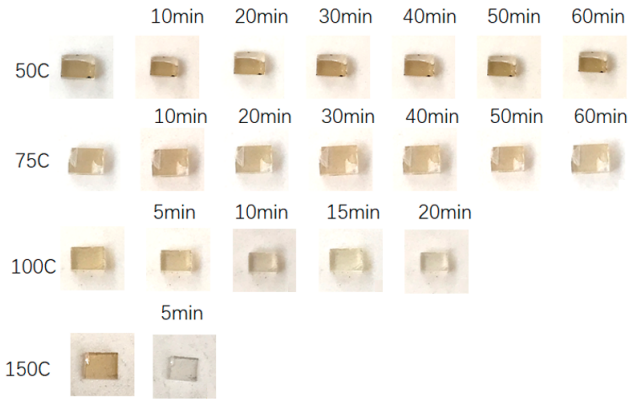

Figure 2.10: Upon exposure to air, $CsSnBr_3$ undergoes a chemical transformation leading to marked change in color (brown to transparent). The rate of this air-driven material change with increased temperature as shown in the figure.

Similar to $CsSnI_3$, transformation from $CsSnBr_3$ to Cs_2SnBr_6 caused by exposure to air can also been observed using similar methods as described above. In Figure 2.10, we present data showing the color change of several $CsSnBr_3$ films in air with various amount of heating, which also shows that heating speeds up the process of film degradation, as one might expect.

CHAPTER 3

MEASUREMENT SETUP AND PROCEDURES

This chapter details the experimental setups and equipment used for the low-temperature magnetotransport measurements in this dissertation. Important measurement techniques and procedures are also discussed.

3.1 Dilution Refrigerator

A dilution refrigerator (DR) is essential to a modern low-temperature physics lab, as it brings the target system to low temperature where quantum phenomena can be observed. Thus, in this section we will discuss the basic principle of the dilution refrigeration process, and introduce the DR system used for the low-temperature transport measurements.

3.1.1 General Introduction

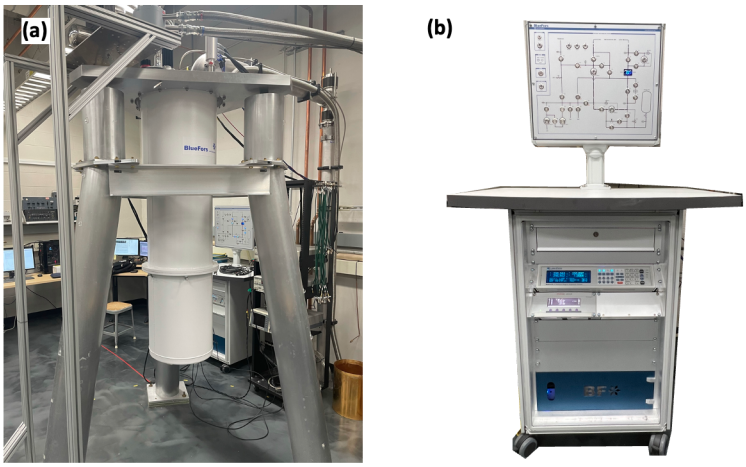

Figure 3.1: Photos of the Bluefors LD400 cryogen-free dilution refrigerator (DR) system. (a) The cryostat and its supporting frame. (b) The control unit.

All the cryogenic temperature measurements in this dissertation were performed using a BlueFors LD400 cryogen-free DR system. The four basic components of this system are described

below:

The cryostat: The cryostat (supported by a tripod, see Figure 3.1(a)) contains helium pumping (returning) lines, heat exchangers, thermometers, electrical wiring and flanges at different temperature stages, etc. Devices are mounted and tested at the coldest stage of the cryostat called the mixing chamber, which can achieve $T \simeq 10$ mK.

The control unit: The control unit (Figure 3.1(b)) contains all the electronics to control the DR system. Different from a traditional DR with manual valves located in a gas handling system (GHS), in our Bluefors LD400 DR, pneumatic valves in the GHS can be controlled remotely through the control unit. The status of the GHS and cryostat are also displayed in the control unit, which can itself be operated remotely via a computer interface.

The gas handling system (GHS): The GHS (Figure 3.2 (a)) is contained in a single cabinet. It contains turbo pumps, scroll pumps, pumping lines, valves, pressure gauges and mixture tanks, etc, which are necessary to the operation of the DR system.

The pulse tube compressor: The pulse tube and compressor (Cryomech CP1000 series PT415) are essential for pre-cooling the DR to a temperature at which liquid helium liquefies, so that no external supply of cryogenic liquids is needed. Because of the vibrations they produced, the GHS and pulse tube compressor are placed in a separate room away from the cryostat and control unit.

3.1.2 Dilution Refrigerator Operation Principles

Next, we will describe the fundamental principles of the DR's cooling cycle, which is the only system that can provide continuous cooling power at $T < 300$ mK. The DR in our lab can achieve a lowest temperature ~7 mK at the mixing chamber stage. The cooling power of the DR is provided by the dilution of a mixture of Helium-3 (^{3}He) and Helium-4 (^{4}He) isotopes [104].

To run the dilution refrigerator cooling cycle, we first pre-cool the system to a temperature at which liquid helium liquefies (below 4.2 K) using the pulse tube. At this temperature, the mixture of ^{3}He and ^{4}He is introduced into the DR to cool down the system even further. The general idea of this process is the following: at saturated vapor pressure, pure ^{4}He undergoes a phase transition at

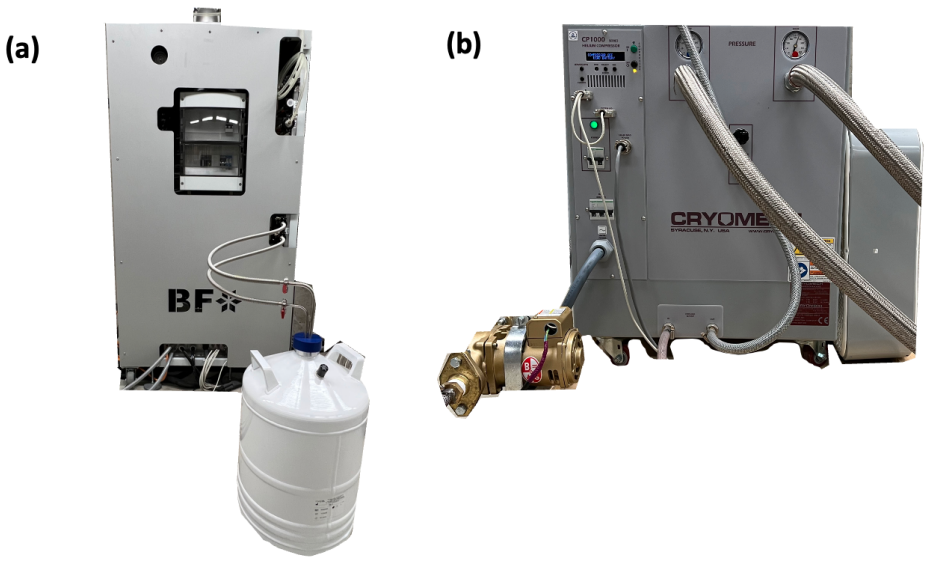

Figure 3.2: (a) Gas handling system (GHS) of the Bluefors LD400 cryogen-free DR with cold trap attached. (b) Cryomech CP1000 series PT415 pulse tube compressor with a fan and water booster pump, which help cool the compressor during the operation.

2.17 K from a normal fluid into a superfluid. If we dilute the ^{4}He with ^{3}He, the superfluid transition temperature of the ^{4}He in this mixture will also decrease (see Figure 3.3). When the temperature is below 0.8 K, the mixture of ^{3}He and ^{4}He undergoes spontaneous phase separation into a ^{3}He rich phase (concentrated phase) and ^{3}He poor phase (dilute phase). At very low temperatures, the concentrated phase is almost pure ^{3}He, while the dilute phase contains about 6.6% ^{3}He, and they are separated by a phase boundary [104]. The enthalpy of ^{3}He in the dilute phase is larger than that in the concentrated phase. As a consequence, energy (heat) is required if ^{3}He is taken from the concentrated to the dilute phase. The place where the heat exchange between these two phases happens is called mixing chamber (MXC), it is the coldest stage of the DR system.

To show how to realize the refrigeration process, we present a schematic diagram of our cryogen-free DR (Figure 3.4 (a)), along with a photo showing what is inside the cryostat (Figure 3.4 (b)). After pre-cooling, the system is below 4.2 K. The mixture of ^{3}He and ^{4}He is condensed into the system via the ^{3}He condensing line, and we fill the entire MXC with the mixture. After that, the DR cooling cycle is started by pumping the mixture from the MXC via the still pumping line (the

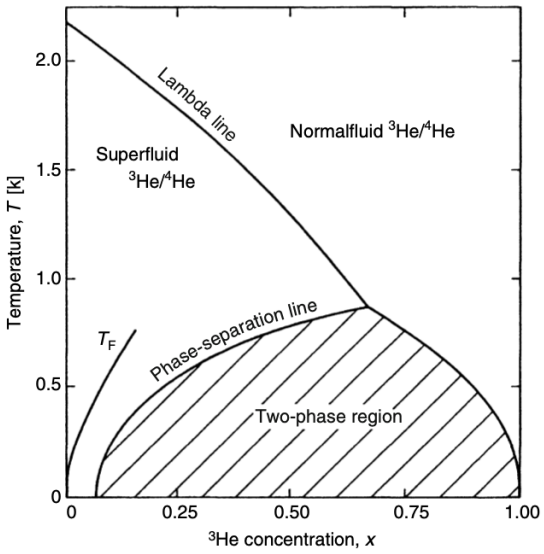

Figure 3.3: Phase diagram of liquid ^{3}He/^{4}He mixtures [104].

mixture pumped out will return to the MXC through condensing line), and the system will be cooled down below 0.8 K by evaporative cooling. Once the phase separation starts to show up in the MXC, the dilute phase of the mixture sinks below the concentrated phase because it is more dense.

When the MXC temperature goes below 0.8 K, the helium pumped from the dilute phase is almost pure ^{3}He. This is because the vapor pressure of ^{3}He is at least two orders of magnitude higher than vapor pressure of ^{4}He [104]. As the DR runs continuously, the ^{3}He pumped from the MXC will be re-condensed (with the help of, (i) heat exchangers connected to the still and condensing line, and (ii) heat exchange between condensing line and refrigeration part of the DR driven pulse-tube) and return to MXC. This closed loop of ^{3}He circulation brings the MXC to its lowest temperature (~10 mK). The cooling power of the system therefore strongly depends on the ^{3}He circulation rate across the phase boundary in the MXC. The circulation rate can be increased by applying heat to the still, increasing the ^{3}He vapor pressure, resulting in a higher throughput of ^{3}He through the circulation pumping system.

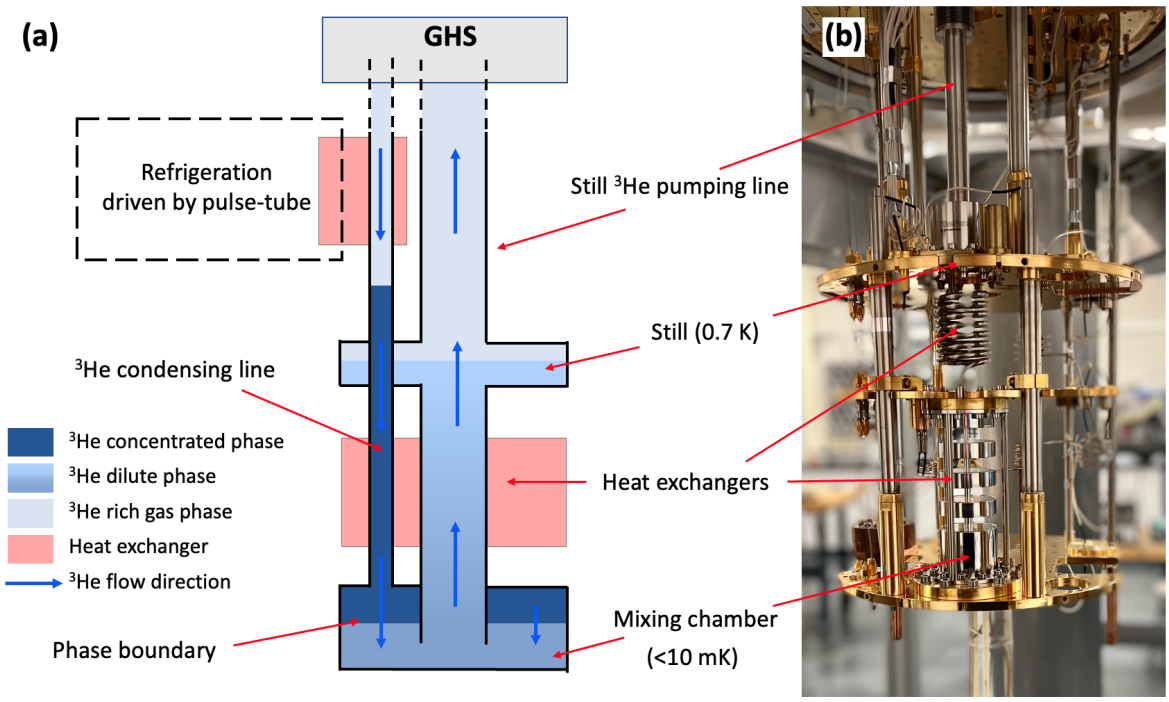

Figure 3.4: (a) Schematic diagram of a cryogen-free ("dry") DR. (b) Photo shows the inside of the Bluefors LD400 DR cryostat. Note that the still pumping line and ^{3}He condensing line contain heat exchangers to help thermal contact.

3.2 Superconducting Magnet

To reveal the collective behavior and quantum coherent transport of charge carriers at low temperatures in a 2DES, it is necessary to apply a strong magnetic field to the system. In this section we describe the magnet used in our experiment to apply the necessary field.

Our magnet system is an integrated cryogen-free superconducting magnet system (see Figure 3.5) manufactured by American Magnetics Inc. Compared with traditional liquid helium cooled magnet systems (i.e. "wet" magnets), the cryogen-free magnet ("dry" magnet) does not involve external cryogenic liquid for cooling. The magnet (see Figure 3.5 (a)) consists of compensated solenoids, and it is manufactured in a configuration to accommodate the requirements of our measurements and the size of Bluefors LD400 DR. The cryogen-free magnet in this system connects to the 4K stage of the DR. Once the cool-down cycle of the DR is complete, the solenoid made of Nb_3Sn wire is below its superconducting transition temperature (18.3 K), and will carry

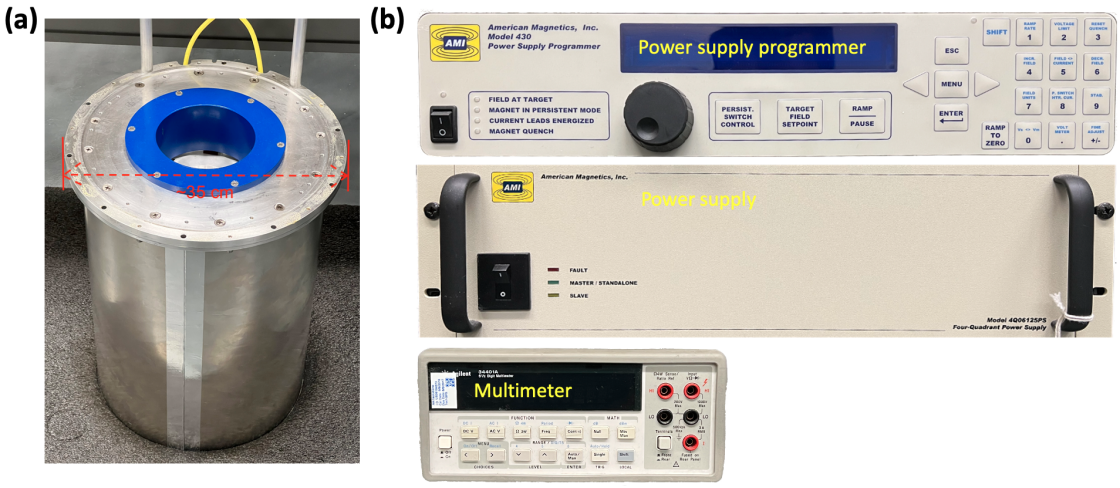

Figure 3.5: Photos of the AMI 14T integrated cryogen-free superconducting magnet system. (a) cryogen-free superconducting magnet. (b) From top to bottom are the power supply programmer, power supply and Agilent HP 34401A multimeter. The multimeter is used to measure the voltage drop across a resistor ($R = \frac{50\,\text{mV}}{150\,\text{A}} = 0.33\ \text{m}\Omega$) in series with the magnet winding to calculate the current flow through the magnet solenoid. The field-to-current factor of this magnet is 0.1313 T/A.

current without resistance.

The superconducting magnet can also be operated in persistent mode, without connection to the external power supply providing the current to the solenoids. This is achieved via a short section of superconducting wire connected in parallel to the solenoid, i.e. the so-called "persistence switch". When the switch is heated via a connected heater it will become a resistive normal conductor. When the appropriate operating current in the magnet is achieved, the heater can be turned off and the persistent switch is allowed to cool until it becomes superconducting. At this point, the power source to the magnet is no longer needed and a constant magnetic field is created via current flowing through the magnet windings and the persistence switch.

The magnet can create up to 14 T magnetic field in a bore with a diameter of ~2 inches with field-to-current factor is 0.1313 T/A. Appendix D provide additional details about how to properly operate the magnet and avoid a quench.

3.3 Cold-Finger and Sample Stages

Before mounting a device to the DR and performing low-temperature magnetotransport measurements, we must consider two important points. First, we need to thermally connect our device to the MXC, so that the device can be cooled down to mK temperatures. Second, we must make sure that the device is in a specific location along the central axis of the solenoid, thus ensuring that the magnitude of the magnetic field applied to the device corresponds to the correct value. To address these two points, a "cold-finger" is specifically designed (see Figure 3.6 (a)) [67]. The silver rods in this cold-finger are used to transfer heat from the sample to the MXC, and they are annealed to reduce crystal defects. Six alumina rods mechanically support the cold-finger and reduce eddy currents induced as we change the magnetic field. The brass connections at the bottom of the alumina rods are spring loaded to provide stability and account for thermal contractions. Additionally, the length of the rods and the height of the sample stages (shown in Figure 3.6 (c) and (d)) are carefully designed so that the device to be measured sits exactly 41.5 cm below the MXC, where the magnetic field of the solenoid is calibrated.

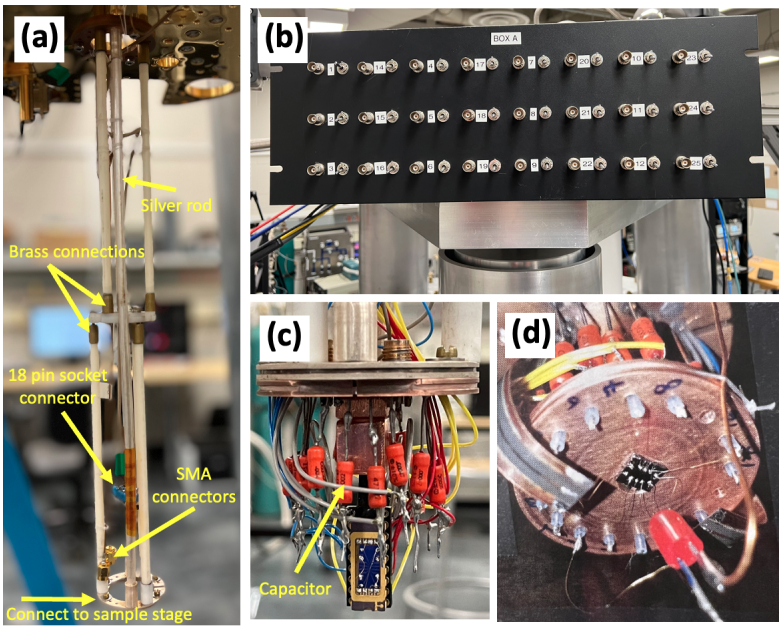

Figure 3.6: (a) Photo of the thermal cold-finger. Notice that the 16-pin socket connector is not connected to the cold-finger and each of the 16 pins is connected in series with a 10 kΩ resistor. Two SMA connectors are connected with coaxial cable, and they run all the way to the top of the cryostat. They enable the ability to apply radio-frequency (RF) signals to the sample. (b) Photo of the breakout box, which is connected to the 16 pin socket connector in (a). (c) Customized sample stage for measuring the critical temperature of a thin superconducting Nb wire. The mylar capacitors are indicated. (d) Another customized sample stage for the GaAs/AlGaAs heterostructures transport measurement discussed in this dissertation.

Customized sample stages can be made for different measurements and mounted to the lower end of the cold-finger. The sample stage shown in Figure 3.6 (c) was used to measure the critical temperature of thin superconducting Nb wires where the plane of the Nb wire device was aligned parallel to the magnetic field. This sample stage can be also modified, as shown in Figure 3.6 (d), to perform quantum Hall measurements on GaAs/AlGaAs heterostructures, in which the 2DES sample is placed perpendicular to the applied magnetic field. The body of the sample stage is made of Oxygen Free High Conductivity (OFHC) copper. There are 16 leads to the sample stage, each of these 16 leads is physically connected to thermal ground with an in-line thin film mylar capacitor (see Figure 3.6 (c)). This 470 pF mylar capacitor, along with a 10 kΩ resistor in series with each measurement line, functions as a low-pass filter that attenuates high frequency (200 kHz) noise.

The device to be measured can be electrically connected to the 16 leads on the sample stage that are connected to a breakout box at the top of the cryostat (see Figure 3.6 (b)). This breakout box has switches to control the open/ground configuration of individual measurement leads in the cryostat. Moreover, we connect measurement instruments to the samples through the breakout box.

3.4 Low-Frequency Lock-In Measurement

This section describes how the low-frequency lock-in transport measurements presented in this dissertation are performed at low temperatures. The typical lock-in used is the Stanford Research Systems lock-in amplifier SR830. An internal oscillator in the lock-in generates a sinusoidal voltage at a certain frequency f. Due to the orthogonality of sine and cosine functions, a multiplier inside the lock-in will only detect the signal at this frequency f without measuring contributions from other signals with different frequencies. This means if a measurement is performed in an extremely noisy environment, a small signal can be amplified and detected.

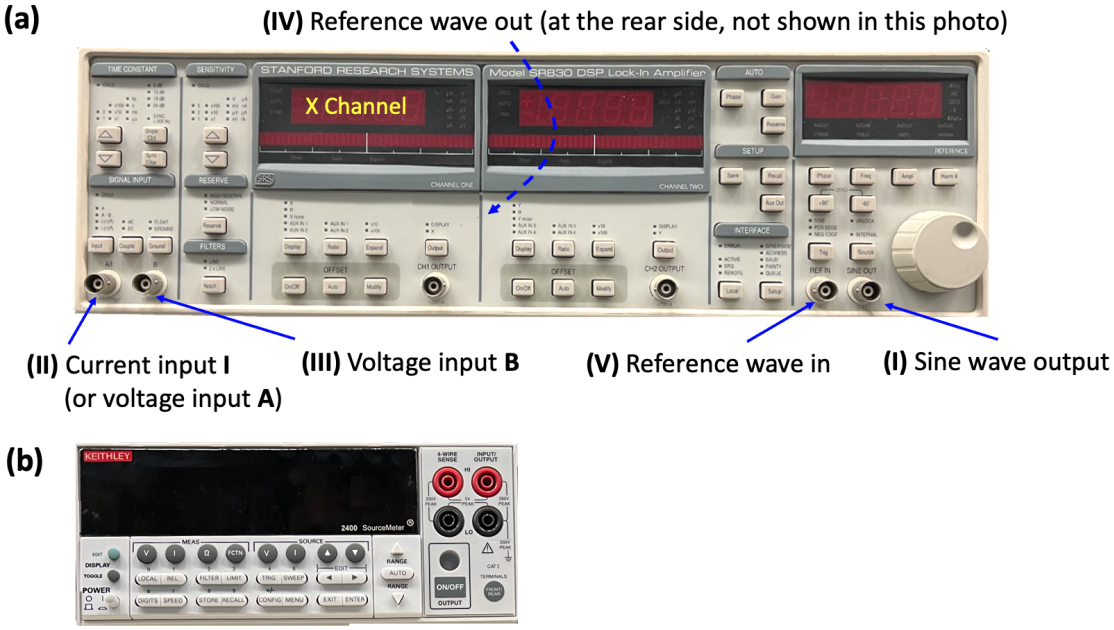

Figure 3.7: (a) Stanford Research Systems lock-in amplifier SR830. The five most important ports and readout X Channel are marked by the blue arrows. (b) Keithley Series 2400 source meter. This source meter functions as a highly accurate voltage source to control the density of charge carriers in 2DES. It can also function as a voltage (or current) meter.

Here we will briefly describe the most commonly used features/ports of the SR830 (see Figure 3.7 (a)). Each of these ports serves a unique function in the process of low-temperature transport measurement. **(I) Sine wave output**. This port can source a variable amplitude voltage at a fixed frequency and phase. **(II) Current input I (or voltage input A)**. This port is used to measure a current from the sample. It can also be used to measure a voltage relative to ground. **(III) Voltage input B**. This port can be used with voltage input A to measure differential (A-B) voltage drop. **(IV) & (V) Reference wave out and reference wave in**. Both of these ports are important for measurement that involves multiple lock-ins. The reference wave out port can source a reference signal, which has the same waveform as the signal coming from the sine wave output. The reference wave in port can receive a reference signal from another lock-in, so that two lock-ins are synchronized. A more complete description of the operation of a lock-in amplifier can be found in the thesis of Dr. Heejun Byeon in Ref. [12].

3.4.1 Four-Terminal Lock-In Measurement on Hall Bar

Subsection 1.3.2 describes the Hall bar device geometry for a 2DES (see Figure 1.2). In this device geometry, if a current is sourced along the sample, the measured longitudinal voltage V_{xx} and transverse (Hall) voltage V_{xy} can be used to obtain the resistivity and conductivity of the device. In this subsection, we discuss how to perform four-terminal transport measurements on a Hall bar 2DES device, such as the bi-layer graphene (BLG) device discussed in Subsection 1.4.4 and Appendix A, as well as methylammonium lead iodide ($MAPbI_3$) device discussed in Chapter 6.

In Figure 3.8, lock-in A sources a voltage V at frequency f and measures the current I at frequency f flowing from contact 1 to 2 through the sample. Lock-in B is used to measure the voltage drop V_{xx} across contacts 4 and 6 of the sample. Additionally, in this setup we can also perform a Hall measurement of V_{xy} across the 2DES using lock-in C, which corresponds to the voltage drop across contacts 5 and 6. To perform this measurement, all three lock-ins are referenced to the same measurement frequency f. Both measurements of V_{xx} and V_{xy} are four-terminal measurements since they separate pairs of current-carrying and voltage-sensing wires.

In some transport measurements on a 2DES, one or several Keithley 2400 source meters (shown in Figure 3.7 (b) and Figure 3.8) are used to supply gate voltages to the sample. This allows for controlling of the charge carrier density in the sample (see Appendix A for more details).

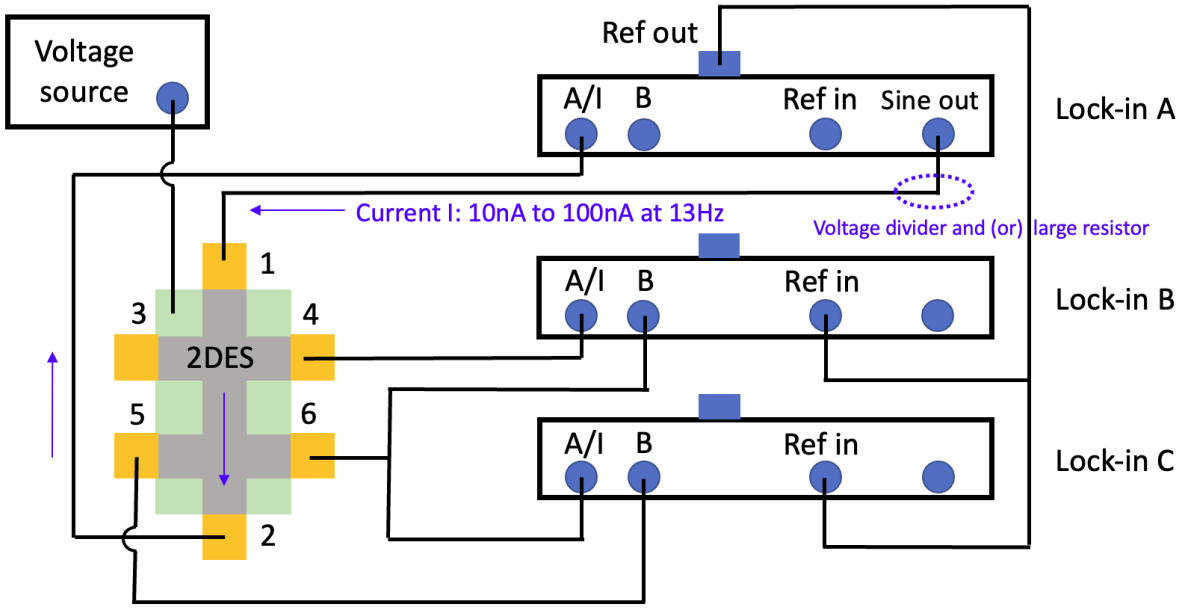

Figure 3.8: Illustration of a four-terminal transport measurement on a 2DES having a Hall bar device geometry. Lock-in A is used to source a voltage and measure the current I (typically between 10 nA to 100 nA at ~13 Hz) through the 2DES. Lock-in B and C measure V_{xx} and V_{xy}. A voltage divider and (or) a large resistor can be attached inline with the output port of lock-in A (illustrated by the dashed circle) to control the current flow through the 2DES. The green shaded area represents the gate electrode of the device, which can be connected to a voltage source, and used to tune the electron density.

The most important benefit of four-terminal measurements is that it allows for the measurement of the electrical resistance of the device separate from that of the Ohmic contacts. This is an extremely valuable feature, given that the contact resistances to a 2DES can dominate the resistance of the 2DES itself. Additionally, the four-terminal measurement eliminates the lead resistances from the measurement. Four-terminal measurements on a Hall bar geometry device can also be used to determine the charge mobility and the charge density of the device. When performing four-terminal measurement at cryogenic temperatures, small excitation signals (between 10 nA to 100 nA) are often used to prevent heating of the electrons in the sample out of thermal equilibrium

with their surrounding lattice and cryostat. This small signal is typically sourced at a low frequency (∼13 Hz) to eliminate parasitic capacitive electrical signals from the measurement [16]. A common way to produce such a small excitation signal is to use a voltage divider in series with the lock-in output. This will reduce the amplitude of the voltage sourced by the lock-in [1]. When the resistance of the device to be measured is unknown, we often connect a large (∼ MΩ) resistor, which sets an upper limit on the current passing through the device and prevents unexpected heating of the MXC.

3.4.2 Two-Terminal Measurements of Epitaxial Single-Crystal Halide Perovskites Devices

In the previous subsection, we discussed the advantages of performing four-terminal measurements. However, there are sometimes constraints regarding the sample that prevent four-terminal measurement from being feasible. In these cases, we can only make limited number connections to the surface of the sample and must perform two-terminal measurements with one pair of current-carrying and voltage-sensing electrodes.

This is the case for the quantum coherent transport measurements performed on the halide perovskites devices described in this dissertation. Here we briefly discuss how to perform these two-terminal measurements, and how we can derive the electrical conductivity and resistance of samples measured in this fashion. Figure 3.9 (a) and (b) show two schematics of the experimental setups for two-terminal transport measurements of $CsSnI_3$ and $CsSnBr_3$ thin film devices from Refs. [94, 135]. The equivalent circuit diagram representing the experimental setups in Figure 3.9 (a) and (b) is shown in Figure 3.9 (c). Here, V_{drive} is the voltage sourced from the lock-in and this lock-in simultaneously measures the current I flowing through the sample. The voltage drop across the gold contacts on the sample is V_m, which corresponds to the total device resistance R_t including the contact resistance R_c between a gold pad and the thin film as well as the resistance of the sample between the two god pads R_s.

Device geometry: Our $CsSnI_3$ and $CsSnBr_3$ samples have similar geometry. The overall sample size is 5 mm × 3 mm consisting of a halide (KCl for $CsSnI_3$ and NaCl for $CsSnBr_3$) single

[1] The SR830 lock-in can output a voltage from 0.04 V to 5 V

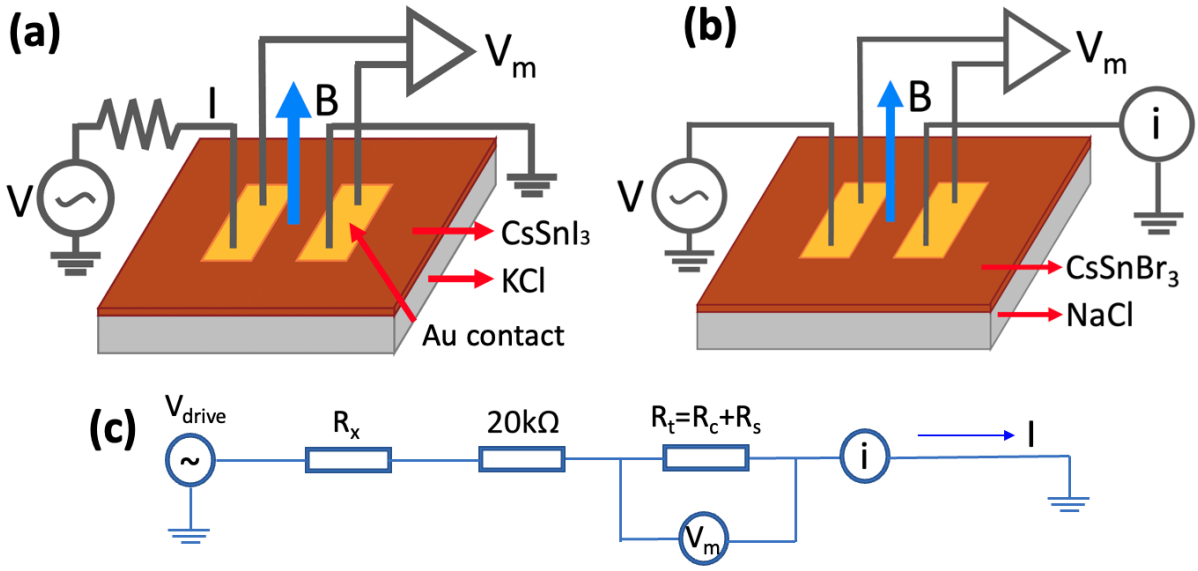

Figure 3.9: Two-terminal transport measurement of epitaxial $CsSnI_3$ thin film devices (a) and epitaxial $CsSnBr_3$ thin film devices (b). The current measured flows through the two gold contacts (yellow regions). (c) Equivalent electrical diagram of (a) and (b). R_x represents the resistance of an external current limiting resistor series with the total sample resistance.

crystal substrate. The thickness of epitaxial film grown on top of this substrate was 50 nm for $CsSnI_3$ and 30 nm for $CsSnBr_3$. Two gold contacts (0.5 mm × 2 mm with 50 μm separation) were e-beam evaporated to the top of the epitaxial film and these contacts had a thickness of 100 nm.

Two-terminal measurements of $CsSnI_3$ devices: The epitaxial $CsSnI_3$ devices studied showed relatively low resistance ($< 200\ \Omega$) at temperatures < 300 K. In the two-terminal measurements, we typically sourced a voltage $V_{\text{drive}} = 0.1$ V and used a series resistor $R_x = 10\ \text{M}\Omega$ to create a current I which flows through the two gold pads. This current can be treated as a constant due to the small resistance of our $CsSn_3$ device relative to R_x. In this setup, $I \approx \frac{0.1\,V}{10\,M\Omega+20\,k\Omega} = 9.98$ nA, consistent with what is measured independently via the lock-in amplifier. Then the total sample resistance is given by $R_t = V_m/I$. The conductance which corresponds to this resistance can then be derived from the known geometry of the device and an assumption of uniform current flow through the sample between the rectangular gold contacts.

Two-terminal measurements of $CsSnBr_3$ devices: In contrast to the $CsSnI_3$ samples, the

epitaxial $CsSnBr_3$ devices studied in this dissertation are highly resistive at temperatures < 10 K. As a consequence, for the low-temperature transport measurements, a large ballast resistor R_x is no longer needed. Additionally, the epitaxial single-crystal $CsSnBr_3$ devices showed a large negative magnetoresistance (see Chapter 5), so the current I varies dramatically as we increase or decrease the magnetic field. Thus, in the two-point measurements of the $CsSnBr_3$ devices, we independently measure the current I flowing through the circuit directly with a lock-in amplifier. The total device resistance is then given by $R_t = V_m/I$.

3.5 Preparation and Handling of Epitaxial Single-Crystal Halide Perovskite Devices

As described in Section 2.3, epitaxial single-crystal $CsSnI_3$ and $CsSnBr_3$ thin film devices are sensitive to air, and will decompose when exposed to ambient conditions. To prevent the decomposition of the devices in an oxygen-rich environment, we developed protocols to keep the $CsSnI_3$ and $CsSnBr_3$ devices in a high-vacuum or dry-nitrogen filled environment, from start to finish, during sample fabrication, transferring, and measurement.

3.5.1 Wiring-Up Samples in Glove Bag

Halide perovskite samples are properly sealed and transferred from growth chamber to our lab in a container that is completely isolated from air. This container includes two KF vacuum end blanks, a KF o-ring and a KF clamp (see Figure 3.10 (c)). To perform wire-up of the halide perovskite device on a chip carrier, we place our sample container into a glove bag (see Figure 3.10 (a)) containing an optical microscope and supplies needed for making electrical contact to the devices. The glove bag is purged with dry nitrogen gas before opening the sample containers. The level of humidity and oxygen in the bag are continuously monitored via commercial sensors.

When the oxygen level of the glove bag is sufficiently low, we open the sample container and transfer the samples to a 16 pin chip carrier (see Figure 3.10 (b)). This chip carrier is manufactured by Spectrum Semiconductor Materials (part number: CSB01652). It can be mounted to the

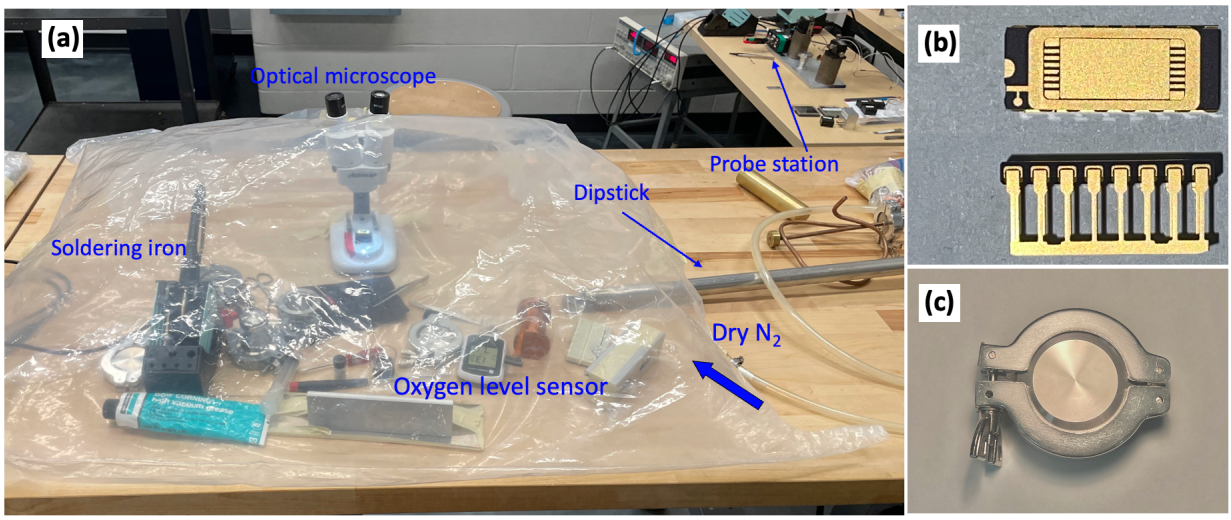

Figure 3.10: (a) Photo of the sample preparation glove bag. The location of optical microscope, soldering iron, oxygen level sensor, dipstick and dry nitrogen supply line are labeled. A nearby probe station can be placed into the glove bag when needed. (b) Top and side photos of the 16 pin chip carrier. (c) Photo of the sample container used to transport samples between labs.

common 18 pin sockets shown in Figure 3.11 (b) and 3.12 (a). The gold contacts on our halide perovskite samples are connected to the pads on chip carrier via gold wires. The typical solder joint between gold wire and contact pad is made of an indium-tin alloy. The soldering is performed using a Weller soldering station that can precisely control the temperature of the fine soldering tip. In addition, a probe station can be placed into the glove bag for checking sample and contact viability before low-temperature transport measurements.

3.5.2 Measurement at Liquid Nitrogen Temperature

Before performing measurement on halide perovskite devices at millikelvin temperatures, we first check the low-temperature viability of a device and its electrical contacts. To do this, we perform transport measurements at liquid nitrogen temperature $T = 77$ K by using a "dipstick" (see Figure 3.11 (a)). The dipsitck consists of a breakout box similar to the one in Figure 3.6 (b) and an 18-pin socket connector (see Figure 3.11 (b)). At the end of the dipstick, both the chip carrier and a brass cap with a silicon diode temperature sensor (see Figure 3.11 (c)) are connected. This

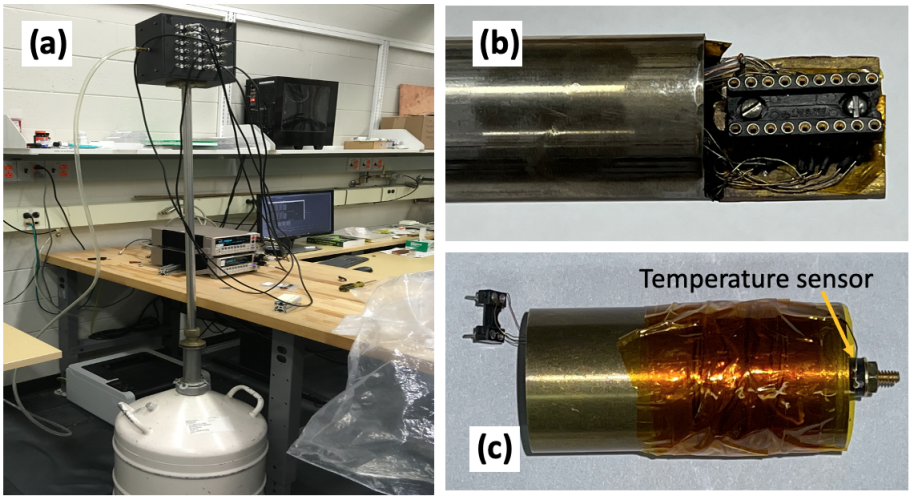

Figure 3.11: (a) Dipstick and nitrogen dewar for temperature dependent characterization of halide perovskite thin film devices down to 77 K. (b) 18-pin socket at the end of the dipstick for mounting the halide perovskites device. (C) A brass cap with diode temperature sensor. The cap can be connected to the end of the dipstick electrically and mechanically.

temperature sensor is made by Cryocon (part number: S950-A-BB), and has a wide temperature range (1.4 K to 370 K). We use a Keithley Series 2400 source meter (in 4-wire mode) to record the voltage across the temperature sensor and convert the voltage to temperature using the manufacturer provided calibration. The dipstick is also outfitted with a connection for flowing dry nitrogen during cool-down and warm-up of the device to prevent exposure to moisture in the air. Before the liquid nitrogen measurement, the lower end of the dipstick is kept inside the glove bag and the sample can be loaded onto the dipstick without exposing it to air (see Figure 3.10 (a)).

3.5.3 Hermetically Sealed Sample Cell

A hermetically sealed sample cell is used for low-temperature (10 mK) and high-magnetic field (14 T) measurements. The body of the cell is made of OFHC copper and the sample is attached to an 18-pin chip carrier within the cell. The device is loaded into this cell within a dry nitrogen environment in the glove bag and the cell is sealed with a conventional indium O-ring compatible with cryogenic measurements. The sample cell is then mounted onto the cold finger of the DR. To

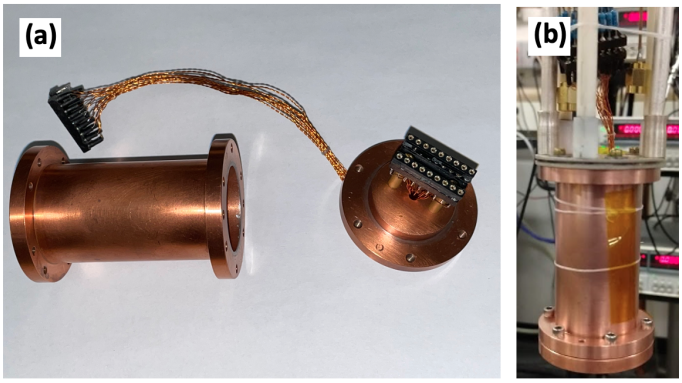

Figure 3.12: Hermetically sealed sample cell for low-temperature halide perovskites measurements in the LD400 DR.

check if the cell is hermetically sealed, after loading the cell onto the DR, we perform a resistance versus time measurement of the halide perovskite device to make sure the device is not in the process of degrading due to an air leak into the cell.

CHAPTER 4

QUANTUM INTERFERENCE AND WEAK ANTI-LOCALIZATION IN EPITAXIAL $CsSnI_3$

4.1 Introduction

In this chapter, measurement results of quantum coherent transport and localization of charges in epitaxial single-crystal $CsSnI_3$ thin films will be presented. A comprehensive discussion of weak localization (WL) and weak anti-localization (WAL) will be given in this chapter to interpret the measured data and discuss the experimental results. The observation of WAL and long charge carrier phase coherence length in an epitaxial $CsSnI_3$ devices will be presented, along with a possible explanation regarding the origin of the spin-orbit interaction in this material. These results represent the first observation of long charge carrier phase coherence length in epitaxial halide perovskites. Much of this chapter will cover the results presented in Ref. [94].

4.2 Electrical Conductivity in the Drude Model

The electrical conductivity σ is one of the most important physical parameters of a low-dimensional system. The way to obtain it is using Ohm's law. The vector form of Ohm's law is:

$$\vec{j} = \sigma \vec{E}\,, \tag{4.1}$$

where $\vec{j}$ is the current density and $\vec{E}$ is the electric field. Ohm's law shows that if there is an electric field applied across a low-dimensional system, a current density will flow through the system, and this current density is dictated by the conductivity of the material, which will be a tensor in its general form (see Subsection 1.3.2).

The Drude model proposed by Paul Drude [23], is a classical model to explain how electrons move inside materials. It is an application of the kinetic theory of gases to systems in which charged particles can move. The most fundamental idea of this model is to treat the microscopic behavior

of electrons in a classical way. The Drude model assumes that electrons are constantly bouncing between impurities or defects in a material while propagating in a straight line between scattering centers, and the electrons do not interfere with each other. The time between each collision is identical and independent of electron's velocity and position. The conductivity in the Drude model can be derived using the following method. Consider an electron with velocity v and charge $-e$. Then, a system with charge density n, will have current density:

$$\vec{j} = -ne\vec{v}\,. \tag{4.2}$$

The electron velocity $\vec{v}$ will be zero if there is no applied electric field. When the electric field is applied, the electron will pick up the following velocity:

$$\vec{v} = \vec{v_0} - \frac{e\vec{E}t}{m}\,, \tag{4.3}$$

where t is the time passed since the last collision and v_0 is the electron velocity after the last collision. If we average Equation 4.1 over time we can eliminate v_0. By taking the time average, we can also replace time t with the average scattering time between collisions, i.e. the relaxation time τ. If we then consider Equations 4.1, 4.2, and 4.3, we get the following relationship between the current density $\vec{j}$ and the electric field $\vec{E}$:

$$\vec{j} = \left(\frac{ne^2\tau}{m}\right)\vec{E}\,. \tag{4.4}$$

The conductivity $\frac{ne^2\tau}{m}$ here is called the Drude conductivity. This model has been applied to a variety of electrically conducting systems such as metals. However, one can see shortcomings of this model. One of the shortcomings is that the electrons will not interact with the electric field created by other moving electrons, i.e. electron-electron interactions are not included in this model. Also, whether electrons can be treated as classical particles is often questionable. The de Broglie wavelengths of electrons are on the nanometer scale at low temperatures. This means that electrons cannot be treated as classical particles at low temperatures (since they have substantial wave character) under the conditions of the Drude model [46]. In particular, quantum interference will need to be added to the model to accurately describe many low-temperature phenomena.

4.3 Quantum Transport in Solids

4.3.1 Characteristic Length Scales in Different Transport Regimes

We want to first start by describing the different characteristic lengths associated with electronic transport in solids in the quantum regime. Due to interference effects, the transport behavior of charge carriers can be strongly influenced by these length scales in the quantum regime. These relevant characteristic lengths are the followings [80]:

- **The macroscopic scale of the sample L**: L can be either the length or the width of a thin film sample.

- **The mean free path l:** The mean free path l is the average distance over which a moving charge carrier propagates before substantially changing its momentum due to potential scattering with scattering centers in the material. The mean free path is related to the concept of the relaxation time τ, which is the average time over which the momentum of the charge carrier is reversed through a series of scattering events in the material. The relation between the mean free path and relaxation time τ is $l = v_F \tau$, where v_F is the Fermi velocity [58].

- **The phase coherence length l_ϕ:** The phase coherence length l_ϕ is the average distance that a charge carrier can travel before losing its phase coherence. The average time that elapses between dephasing events τ_ϕ is also associated with the quantum phase coherence, and is called phase coherence time. In the quantum diffusive transport regime $l_\phi = \sqrt{D\tau_\phi}$, where D is the charge carrier diffusion constant [10].

Due to rapid advances in the high-quality growth and fabrication of mesoscopic and nanoscale structures, it is possible to study different materials in which the average impurity spacing is about the same as the sample dimensions. Thus, it is important to distinguish different transport regimes so that we can clearly understand the observed phenomena and the relation between different length scales relevant to quantum transport.

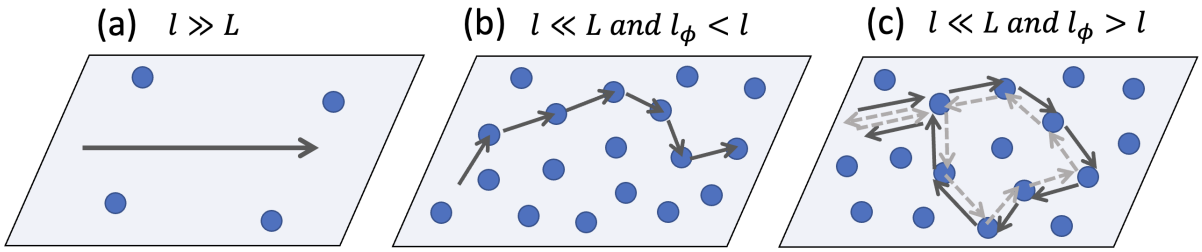

Figure 4.1: Schematic illustration of different electronic transport regimes in solids [80]. The blue dots represent impurities (scattering centers) and arrows mark the trajectories that charge carrier travel. (a) Ballistic transport regime. (b) Semi-classical diffusive transport regime. (c) Quantum diffusive transport regime. Notice that both (b) and (c) belong to diffusive transport regime.

Ballistic transport happens when l is much greater than the sample dimension. In this regime, there will be no scattering when the charge carriers transport through the sample (see Figure 4.1 (a)) due to a low amount of impurities. In contrast, when l is much less than L, the sample will be in a diffusive transport regime, as shown in Figure 4.1 (b) and (c). In the diffusive transport regime, the disorder scattering of charge carriers will dominate the sample's transport behavior. In Figure 4.1 (b), the charge carrier's phase coherence length l_ϕ is less that l, and quantum effects are negligible. This is the regime that can be explained by Drude's electrical conductivity theory and it is called the semi-classical diffusion regime. In Figure 4.1 (c), when l_ϕ is greater that l, electrons will maintain their wavefunction phase coherence even after being scattered many times. The scattering events in each electron's diffusive trajectories are elastic and this regime is called quantum diffusive regime. As we will see, it is this regime which will be most relevant to our experiments on $CsSnI_3$.

4.3.2 Phase Coherence in Quantum Diffusion

In the quantum diffusive regime shown in Figure 4.1 (c), the phase coherence of the electron wavefunction is important. This wave function can be described by the following expression:

$$\psi(\vec{x}, t) = |A_0| \exp\left(i\vec{k} \cdot \vec{x} - \frac{iEt}{\hbar}\right) . \tag{4.5}$$

In the equation above, a change of phase can be caused by any change of the position, momentum or energy in the electron's wavefunction. The phase coherence length l_ϕ is a measure of the distance that the electron propagates phase coherently before its phase is randomized by inelastic scattering. During an elastic scattering event at an impurity, the phase of an electron is not randomized, it is only shifted by well-defined amount. If a second electron propagates along the identical path, the phase accumulation will be exactly the same, i.e. phase coherent with the first electron. Quantum diffusion will occur when electrons can on average keep their phase coherence over a relatively long distance so that $l_\phi > l$. This is in strong contrast to inelastic scattering events, where the scattering produces changes in the energy of the electrons over time. In this case, the phase shift that the electrons acquire is different each time and produces loss of phase coherence [132]. The phase coherence in the quantum diffusive regime opens the door for the coherent interference between different electron's trajectories and thus leads to the observation of a variety of physical phenomena, including localization of charges, Aharonov-Bohm oscillations [103] and Universal Conductance Fluctuations (UCF) [72].

4.4 Weak Localization in Two-dimensional Electron Systems

4.4.1 Weak Localization

Constructive interference between the trajectories of charge carriers results in weak localization (WL) in the quantum diffusive regime at sufficiently low temperatures. In Figure 4.2, where an electron moves in a conductor from point A to B, the transport can happen along different paths which are shown as yellow arrows. In this case, we assume the electron's mean free path l is less than $\overline{AB}$ so there will be multiple elastic scattering events in the electron's diffusive transport trajectories Additionally, we assume $l_\phi > l$, which means the phase coherence length is longer than $\overline{AB}$, so the electron's phase is preserved after many scattering events. In this situation, there is a possibility that the electron can scatter elastically in a clockwise loop trajectory starting at point M with (gray arrows in Figure 4.2). This loop trajectory can constructively interfere with its time-reversed counterclockwise partner (red arrows in Figure 4.2) and the interference between the

two trajectories leads to an overall increase of the device's resistance, which is known as WL (also sometimes called coherent backscattering).

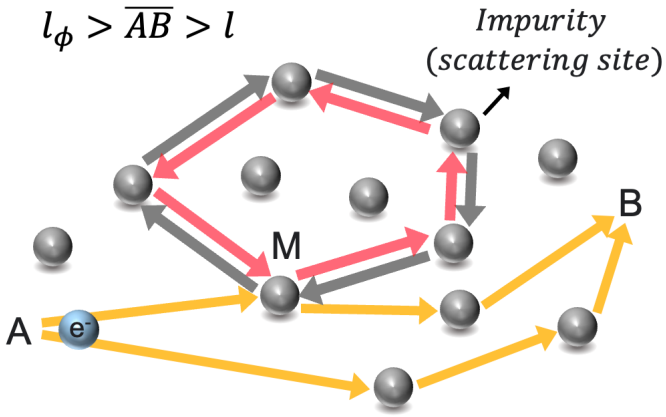

Figure 4.2: Qualitative picture of WL showing possible electrons trajectories from point A to B. The grey dots are impurities (sites of elastic scattering). Grey (red) arrows show clockwise (counterclockwise (time-reversed)) diffusive trajectories. The hierarchy of different length scales is shown in this figure.

To quantitatively describe WL, we will start the derivation using the theory of the Feynman path [31], and each path will be indexed by i. An electron keeps its phase coherence along an individual path i when it is transported from point A to B. We can write the Feynman path's amplitude for trajectory i as:

$$A_i = a_i \exp(i\phi_i)\,, \tag{4.6}$$

where ϕ_i is the total phase that the electron accumulates along path i, and a_i is a complex coefficient. The phase ϕ_i is defined in the following way:

$$\begin{aligned} \phi_i &= S_i/\hbar \\ S_i &= \int_{t_A}^{t_B} dt\; L(\vec{r},\dot{\vec{r}},t)\;\;, \end{aligned} \tag{4.7}$$

where the integral S_i is the non-relativistic action and $L(\vec{r},\dot{\vec{r}},t)$ is the Lagrangian function of the freely propagating electron. The times t_A and t_B are when the electron starts at point A and stops

at point B. Then the total amplitude for the electron traveling from A to B will be the sum of each individual path, and the total probability of the electron travelling from A to B will be:

$$P_{AB} = \left| \sum_i A_i \right|^2 = \sum_i |A_i|^2 + \sum_{i \neq j} \mathrm{Re} A_i A_j^* \,. \tag{4.8}$$

In Equation 4.8, A_i^* is the complex conjugate of A_i. In the case of WL, the electron's diffusive trajectory and its time-reversed partner will interfere constructively with each other as shown in Figure 4.2, and we can denote the two trajectories as $A_1 = a_1 \exp(i\phi_1)$ and $A_2 = a_2 \exp(i\phi_2)$, where $a_1 = a_2$ and $\phi_1 = \phi_2$. If we calculate the total probability of the carriers returning to the starting point M, then we can find:

$$P_{MM} = |A_1 + A_2|^2 = |A_1|^2 + |A_2|^2 + [A_1 A_2^* + A_2 A_1^*] = 4\,|A_1|^2 \,. \tag{4.9}$$

The result given in Equation 4.9 is distinct from the result one would obtain for the classical diffusive case. In the classical diffusive case, we do not need to consider the quantum interference terms in the calculation of P_{MM} and thus $P_{MM} = |A_1|^2 + |A_2|^2 = 2\,|A_1|^2$. Therefore the interference in the quantum diffusive case causes an increase in the probability of finding the electron at the starting point M relative to the classical prediction. It is important to note here that constructive interference occurs for all possible closed loops in the conductor, and is therefore not averaged out. As a result, the total resistance is increased compared to the classical case.

4.4.2 Spin-orbit Interaction and Weak Anti-localization

In the discussion of the previous subsection, we have ignored the effect of the electron's spin on the interference between electron trajectories. The effect of spin can be ignored in some materials if the spin is conserved (i.e. not changed) along the electron's diffusive trajectory. In materials with strong spin-orbit coupling (SOC), the effect of the spin cannot be ignored and can lead to destructive interference, also known as weak anti-localization (WAL) and was originality demonstrated and explained by Bergmann [9]. A general explanation of the SOC effect can be described as the following. When an electron propagates in a closed loop, the electrons sees its nearby ion cores as

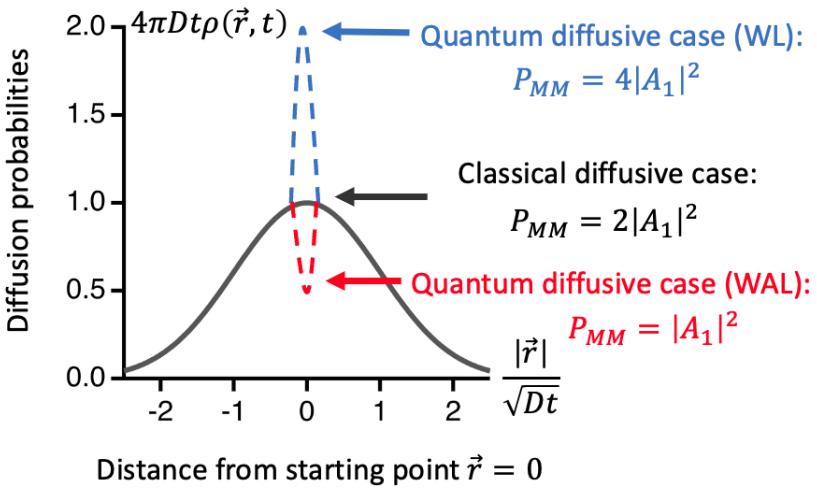

Figure 4.3: Probability distribution of electron diffusion in two-dimension. The electron starts at point M in Figure 4.2 where $\vec{r} = 0$. The black trace represents the classical diffusive case, where the probability has the form $\rho(\vec{r},t) = [1/(4\pi Dt)]\exp\left(-|\vec{r}|^2/4Dt\right)$. The blue dashed trace represents the quantum diffusive case in WL and its probability is twice that of the classical case. The red dashed trace represents the quantum diffusive case in WAL and its probability is half of the classical result.

moving charges. The moving charges create a local magnetic field that rotates the electron's spin as shown in Figure 4.4 [9].

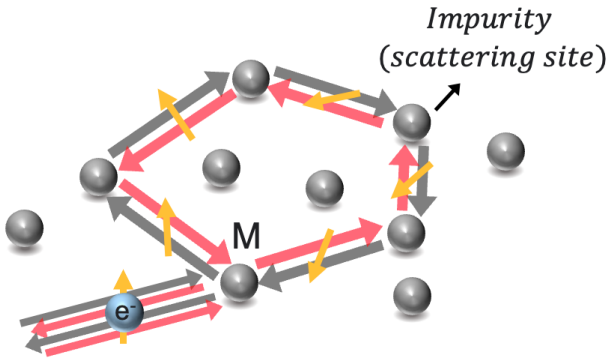

Figure 4.4: Qualitative picture of WAL. An electron's spin state is shown in this figure. Notice that as the electron propagates along the loop trajectory, the its spin is rotated due to the strong SOC of the system.

We will discuss the detailed underlying mechanism of the spin rotation and SOC later in

Section 4.5. Here we will simply define change of the spin state due to different scattering sites in the loop trajectory using a generic rotation matrix R [32]. This rotation matrix R is shown in Equation 4.10 and can act on the spin of the electron and help us to derive the destructive interference observed in WAL,

$$R = \begin{pmatrix} \cos\left(\frac{\alpha}{2}\right) \exp\left[i(\frac{\beta+\gamma}{2})\right] & i\sin\left(\frac{\alpha}{2}\right) \exp\left[-i(\frac{\beta-\gamma}{2})\right] \\ i\sin\left(\frac{\alpha}{2}\right) \exp\left[i(\frac{\beta-\gamma}{2})\right] & \cos\left(\frac{\alpha}{2}\right) \exp\left[-i(\frac{\beta+\gamma}{2})\right] \end{pmatrix}. \tag{4.10}$$

In Equation 4.10, α, β, γ are Euler's angles that define the orientation of a coordinate frame x', y', z' relative to another frame x, y, z. One can easily check that the matrix R here is a unitary matrix that has the following properties:

$$\begin{aligned} R^{\dagger} R &= 1 \\ R^{-1} &= R^{\dagger}, \end{aligned} \tag{4.11}$$

where $R^{\dagger}$ is the Hermitian conjugate (or adjoint) matrix of R, and R^{-1} is the inverse matrix of R. Let us define the initial spin state of an electron as $|s\rangle$. Then we can define the final spin state of the electron propagating in a clockwise trajectory as $|s_1\rangle$ and the final spin state of the electron propagating in a counterclockwise trajectory as $|s_2\rangle$. After the scattering events, the two resultant electron spin states and their original spin state $|s\rangle$ have the following relation:

$$\begin{aligned} |s_1\rangle &= R\,|s\rangle \\ |s_2\rangle &= R^{-1}\,|s\rangle\,. \end{aligned} \tag{4.12}$$

In Equation 4.12, we have used the fact that the R^{-1} physically corresponds to rotation in the opposite sense. The interference between the two trajectories becomes,

$$\langle s_2|s_1\rangle = \langle s|(R^{-1})^{\dagger} R|s\rangle = \langle s|R^2|s\rangle\,, \tag{4.13}$$

where R^2 in Equation 4.13 has the following form:

$$R^2 = \begin{pmatrix} \cos^2(\frac{\alpha}{2}) \exp[i(\beta+\gamma)] - \sin^2(\frac{\alpha}{2}) & \frac{i}{2}\sin(\alpha)[\exp(-i\beta) + \exp(i\gamma)] \\ \frac{i}{2}\sin(\alpha)[\exp(i\beta) + \exp(-i\gamma)] & \cos^2(\frac{\alpha}{2}) \exp[-i(\beta+\gamma)] - \sin^2(\frac{\alpha}{2}) \end{pmatrix} \tag{4.14}$$

The Equation 4.14 can be classified into two different categories, one without SOC, another with strong SOC.

(I) System without SOC.

When the system lacks SOC the electron's spin will not be rotated, so $\alpha = \beta = \gamma = 0$. In this case, R^2 will be an identity matrix I and there will be no spin-orbit correction to Equation 4.9. This is simply the case for WL where $P_{MM} = 4\,|A_1|^2$.

(II) System with SOC.

In the system with strong SOC, the electron's spin will be rotated during the electron propagation along the loop trajectory. If we consider all the possible diffusive trajectories for electrons along loops in a conducting material, we find an overall destructive interference. This overall destructive interference is equivalent to an average over all the matrix elements of R^2 since the rotation angles can take on any values. After taking average values of matrix elements at all angles, we get $R^2 = (-1/2) \cdot I$. If we apply this quantum correction to Equation 4.9, we can find $P_{MM} = 2\,|A_1|^2 - (1/2) \cdot 2\,|A_1|^2 = |A_1|^2$ which is distinct from WL. Specifically, P_{MM} in WAL is half of the classical diffusive case, which is shown in Figure 4.3. This means in the case of WAL, the electron is more likely to move away from its starting location M after time t passed, which leads to an overall decrease in the resistance of the material.

4.4.3 Effect of Magnetic Field on Weak (Anti-)Localization

It turns out that a magnetic field can be used to reveal and investigate localization in the quantum diffusive regime. In the classical theory, if we apply magnetic field to the metal, the change in resistance will be proportional to $(\omega_c\tau)^2$, where $\omega_c = eB/m^*$ is the cyclotron frequency, and m^* is the electron's effective mass [58]. In the case of a thin metal film, the sample's resistance should be almost magnetic field independent. For example, consider a copper (Cu) thin film with 10 nm thickness. Since the mean free path l for the electrons in this Cu film are on the order of the film thickness, we can assume $l = 10$ nm [10], and m^* is almost equal to free electron mass. By calculation we can find $(\omega_c\tau)^2 \approx 10^{-4}$ at $B = 10$ T, which is negligibly small, and shows we do not classically expect to see magnetoresistance in thin metal films even at large magnetic field [10]. In contrast, the magnetoresistance data of a Cu thin film at low temperatures (see Figure 4.5) shows a

significant discrepancy with what is expected from this simple calculation [10]. The observation of this discrepancy arises from quantum interference and lead to the discovery of WL (WAL).

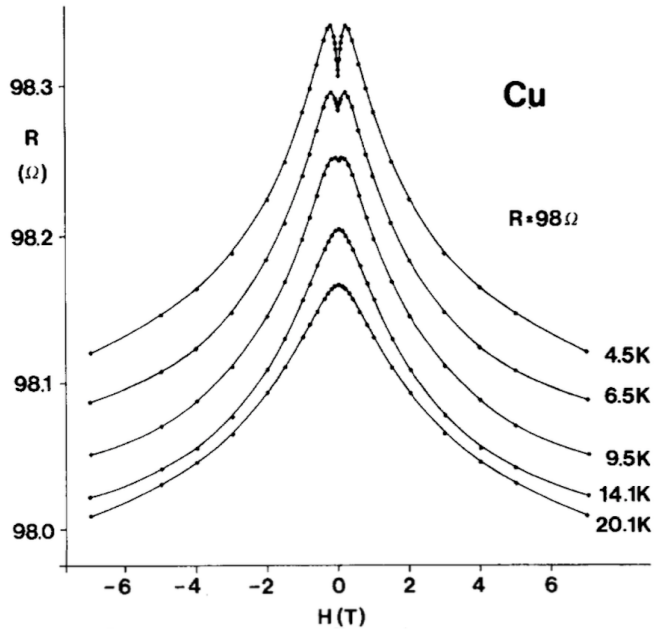

Figure 4.5: The magnetoresistance of a thin Cu-film (thickness of 10 nm) at low temperatures [10]. All data traces show features of WL. Starting from 9.5 K, a WAL feature is also observed, which is manifest as the local minimum in resistance near zero magnetic field.

To understand the observation of WL (WAL) and the role of magnetic field, let us first start with the electron's Lagrangian function in Equation 4.7 [132]. If an external magnetic field is applied normal to the plane of a thin film sample containing electrons with charge $-e$, the Lagrangian function will be of the following form:

$$L(\vec{r}, \dot{\vec{r}}, t) = \frac{1}{2} m \dot{\vec{r}}^2 - e\vec{r} \cdot \vec{A}\,, \tag{4.15}$$

where $\vec{A}$ is the vector potential and $\vec{B} = \nabla \times \vec{A}$ is the magnetic field. The first term on the right hand side of Equation 4.15 will produce a fixed phase ϕ_i in Equation 4.7 for a given loop trajectory. The second term on the right hand side of Equation 4.15 will produce an additional phase to the electron's Feynman path amplitude caused by the external magnetic field. If we consider that the

electron travels in a clockwise loop, this additional phase term ϕ_p will be given by:

$$\phi_p = \frac{e}{\hbar}\oint \vec{A}\cdot d\vec{L} = \frac{e}{\hbar}\iint (\nabla\times\vec{A})\cdot d\vec{s} = \frac{e}{\hbar}\iint \vec{B}\cdot d\vec{s} = \frac{eBs}{\hbar}\,. \tag{4.16}$$

In Equation 4.16, s is the area enclosed by the loop trajectory. In WL (WAL), we can assume $a_1 = a_2 = a$ and $\phi_1 = \phi_2 = \phi$, and the two different Feynman path amplitudes for the electron will be:

$$\begin{aligned} A_1 &= a e^{i\phi} e^{i\phi_p} \\ A_2 &= a e^{i\phi} e^{-i\phi_p}\,. \end{aligned} \tag{4.17}$$

When we apply these amplitudes to Equation 4.9 and consider the effect of SOC, we arrive at:

$$\begin{aligned} \text{WL:}\quad & P_{MM} = 2a^2\left[1+\cos\left(2\phi_p\right)\right] && (a) \\ \text{WAL:}\quad & P_{MM} = 2a^2\left[1-\frac{1}{2}\cos\left(2\phi_p\right)\right]. && (b) \end{aligned} \tag{4.18}$$

We will consider WL as an example to discuss what we can observe if we apply an external magnetic field B to the system at low temperatures. In Equation 4.18(a), if $B = 0$, P_{MM} will be $4a^2$, similar to Equation 4.9. With the application of an increasing B we find a gradually decreasing device resistance. This decreasing resistance arises from the breaking of the constructive interference of the diffusive loop trajectories of electrons. If we continue to increase B, one would expect an oscillatory resistance from Equation 4.18(a). However, the measured data in Figure 4.5 show no oscillation, but rather a continuously decreasing resistance, see Figure 4.6 (a). This is because the value of ϕ_p in Equation 4.18 is associated with the area of single loop trajectory. In reality, there will be multiple loops in the device and an increasing B will first break the constructive interference of large loops and then subsequently smaller and smaller loops. In this fashion the measurement will average over these oscillations and only a decreasing resistance will remain. In the case of WAL, the additional phase associated with the rotation of electron spin will lead to a gradually increasing device resistance with applied field due to destructive interference, as shown in Figure 4.6(b).

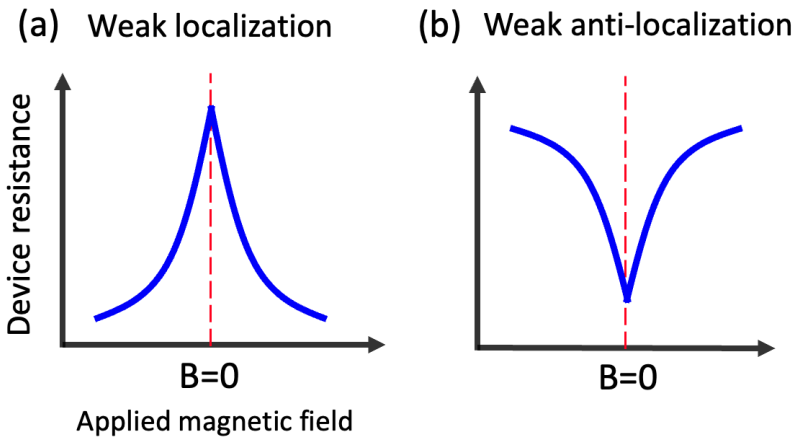

Figure 4.6: Schematic magnetoresistance of devices showing (a) WL, (b) WAL features. The saturation of the device resistance at relatively large field is caused by the averaging of different loop trajectories of electrons.

4.5 Spin-Orbit Coupling and Origins of Inversion Symmetry Breaking

In this section, we will first describe the relation between SOC in a system lacking inversion symmetry. Then, we will illustrate possible origins of the inversion symmetry breaking that are associated with the systems we study.

When the relatively slow electron ($(\frac{v}{c})^2 \ll 1$, where v is the speed of the electron and c is the speed of light) moves in an electric field $\vec{E}$, it will experience a effective magnetic field in its rest frame that is given by the standard Lorentz transformation:

$$\vec{B}_{eff} \approx \frac{\vec{E} \times \vec{p}}{mc^2}, \tag{4.19}$$

where $\vec{p}$ is the electron momentum and m is its mass. This effective magnetic field can induce a momentum-dependent Zeeman effect, which is referred as SOC and described by the following Hamiltonian:

$$H_{so} = \mu_B \, \vec{B}_{eff} \cdot \vec{\sigma} \approx \mu_B \, \frac{(\vec{E} \times \vec{p}) \cdot \vec{\sigma}}{mc^2}. \tag{4.20}$$

In crystals, the electric crystal field is given by $\vec{E} = -\nabla V$, where V is the gradient of the crystal potential. This leads to a spin-orbit field in the system which is given by:

$$\vec{W}(\vec{p}) = -\mu_B \frac{(\nabla V \times \vec{p})}{mc^2}. \tag{4.21}$$

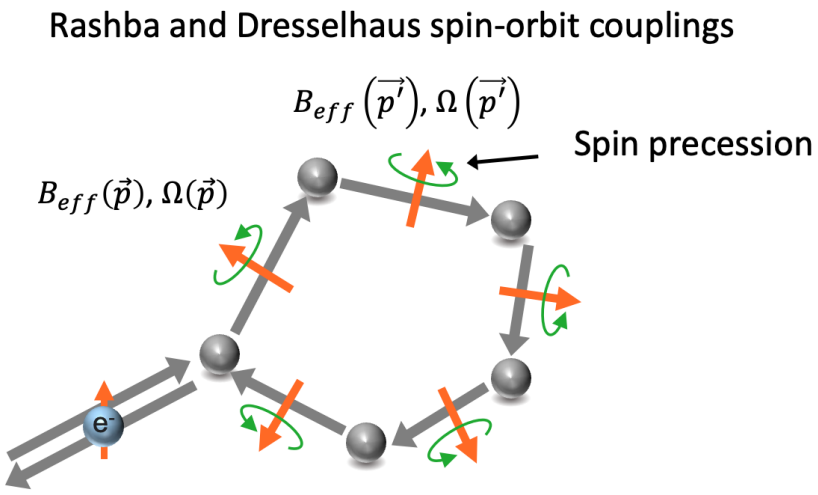

Figure 4.7: Typical clockwise scattering trajectory of an electron with spin scatterings at the impurities. Change of spin state can be caused by Rashba and Dresselhaus effects. The electron spin precesses around the internal effective magnetic fields, and spin's direction may change after each scattering event.

Since SOC preserves time-reversal symmetry, we have $\vec{W}(\vec{p}) \cdot \vec{\sigma} = -\vec{W}(-\vec{p}) \cdot \vec{\sigma}$. So the spin-orbit field must be an odd function in electron momentum $\vec{p}$:

$$\vec{W}(-\vec{p}) = -\vec{W}(\vec{p})\,. \tag{4.22}$$

The above equation shows that SOC will appear in systems with inversion asymmetry [83] and that SOC will remove spin-degeneracy. Different origins of inversion asymmetry can lead to different SOC effects. Inversion asymmetry can be produced by the application of a homogeneous external electric field normal to the plane of a 2DES heterostructure. This type of inversion symmetry breaking is called the Rashba SOC effect [136]. Bulk inversion asymmetry can also arise in some materials such as zinc-blende semiconductors and leads to Dresselhaus SOC [54].

The Rashba SOC:

The Rashba SOC Hamiltonian H_R has the following form when the interfacial confining electric field $\vec{E}$ is along the z-direction ($\vec{E} = E_z\hat{z}$):

$$H_R = \left(\frac{\alpha_R}{\hbar}\right)(\hat{z} \times \vec{p}) \cdot \vec{\sigma}\,, \tag{4.23}$$

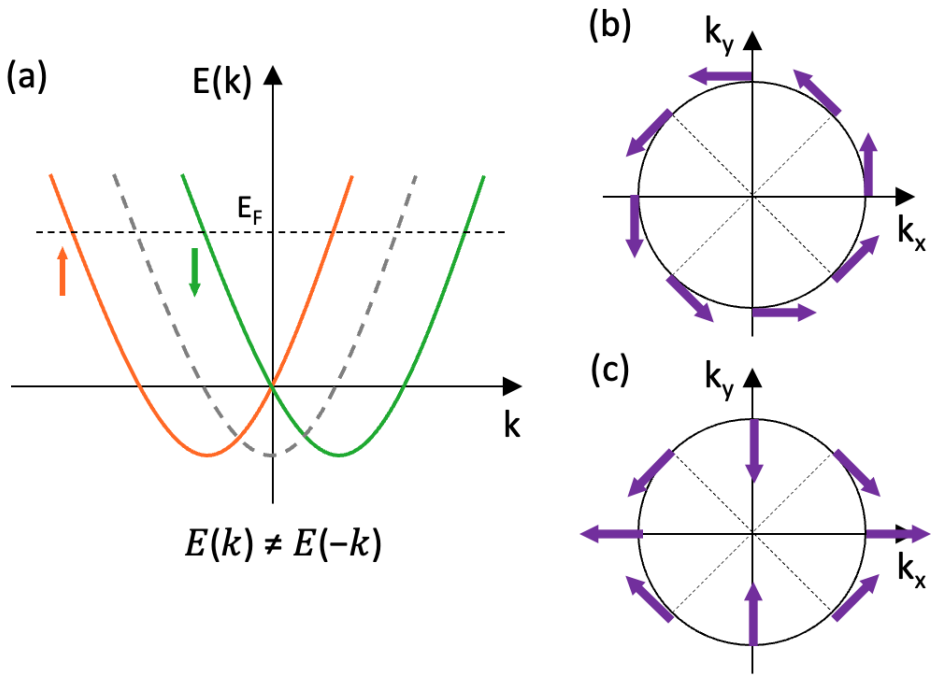

Figure 4.8: (a) The SOC from inversion asymmetry of material breaks up the spin-degenerate states which are indicated by the orange and green curve.s The gray dashed curve shows the spin-degenerate states in a material that has inversion symmetry. Momentum space spin textures in case of (b) the Rashba effect and (c) a linear Dresselhaus effect with strain applied along (001) direction [83].

where α_R is the Rashba parameter, which can be tuned by the applied confining voltage when a metal gate is present.

The Dresselhaus SOC:

When the Dresselhaus effect is applied to a 2D system in which the growth direction is along the (001) direction, the Dresselhaus SOC Hamiltonian H_D is linear in form:

$$H_D = \left(\frac{\gamma p_z^2}{\hbar}\right)(p_x\sigma_x - p_y\sigma_y)\,, \tag{4.24}$$

where γ is the Dresselhaus coefficient which depends on the material and cannot be tuned.

As we can see from Equation 4.23 and 4.24, both Rashba and Dresselhaus effects lock the spin to the linear momentum and split the spin sub-bands in energy. Additionally, each of them shows unique spin textures at the Fermi surface (see Figure 4.8) [83]. The Dresselhaus and Rashba effects lead to a effective magnetic field $B_{eff}(\vec{p})$ which is determined by the electron's momentum at

different scattering centers. This B_{eff} will act and exerts a torque on the spin, so that the spin will precess around it at the Larmor precession frequency $\Omega(\vec{p})$ (see Figure 4.7).

4.6 Long Phase Coherence Length and Weak Anti-localization in $CsSnI_3$

Up to here, we have described the quantum nature of WL (WAL) in a material in the quantum diffusive regime. Next, we will show the first realization of WAL in epitaxial single-crystal halide perovskite thin films.

4.6.1 Temperature-Dependent Electrical Properties of Epitaxial $CsSnI_3$

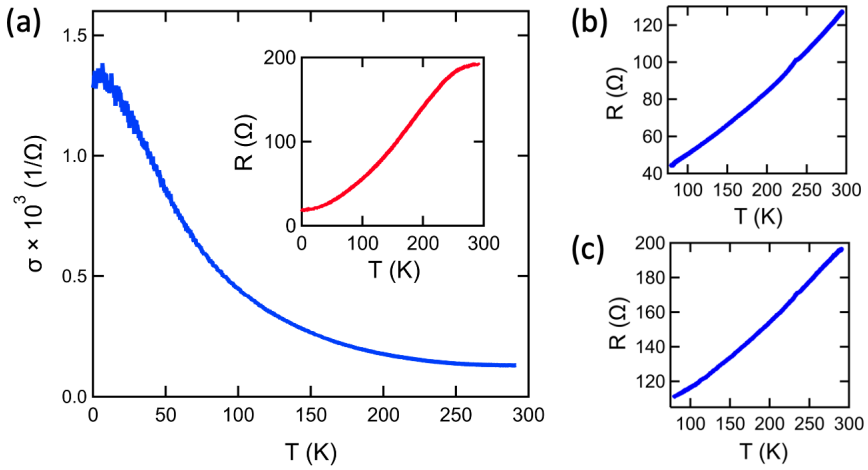

Figure 4.9: (a) Electrical conductivity σ of an epitaxial $CsSnI_3$ thin film as a function of temperature with magnetic field $B = 0$. Inset: the corresponding device resistance R versus temperature. (b) and (c) Two additional epitaxial $CsSnI_3$ thin film show similar temperature-dependent resistance behavior.

In this subsection, we will present the temperature-dependent resistance behavior of our eptiaxial $CsSnI_3$ device, which reveals the relatively large charge carrier density in this material. Figure 4.9 (a) shows the conductivity σ of a $CsSnI_3$ epitaxial film as the sample was cooled from room temperature down to $T = 16$ mK (we present measurements on additional two $CsSnI_3$ devices which are cooled down to liquid nitrogen temperature (T=77 K) in Figure 4.9 (b) and (c), which show similar behavior). These measurements were performed using standard low-frequency lock-

in techniques (see Subsection 3.4.2 for more detail). The overall low measured device resistance indicates that the gold makes good Ohmic contact to the $CsSnI_3$.

The conductivity of the device increases with decreasing temperature, indicating that the presence of mobile charge carriers do not freeze out upon cooling to low temperature. This increase in the conductivity is consistent with a reduction in phonon density upon lowering the temperature of the device. The existence of charge carriers in the material is likely the result of intrinsic doping in the epitaxial $CsSnI_3$, which is a direct bandgap semiconductor in its epi-tetragonal phase (see Figure 2.2 and Table 2.1). It turns out that previous electrical conductivity measurements on orthorhombic $CsSnI_3$ have also reported metal-like conduction attributable to hole-doping associated with Sn vacancies [127]. Furthermore, we see no evidence in the resistance for phase transformations in the temperature dependent resistance measurements over multiple devices.

4.6.2 The Observation of Weak Anti-localization in $CsSnI_3$

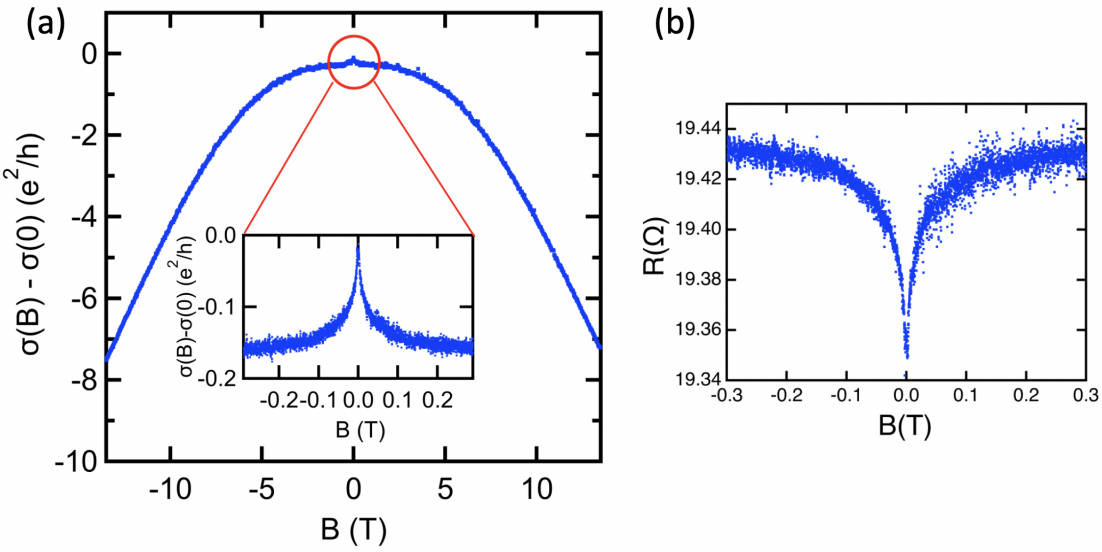

Figure 4.10: (a) Magnetoconductivity of the epitaxial $CsSnI_3$ thin film as a function of magnetic field at $T = 16$ mK. The vertical axis is the magnetoconductivity $\sigma(B)$ minus the value of the conductivity at zero magnetic field $\sigma(0)$. Inset of (a): low field magnetoconductivity showing a clear weak anti-localization peak at $B = 0$ and the WAL curvature extends to $B = \pm 0.3$ T. (b) Low field magnetoresistance data that shows the WAL peak only varies the overall resistance by 0.5%.

In the previous subsection, we discussed the temperature-dependent conductivity of epitaxial $CsSnI_3$ film device without applying magnetic field, and the result shows charge carriers do not freeze out upon cooling to low temperature. At low-temperatures, the application of a magnetic field normal to the plane of the $CsSnI_3$ layer strongly modifies the transport of these charge carriers. Figure 4.10 (a) presents the conductivity of a $CsSnI_3$ epitaxial film device as a function of magnetic field up to $B = \pm 13.5$ T. Above several Tesla, there is a non-saturating magnetoconductivity which is approximately linear to the applied field. This apparent reduction in the conductivity with increasing magnetic field likely arises from a convolution of the longitudinal conductivity measurement by the Hall voltage across the sample due to the two-terminal geometry of our device (see Subsection 3.4.2 for details). The fact that the gold pads (voltage probes) on our $CsSnI_3$ sample are comparable to the sample size leads to the formation of so-called "hot-spot" near corners of the pads [60, 109, 116]. This effect is common in magnetotransport measurements and often observed in 2DESs in semiconductors [30, 109] and graphene [116]. More importantly, the low-field magnetoconductivity can be used to reveal signatures of coherent quantum phenomena. The inset of Figure 4.10 (a) shows the change in the magnetoconductivity $\sigma(B) - \sigma(0)$ near zero magnetic field at $T = 16$ mK. The upward cusp in $\sigma(B) - \sigma(0)$ in the vicinity of $B = 0$ is the characteristic signature of charge carrier WAL in quantum diffusive magnetotransport. The observation of WAL in transport measurements is a hallmark of quantum coherence of the charge carriers in a material in the presence of spin-orbit coupling as we described previously. The measured data can also be used to quantitatively assess the spatial extent of this electronic coherence.

In Figure 4.11 we show the evolution of the WAL cusp with increasing temperature, which broadens and weakens as the temperature is increased due to increased inelastic scattering of charge carriers at higher temperatures. WAL is a characteristic fingerprint of spin-orbit coupling in 2DESs, therefore these results demonstrate that the charge carriers in epitaxial $CsSnI_3$ experience significant spin-orbit coupling and open the door to the possibility of future spintronic or spin-orbitronic devices based on halide perovskites.

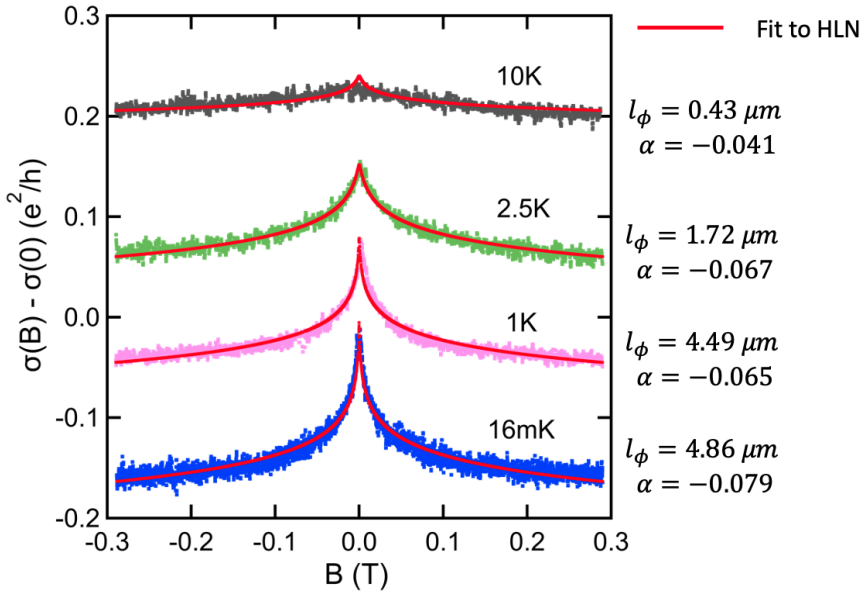

Figure 4.11: As the temperature is increased the WAL peak broadens and weakens as l_ϕ decreases due to increased inelastic scattering of charge carriers. The red solid line is a fit to the WAL theory (HLN formula, Equation 4.25) described in the text, from which we can extract α and the charge carrier coherence length l_ϕ at different temperatures, which are shown in the right hand side of each data trace.

4.6.3 Hikami-Larkin-Nagaoka Formula

To analyze the magnetoconductance data of epitaxial single-crystal $CsSnI_3$ thin films at low temperatures, we use the Hikami-Larkin-Nagaoka (HLN) formula [45, 8]. This formula describes 2D systems and quantitatively describes the relation between the change of the device's sheet conductivity with increasing magnetic field. It has the following form when one considers strong and weak SOC cases, and it is the so-called simplified empirical HLN formula: [45, 43]

$$\Delta\sigma = \sigma(B) - \sigma(0) = \frac{\alpha}{\pi}\left[\Psi\left(\frac{1}{2} + \frac{\hbar}{4eBl_\phi{}^2}\right) - \ln\left(\frac{\hbar}{4eBl_\phi{}^2}\right)\right]. \tag{4.25}$$

The conductance in Equation 4.25 is in quantized conductance units $\frac{e^2}{h}$, and the relation $l_\phi = \sqrt{D\tau_\phi}$ has been taken into account. The $\Psi(x)$ is the Digamma function. This equation contains two fit parameters l_ϕ and α, which can accurately capture the physics of WAL in our data without the need to know the diffusion coefficient of the device, since the two-terminal geometry of our device does not allow us to independently determine the charge carrier mobility. The sign of the coefficient α

T (K)	Average α	Average l_ϕ	T (K)	Average α	Average l_ϕ
0.016	-0.0780	4.90	2.65	-0.0693	1.38
0.1	-0.0788	4.91	3	-0.0638	1.59
0.2	-0.0761	5.03	4	-0.0578	1.27
0.3	-0.0685	5.44	5	-0.0478	1.05
0.4	-0.0679	5.09	7	-0.0500	0.63
0.5	-0.0696	4.67	8	-0.0403	0.65
0.7	-0.0682	4.73	10	-0.0394	0.48
0.85	-0.0697	3.67	15	-0.0462	0.27
1	-0.0670	4.13	20	-0.0297	0.20
2.5	-0.0601	2.38			

Table 4.1: HLN parameters using Equation 4.25 of the magnetoconductivity data of epitaxial $CsSnI_3$ at different temperatures. Values of l_ϕ and α correspond to the average value obtained from multiple measurements at a given temperature.

indicates the type of localization. Specifically, $\alpha > 0$ is associated with WL ($\alpha = 1$ is the weak spin-orbit interaction limit), while $\alpha < 0$ indicates WAL ($\alpha = -\frac{1}{2}$ is the strong spin-orbit interaction limit).

4.6.4 Data Fitting and Long Phase Coherence Length in $CsSnI_3$

In this subsection, we will show the fitting results (different α and l_ϕ values) of the magnetoconductance data obtained from our eptiaxial single-crystal $CsSnI_3$ thin film device measurements at different temperatures. The fitting formula we used is the simplified HLN formula (Equation 4.25) described in previous subsection.

To fit the magnetoconductivity data, such as the four data traces shown in Figure 4.11, we need to carefully choose the appropriate fitting range of the magnetic field B. The HLN formula is valid so long as the elastic mean free path l is smaller than the magnetic length $l_B = \sqrt{\frac{\hbar}{eB}}$ [27, 71, 25]. This condition leads to a significantly larger field range over which WAL is manifest in our measurements and accurately captured by the HLN formulation. While we do not know the precise value of l, it is reasonable to assume that it can be no larger than the $CsSnI_3$ thin film thickness (i.e. 50 nm). If we use 50 nm as an upper bound for the l, this will imply that the HLN formula would be valid below ± 0.3 T, which is the magnetic field range we use to fit the data. Also, the observed

correction (i.e. curvature) to the magnetoconductivity is an average effect over different electron loop trajectories in the $CsSnI_3$ device. The interference of different loop trajectories that have small enclosed area will only be destroyed at larger field. In our measurement, we qualitatively observe a WAL correction in a field range up to ± 0.3 T (see inset of Figure 4.10), which is the same field range as our previous estimation based in condition $l \ll l_B$. Moreover, there are copious examples in the literature showing fits to WL or WAL over quantitatively similar (or much larger) ranges in magnetic field, a non-exhaustive list includes [78, 133, 69]. In Figure 4.12, we can observe a relative small decrease of l_ϕ (less than a factor of 2) while we shrink the fitting range by an order of magnitude.

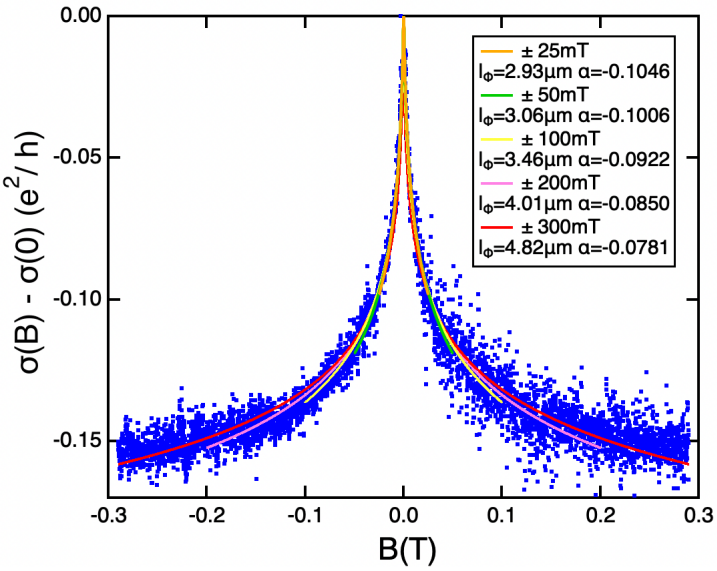

Figure 4.12: HLN fits (Equation 4.25) to the magnetoconductivity data of epitaxial $CsSnI_3$ at 17 mK. at different magnetic field ranges. Orange, green, yellow, pink and red curve are fits in which the fitting range are ±25 mT, ±50 mT, ±100 mT, ±200 mT and ±300 mT respectively. This analysis shows that the value of l_ϕ decreases only modestly as we shrink the fitting range.

The temperature dependence of the phase coherence length l_ϕ extracted from our measurements is shown in Figure 4.13 along with value of l_ϕ for other low-dimensional quantum electronic materials in the quantum diffusive transport regime. For our data on epitaxial $CsSnI_3$ each value of l_ϕ corresponds to the average value obtained from multiple measurements at each temperature and the error bars are the standard deviation. The value of the charge carrier phase coherence length

we find in epitaxial $CsSnI_3$ can be compared to other high-quality low-dimensional electronic materials in the quantum diffusive regime where localization measurements are possible such as Si [6], GaAs [6], GaAs microstrips [82], Graphene (blue cross) [56], Graphene (pink star) [4], Epi-graphene [27], Graphene flakes [121], and La-doped CdO [133]. We note that longer phase coherence exists in extremely high-mobility GaAs 2DESs and graphene but are not reported due to the absence of localization effects in sufficiently disorder free samples. In fact, in graphene ballistic transport has been observed over longer than 15 μm [128]. For completeness, the different values of α we obtained from HLN fitting at different temperatures are presented in Table 4.1. For the entire range over which we observe phase coherent transport (T<15 K) we find a negative value of α (see Table 4.1), which demonstrates the presence of spin-orbit coupling in the epitaxial $CsSnI_3$ film.

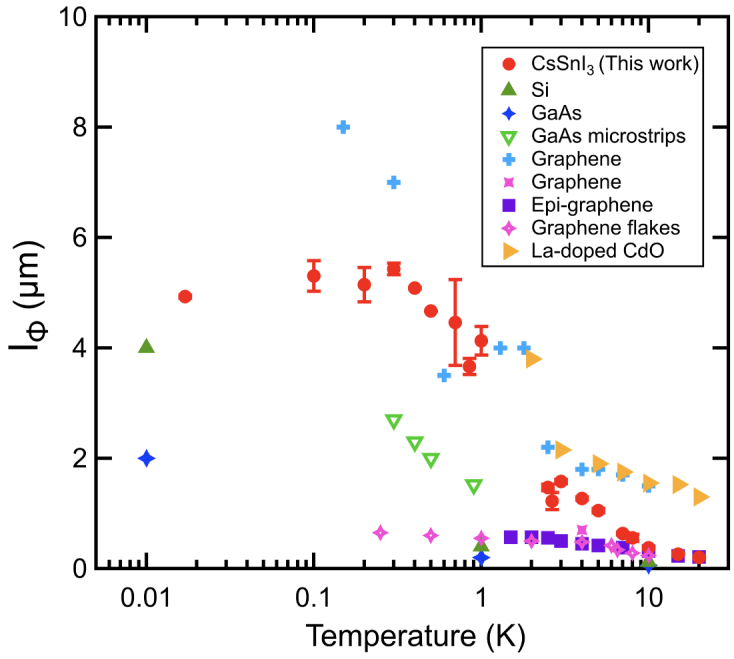

Figure 4.13: Temperature dependence of the charge carrier phase coherence length l_ϕ in the epitaxial $CsSnI_3$ thin film. Each value of l_ϕ corresponds to the average value obtained from multiple measurements at a given temperature and the error bars are the standard deviation. For comparison, we also show results from the literature for other electronic materials, which are Si [6], GaAs [6], GaAs microstrips [82], Graphene (blue cross) [56], Graphene (pink star) [4], Epi-graphene [27], Graphene flakes [121], La-doped CdO [133].

4.6.5 Reliability of Measurement and Data Fitting Results

There are several points which must be addressed to ensure that the fits produce reliable measures of l_ϕ and α. Since the measurement electrodes are at the center of the $CsSnI_3$ film and not along the edge of the film, it is somewhat difficult to determine the pattern of the current flow from one electrode to another, which would affect the measurement of the absolute conductivity. Additionally, the measurements were performed using a two-terminal configuration rather than a four-terminal configuration, so one must consider the role of the contact resistance in data fitting. Furthermore, the relation between l_ϕ and α should be discussed. In this subsection, we will answer these questions by giving more details and examples about the HLN fitting procedure of the magnetoconductivity data for the epitaxial $CsSnI_3$ thin film device.

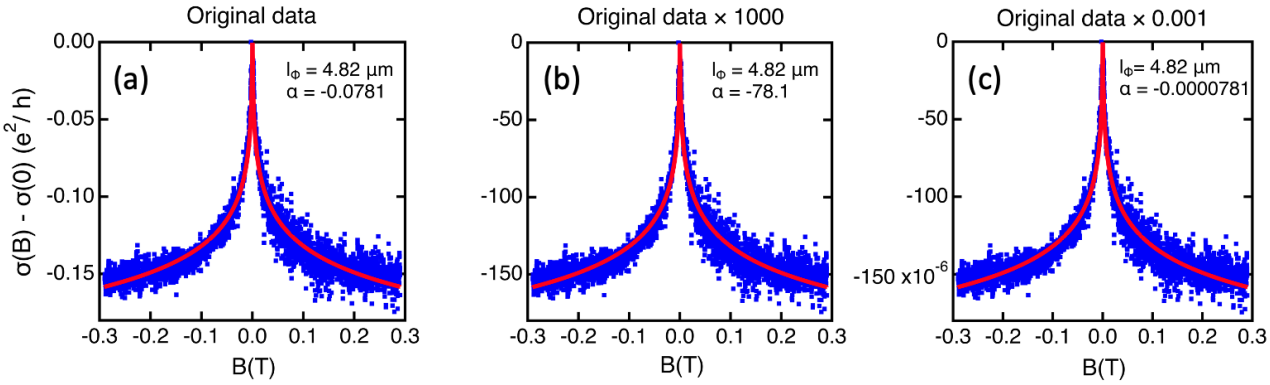

Figure 4.14: HLN fits (Equation 4.25) to the magnetoconductivity data of epitaxial $CsSnI_3$ at 17 mK. The red solid lines are fits to HLN. (a) Original magnetoconductivity data. (b) Scaled magnetoconductivity data by a factor of 1000. (c) Divided magnetoconductivity data by a factor of 1000. This change of scaling (i.e. the magnitude of the conductivity) is completely captured by a scaling of α and in each case l_ϕ is unchanged

(I) The absolute conductivity:

Despite the fact that the two-terminal conductivity measured is not the absolute conductivity of the epitaxial $CsSnI_3$ device, we can still determine the phase coherence length accurately by doing HLN fitting. This is because the phase coherence length is determined by the width and curvature (i.e. the shape) of the WAL cusp as a function of magnetic field and not the overall scaling (i.e. not the absolute magnitude of the conductivity). The scaling factor that normalizes our measurement

to the absolute conductivity is the multiplicative prefactor α, which is determined from the fit. This can be seen from Equation 4.25, where α cannot be subsumed into both the digamma and log functions to simply rescale l_ϕ. To make it more clear, we have shown the magnetotransport data scaled and divided by a factor of 1000 and then refit in Figure 4.14. In each case there is a corresponding change in α by the same scaling factor but l_ϕ remains unchanged. In other words, α serves as a simple scaling factor that takes into account the fact that the measurement does not capture the absolute conductivity, but this has negligible bearing on the value of l_ϕ.

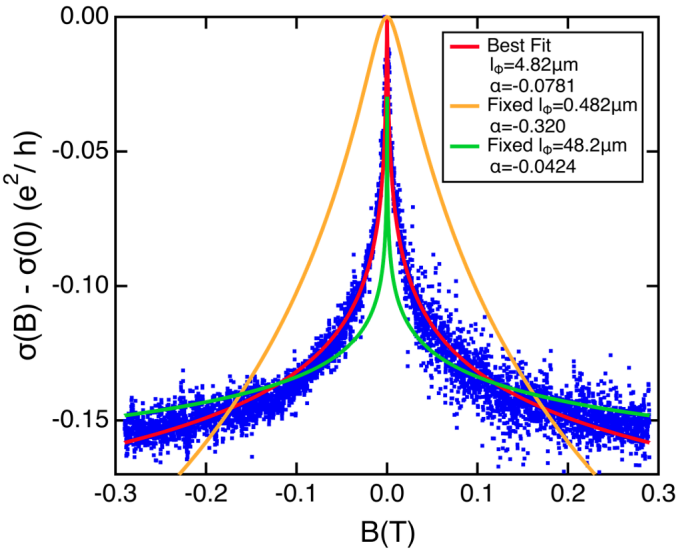

Figure 4.15: HLN fits (Equation 4.25) to magnetoconductivity data of epitaxial $CsSnI_3$ at 17 mK. The red line shows the best fit in which both α and l_ϕ are free fitting parameters. The orange and curve are fits in which we fixed $l_\phi = 0.482$ μm and $l_\phi = 48.2$ μm while allowing α to remain a free fitting parameter. This analysis shows that a value of l_ϕ either above or below several microns does not accurately describe the data.

(II) The dependence between l_ϕ and α:

Fitting parameters α and l_ϕ show strong dependence in the data fitting if we use our original data without scaling and dividing. Both α and l_ϕ are critical for getting the best fitting result because we will not get a good fitting if we fix one of parameters to a non-optimal value. For example, in Figure 4.15 we can see a significantly different value of l_ϕ does not accurately describe our data. In this figure we show three fits to our data at $T = 17$ mK. The best fit to the data is shown as the red

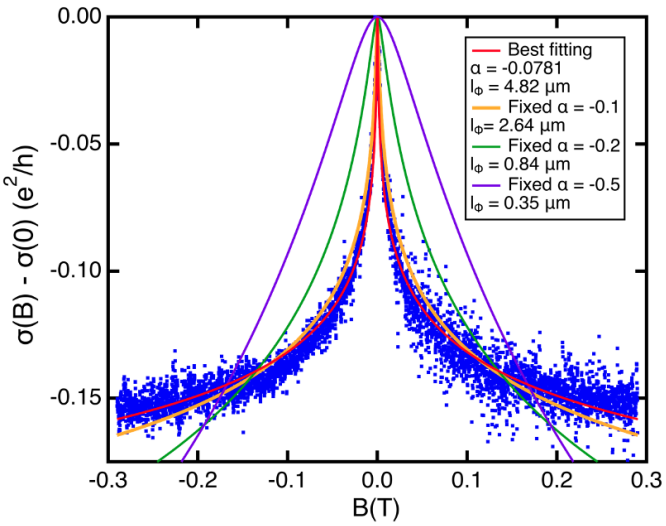

Figure 4.16: HLN fits (Equation 4.25) to magnetoconductivity data of epitaxial $CsSnI_3$ at 17 mK. The red line shows the best fit in which both α and l_ϕ are free fitting parameters. The orange, green and purple curve are fits in which we fixed $\alpha = -0.1, -0.2$ and -0.5 respectively while allowing l_ϕ to remain a free fitting parameter. This analysis shows that a value of α other than $\alpha = -0.0781$ does not accurately describe the data.

curve. For the other two fits we have fixed l_ϕ and allowed α to be a free parameter. In particular, for $l_\phi = 0.482\ \mu$m (orange) and $l_\phi = 48.2\ \mu$m (green), there is no value of α that will give a reasonable representation of the data. This fact can also be seen from the fittings in Figure 4.16, where we fixed the α and allowed l_ϕ to be a free parameter.

(III) Contact resistance R_c:

The total measured resistance of our device is given by $R_t = R_c + R_s$, where R_s is the intrinsic sample resistance and R_c is the total contact resistance from the two gold contacts. At low temperatures, from Figure 4.9, the total resistance of the device is approximately 20 Ω. This places an upper bound of $R_c \leq 20\,\Omega$ on the contact resistance between the gold pads and the $CsSnI_3$ layer. The HLN fitting does not take into account the contact resistance. However, as we shall show this only affects the value of α and has negligible effect on l_ϕ.

Since the resistance of the epitaxial $CsSnI_3$ device is small at low temperatures and we have connected two 10 kΩ resistors and a 1 MΩ resistor inline with the sample (see Figure 3.9 (a) and

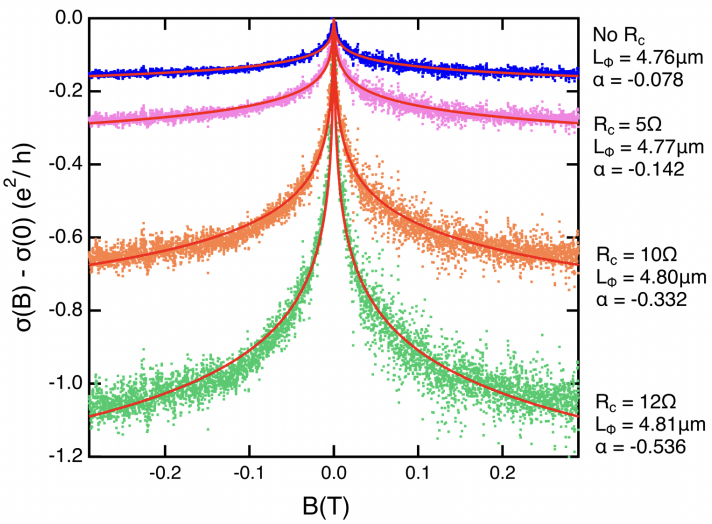

Figure 4.17: HLN fits (Equation 4.25) to magnetoconductivity data of epitaxial $CsSnI_3$ at 17 mK. The red solid lines are fit to HLN. The blue data are the original data without considering contact resistance. The pink, orange and green data are data assuming the overall contact resistance R_c to be 5 Ω, 10 Ω and 12 Ω respectively. The analysis shows if we assume the charge carriers in epitaxial $CsSnI_3$ are in strong SOC regime, the contact resistance should be 11.75 Ω.

(c)), the current I flow from one gold contact to another can be treated as a constant independent of B. Therefore the total measured resistance at a particular value of magnetic field will be:

$$R_t(B) = \frac{V_m(B)}{I} = R_c + R_s(B), \tag{4.26}$$

where V_m is the measured voltage across the two gold pads. From the above equation, we can derive the intrinsic voltage V_s developed across the sample, which is:

$$V_s(B) = I[R_t(B) - R_c]\,. \tag{4.27}$$

The intrinsic sample conductivity σ_s will be the following:

$$\sigma_s(B) = \frac{K_g}{R_t(B) - R_c}\,, \tag{4.28}$$

where K_g is the geometric factor between the two gold pads. If there is no contact resistance (i.e. $R_c = 0$), the change of the device conductivity as we apply magnetic field will be:

$$\sigma_{s,R_c=0}(B) - \sigma_{s,R_c=0}(0) = K_g \frac{R_t(0) - R_t(B)}{R_t(B)R_t(0)}\,, \tag{4.29}$$

where $R_t(0)$ is the intrinsic device resistance without applied magnetic field. If there is a contact resistance (i.e. $0 < R_c < R_t$), the change of the device conductivity will be:

$$\sigma_{s,R_c>0}(B) - \sigma_{s,R_c>0}(0) = K_g \frac{R_t(0) - R_t(B)}{[R_t(B) - R_c][R_t(0) - R_c]}. \tag{4.30}$$

Since the magnetoresistance only varies by 0.5% in the field range between $B = \pm 0.3$ T (see Figure 4.10 (b)), we can assume $R_t(B) \approx R_t(0) \equiv X$, and obtain the following ratio:

$$\frac{\sigma_{s,R_c>0}(B) - \sigma_{s,R_c>0}(0)}{\sigma_{s,R_c=0}(B) - \sigma_{s,R_c=0}(0)} = \frac{R_t(B)R_t(0)}{[R_t(B) - R_c][R_t(0) - R_c]} = \left(\frac{X}{X - R_c}\right)^2. \tag{4.31}$$

When R_c is much smaller than X, we can treat $\left(\frac{X}{X-R_c}\right)^2$ as a constant. That means introducing R_c into the HLN fitting procedure is equivalent to scaling the original data by a factor of $\left(\frac{X}{X-R_c}\right)^2$. From Figure 4.14, we have already shown that fitting the scaled data will only change α but not l_ϕ. Here we will give another example to show that the fitted l_ϕ will not change if we take R_c into account. In Figure 4.17, we present HLN fittings of different data traces, and each trace corresponds to a certain assumed value of R_c. The fitting results show that the different value of R_c will not dramatically change the value obtained for l_ϕ, and will only increase the value obtained for α (scale factor) as we increase R_c.

Moreover, since our data shows no sign of the crossover between WL and WAL in the low magnetic field regime (see Figure 4.10 (b) and Figure 4.11), we assume that the charge carriers in epitaixal $CsSnI_3$ thin film are in the strong SOC regime (in Equation 4.25, $\alpha = -\frac{1}{2}$ indicates the strong SOC limit). From HLN fitting with different values of assumed R_c, we find that $R_c = 11.75\,\Omega$ is the contact resistance if our device is in strong SOC limit ($\alpha = -\frac{1}{2}$).

4.6.6 Possible Origins of Spin-Orbit Coupling in $CsSnI_3$

From the previous discussion in Section 4.5, the magnitude of spin-orbit coupling in a material is dictated by whether the crystal lacks inversion symmetry. The origin of the inversion asymmetry can lead to different types of SOC. Inversion symmetry is broken if a compound is intrinsically non-centrosymmetric and results in Dresselhaus SOC [22]. It is not known whether the epitaxial

phase of $CsSnI_3$ intrinsically lacks an inversion center as it is nearly impossible to perform precise atomic refinement on an epitaxial thin film. Regardless, the presence of the interface between the KCl substrate and the $CsSnI_3$ epitaxial film breaks inversion symmetry and could lead to a Rashba spin-orbit field [11] along the growth direction of the heterostructure. In fact, it has been shown that the large Rashba splitting observed in tetragonal $MAPbI_3$ is likely not a bulk but rather a surface-induced phenomenon [33].

Alternatively, it is possible that the spin-orbit coupling in $CsSnI_3$ that we observe arises from the relatively large mass of the constituent atoms in the crystal (Atomic mass, Cs: 132.9, Sn: 118.7, I: 126.9). The larger mass atoms produce larger magnetic fields relativistically and thus the orbiting electrons gain larger spin-orbit splitting energy [44], which could be the origin of the strong SOC we infer from our measurement.

4.6.7 Possible Dephasing Mechanisms in Epitaxial $CsSnI_3$ Thin Film

There are three possible scattering processes which can cause dephasing of conducting electrons (or charge carriers). They are electron-electron (e-e) scattering, electron-phonon (e-ph) scattering, and spin-flip interactions.

Electron-electron scattering:

Electron-electron scattering is an energy transfer process which is strongly influenced by the temperature of the system. It arises from the fluctuating electromagnetic field created by other surrounding electrons in the system. The thermal energy $k_B T$ can cause thermal fluctuations which can change the electron's density and create electric field (Johnson noise). Due to the statistical nature of these fluctuations, such a scattering is different for each electron, thus the electronic ensemble loses it coherence [77].

Electron-phonon scattering:

Electron-phonon scattering is a energy transfer process between the electrons and crystal lattice since the vibrations of the positive ions in the crystal lattice can scatter the negatively charged electrons. The phonons (excited lattice vibration modes, which can be treated as a quasi-particle)

can be adsorbed or radiated by electrons in this scattering process. The strength of the scattering process is also highly related with the temperature of the system. As the temperature is lowered, the vibration amplitude of the ions become smaller, so the number of available phonons to absorb and emit will decrease. The decreased phonon numbers can lead to an increase of the electron's phase coherence time τ_ϕ.

Spin-flip interaction:

Additionally random spin-flip scattering is phase-breaking. Spin-flip interactions happen when the system has magnetic impurities. The magnetic moments of these impurities creates a local magnetic field that interacts with the conduction electron's spin. The interaction can cause a spin-flip of the electron and hence dephasing. The concentration of magnetic impurity in a material dictates the intensity of the spin-flip interaction [77].

Each individual effect listed above has a characteristic rate, they are τ_{e-e}^{-1} for electron-electron scattering, τ_{e-ph}^{-1} for electron-phonon scattering and τ_{s-f}^{-1} for spin-flip interaction. The phase coherence time τ_ϕ can be determined for these characteristic rates via Matthiessen's Rule:

$$\frac{1}{\tau_\phi} = \frac{1}{\tau_{e-e}} + \frac{1}{\tau_{e-ph}} + \frac{1}{\tau_{s-f}}\,. \tag{4.32}$$

In Figure 4.13, as the temperature is increased we observe a reduction in l_ϕ due to increased inelastic scattering of charge carriers in the epitaxial $CsSnI_3$ thin film. Despite the fact that we do not purposefully introduce magnetic defects/impurities (e.g. Fe, Mn, etc.), magnetic scattering is not impossible in our devices, despite it is somewhat unlikely. The purity of the source materials is high (CsI 99.9% (Sigma-Aldrich), SnI_2 99+% (Alfa Aesar), SnI_2 99% (Strem)), though it is possible for a small residual amount of magnetic impurities to be incorporated during growth from the source materials. Additionally, we cannot completely rule out the role of spin-flip interaction in dephasing since it has recently been demonstrated that vacancy-induced magnetism can arise in solution processed lead halide perovskite [119].

In the quantum diffusive regime, the temperature dependence of τ_ϕ also carries information regarding which of the scattering mechanisms dominates; however multiple competing mechanisms (as described above) often lead to mixed temperature dependences that are difficult to completely

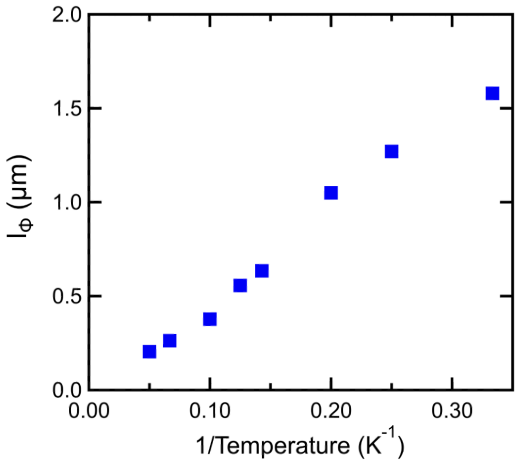

Figure 4.18: Charge carriers phase coherence l_ϕ as a functon of inverse temperature. The phase coherence length l_ϕ and $\frac{1}{T}$ are approximately in linear relationship. Note that $l_\phi = \sqrt{D\tau_\phi}$, which produces $\tau_\phi \propto \frac{1}{T^2}$.

disentangle [77]. We find that τ_ϕ scales as $\frac{1}{T^p}$ with $p \approx 2$ (see Figure 4.18), which is consistent with phonon scattering as the dominant contributor to dephasing with increasing temperature. In fact, previous studies on semiconductors and metals have reported electron-phonon scattering as leading to $p \approx 2-4$ [77]. Regardless of the underlying inelastic scattering mechanism, l_ϕ increases with decreasing temperature and reaches 5 μm below roughly 350 mK, below which it saturates, possibly due to thermal decoupling of the charge carriers at low temperatures.

CHAPTER 5

COHERENT HOPPING TRANSPORT AND GIANT NEGATIVE MAGNETORESISTANCE IN $CsSnBr_3$

5.1 Introduction

In the previous chapter, we have reported on the observation of phase coherent transport of charge carriers in the presence of spin-orbit coupling manifesting in weak anti-localization (WAL) in epitaxial $CsSnI_3$ thin films [94]. Phase coherent quantum interference effects in the form of weak localization have also been recently reported in quasi-epitaxial $CsPbBr_3$ [131]. Additionally, hybrid organic-inorganic halide perovskites of single-crystal $MAPbI_3$ and $MAPbBr_3$ have been shown to exhibit a variety of low-temperature and high-magnetic field transport phenomena under illumination [55]. In this chapter we will show that coherent transport effects can be realized in another high-quality halide perovskite epitaxial material, namely epitaxial single-crystal $CsSnBr_3$ thin films, at low-temperature and high magnetic field. Our $CsSnBr_3$ devices show 2D Mott variable range hopping (VRH) and giant negative magnetoresistance at low temperatures. As we will describe below, the giant negative magnetoresistance can be explained by the Nguyen-Spivak-Shkovskii (NSS) model for quantum interference between different directed hopping paths. Using this model, we can extract the temperature-dependent hopping length of charge carriers in this material, their localization length, and a lower bound for their phase coherence length, which we find to be $\cong$100 nm at low temperatures. These observations add to a growing body of evidence that demonstrates that epitaxial halide perovskite devices are emerging as a material class for low-dimensional quantum coherent transport devices. Much of this chapter will cover the results presented in [135]. Since we observe quantum coherent transport and hopping effects in our epitaxial halide perovskite ($CsSnI_3$ and $CsSnBr_3$) thin film devices, a brief discussion about the potential future prospect of the epitaxial single-crystal halide perovskite films will be given at the very end of this chapter.

5.2 Hopping Conduction in Disordered Systems

In Chapter 4, we described the quantum coherent transport physics, more specifically WL (WAL), of a system in the quantum diffusive transport regime with high charge carrier density. For systems with a low charge carrier density quantum effects can also manifest. In this section, we will describe low carrier density systems exhibiting hopping transport. This section will help us to understand the quantum coherent transport discussed in the next section.

5.2.1 Miller-Abrahams Conductivity

In this section we will introduce Miller-Abrahams conductivity as it serves as a key to understand nearest-neighbor hopping (NNH) and Mott variable range hopping (VRH), which we observed in $CsSnBr_3$ devices. We will first evaluate the current through a pair of localized electron states. If we assume no correlation between the occupation probability of different localized states, the steady-state current can be given by the following [105]:

$$I_{ij} = f_i(1 - f_j)\omega_{ij} - f_j(1 - f_i)\omega_{ji}, \tag{5.1}$$

where f_i and f_j are the occupation probabilities of a localized state i and j, and ω_{ij} is the electron or hole transition rate from occupied state i to empty state j. The occupation probability f_i is given by the Fermi-Dirac distribution function (see Equation 1.1):

$$f_i = \frac{1}{1 + \exp\left(\frac{E_i - \mu_i}{k_B T}\right)}, \tag{5.2}$$

where μ_i and E_i are the chemical potential (Fermi level) and energy of the state i, and T is the system temperature. The Miller-Abrahams hopping rate [88, 105] is related with the hopping process that originates from tunneling events and thermal activation, so we can write the transition rate from site i to site j where $E_j \geq E_i$ as:

$$\omega_{ij} \propto \exp\left(-\frac{2r_{ij}}{\xi} - \frac{E_j - E_i}{k_B T}\right), \tag{5.3}$$

where the $r_{ij} = |r_i - r_j|$ is the hopping length between site i and j, ξ is the Bohr radius of the localized states, which is also referred to as the localization length. If we then apply Equation 5.3 and 5.2 into Equation 5.1, we can get [105]:

$$I_{ij} \propto \exp\left(-\frac{2r_{ij}}{\xi}\right)\left[\frac{\sinh\left(\frac{\mu_j-\mu_i}{2k_BT}\right)}{\cosh\left(\frac{E_i-\mu_i}{2k_BT}\right)\cosh\left(\frac{E_j-\mu_j}{2k_BT}\right)\sinh\left(\frac{|E_i-E_j|}{2k_BT}\right)}\right]. \tag{5.4}$$

In the case of low electric field, resulting in a small voltage drop over a single hopping distance ($\Delta\mu = \mu_j - \mu_i \ll k_BT$), and $\mu \approx \mu_i \approx \mu_j$ (μ is the Fermi level of the system), the following conductivity is obtained [105]:

$$\sigma_{ij} \propto \frac{I_{ij}}{\Delta\mu} = \exp\left(-\frac{2r_{ij}}{\xi} - \frac{\Delta E}{k_BT}\right), \tag{5.5}$$

where the difference in energy ΔE is:

$$\Delta E = \frac{1}{2}(|E_i - \mu| + |E_j - \mu| + |E_i - E_j|)\,. \tag{5.6}$$

Equation 5.5 and 5.6 were derived by Miller and Abrahams in their calculation of the individual conductivity σ_{ij} in the resistor network, and it is often referred as the Miller-Abrahams conductivity [88, 29, 41]. More detailed derivations are provided by Abrahams and Miller's original paper [88].

5.2.2 Nearest-Neighbor Hopping

The Miller-Abrahams conductance can be applied to systems over a wide temperature range. When the system is at relatively high temperature, a charge carrier can be excited by a phonon and hop to an empty nearest-neighbor localized state via the shortest hopping path. The overall effect of a series of hoppings of this type by many charge carriers in the system creates the conduction, and it is refered as Nearest-Neighbor Hopping (NNH) conduction. We can derive NNH conduction from the Equation 5.5. The first exponential term $\exp\left(-\frac{2r_{ij}}{\xi}\right)$ of Equation 5.5 shows the tunneling rate between the two localized states. It depends on overlap between the exponential tails of the

wavefunctions of the sites but is not related to the temperature. The second exponential term $\exp\left(-\frac{\Delta E}{k_B T}\right)$ of Equation 5.5 describes the rate of activation over the barrier, based on the available thermal energy $k_B T$ and the relative depths of the potential wells at the localized sites [102]. At high temperatures where NNH dominates, we can treat the first exponential term $\exp\left(-\frac{2r_{ij}}{\xi}\right)$ as a constant since the hopping length r_{ij} will always be the shortest, which leads to the conductivity of NNH transport:

$$\sigma_{NNH}(T) = \sigma_0 \exp\left(-\frac{\Delta E}{k_B T}\right), \tag{5.7}$$

where σ_{NNH} is the conductivity of the NNH, σ_0 is a temperature independent pre-exponential factor and the difference in energy ΔE given in Equation 5.6.

5.2.3 Mott Variable Range Hopping

We will now introduce the physics of Mott Variable Range Hopping (VRH). The NNH in Subsection 5.2.2 occurs when the system is at relatively high temperature. However, if we cool down the system to very low temperatures, the NNH process is unlikely to happen, which can be seen from Equation 5.5. In this equation, at low temperatures, the contribution of the term $\exp\left(-\frac{\Delta E}{k_B T}\right)$ is greater than at high temperature. Thus, to achieve the maximum conductivity in a single hop at low temperatures, the charge carrier is more likely to hop a long distance (associated with a larger value of r_{ij}) to an empty state that has a small energy difference ΔE compared to its original state. This energetically favorable hopping process is the fundamental idea associated with Mott VRH. Figure 5.1 shows a schematic diagram of both NNH and VRH. When the system is at high temperature, the charge carrier can hop from a filled state to a nearest-neighbor empty state since thermal phonons provide the needed energy for the process. However, at lower temperatures, the phonon density is low and electrons are more likely to quantum mechanically tunnel to an empty state further away but closer in energy to the original state [112].

Now we will give a quantitative derivation of Mott's Law, which is the mathematical expression for the resistance of a disorder low carrier density system in the Mott VRH regime. This derivation is based on the treatment presented in the text by Efros and Shklovskii [113]. The hopping probability

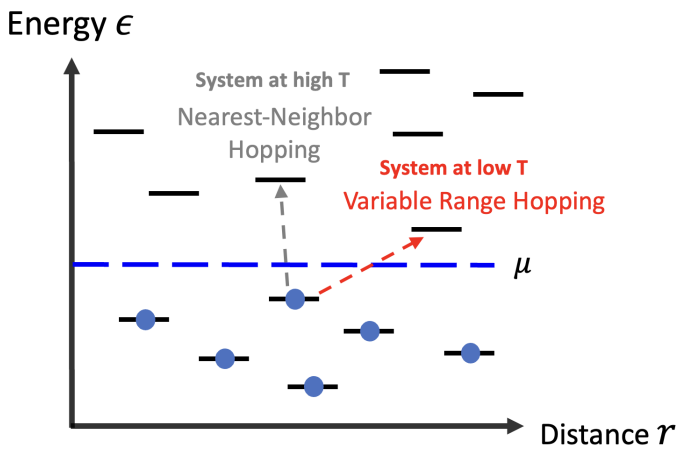

Figure 5.1: Schematic diagram showing the difference between NNH and VRH. Note that NNH happens when the system is at relatively high temperatures and VRH occurs only at low temperatures. In VRH, the charge carriers hop to distant empty localized sites that have a small energy difference relative to its initially occupied state. The blue dashed line shows the Fermi level μ [112].

presented in Equation 5.5 implies that the resistance R_{ij} associated with hopping from site i to j is given by:

$$R_{ij} = R_{ij}^{o} \exp\left(\frac{2r_{ij}}{\xi} + \frac{\Delta E}{k_B T}\right). \tag{5.8}$$

Consider a system with localized electronic states near the Fermi level. From the above expression, it is clear that at sufficiently low temperatures only hopping paths having very small values of ΔE will contribute to the conduction of the system (i.e. hopping is dominated by energetically favorable paths). From Equation 5.6, this means energies E_i and E_j should lie in a narrow band of energy near the Fermi level whose width decreases as T reaches absolute zero (see Figure 5.2). Since the system is at low temperature, the DOS in this narrow interval, which we will denote as $2\epsilon_0$, can be set as a constant (see the red solid line in Figure 5.2). This small energy interval $2\epsilon_0$ is important in Mott VRH and Efros-Shklovskii (E-S) VRH because charge carrier transport and hopping at low temperatures happens in this region near the Fermi level, and the system does not have thermal energy to excite from states that are far below the Fermi level. The localization length ξ in this case is independent of energy. Additionally, we will assume that

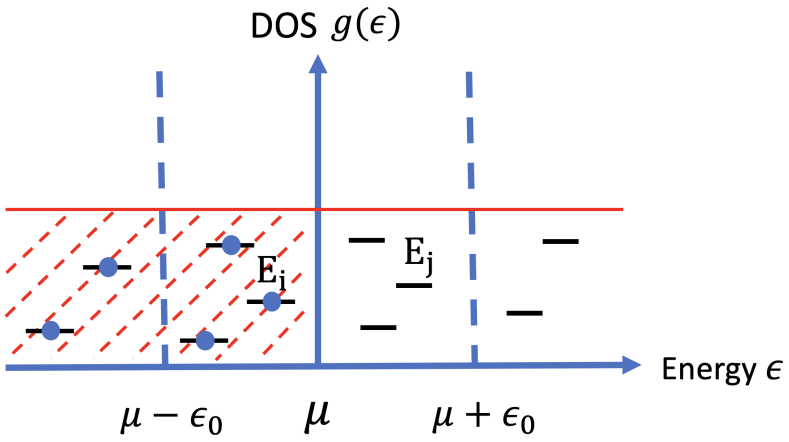

Figure 5.2: Density of states diagram of a narrow energy interval containing states whose energies are separated from the Fermi level by less than ϵ_0. The occupied states reside in the shaded region. The solid red line is DOS which is set to be constant in this model.

on average $\Delta E = \epsilon_0$ [113]. The number of localized states per unit volume N in this narrow energy interval $2\epsilon_0$ is:

$$N = 2g(\mu)\epsilon_0\,, \tag{5.9}$$

where we use $g(\mu)$ as the constant DOS in Figure 5.2. Then, the hopping length r_{ij} (in 3D) can be set as the average separation between two sites:

$$r_{ij} = \left(\frac{1}{N}\right)^{\frac{1}{3}} = \left(\frac{1}{2\epsilon_0 g(\mu)}\right)^{\frac{1}{3}}\,. \tag{5.10}$$

If we apply Equation 5.10 and the assumption $\Delta E = \epsilon_0$ to Equation 5.8, we arrive at:

$$R_{ij} = R_{ij}^{o} \exp\left\{\left[\frac{4}{g(\mu)\xi^3}\right]^{\frac{1}{3}} \epsilon_0{}^{-\frac{1}{3}} + \left(\frac{1}{k_B T}\right)\epsilon_0\right\}\,, \tag{5.11}$$

which describes the resistance associated with a hop from site i to j. Additionally, in the above equation, one can identify the competition between the overlap of the wavefunction (first term) and the activation energy (second term) in then hopping process, and changing the value of ϵ_0 (which is equivalent to changing r_{ij}, see Equation 5.10) has a different effect on each term. If we take the derivative of the terms inside the curly brackets in Equation 5.11 with respect to ϵ_0, and set this

derivative to be equal to zero, then we can find the minimum of the resistance R_{ij} at:

$$\epsilon_0 = \left[\frac{k_B^3 T^3}{\xi^3 g(\mu)} \right]^{\frac{1}{4}} . \tag{5.12}$$

If we apply Equation 5.12 to Equation 5.11 and 5.10, we arrive at the following results:

$$\rho(T) = \rho_0 \exp\left[\left(\frac{T_0}{T} \right)^{\frac{1}{4}} \right] \quad \text{and} \quad r(T) = \xi \left(\frac{T_0}{T} \right)^{\frac{1}{4}}, \quad \text{where: } T_0 = \frac{\beta_{3d}}{k_B g(\mu) \xi^3} . \tag{5.13}$$

Equation 5.13 represents **Mott's Law for VRH in 3D**. In these expressions, we have assumed that the overall temperature-dependent device resistivity $\rho(T)$ is proportional to the individual resistances R_{ij}. The temperature-dependent hopping length $r(T)$ represents the average of r_{ij} at a certain temperature T. The temperature T_0 is the characteristic temperature for 3D Mott VRH and β_{3d} is a numerical factor which can be derived using the Monte Carlo method and percolation theory. Its value is estimated to be $\beta_{3d} = 21.2$ [113, 117].

Mott's Law for VRH in 2D can be derived in a similar way, and here we present only the final result:

$$\rho(T) = \rho_0 \exp\left[\left(\frac{T_0}{T} \right)^{\frac{1}{3}} \right] \quad \text{and} \quad r(T) = \xi \left(\frac{T_0}{T} \right)^{\frac{1}{3}}, \quad \text{where: } T_0 = \frac{\beta_{2d}}{k_B g(\mu) \xi^2} . \tag{5.14}$$

The temperature T_0 is the characteristic temperature for 2D Mott VRH, and $\beta_{2d} = 13.8$ [113, 117].

It is important to note that the above discussion about Mott VRH is restricted to the linear response regime. In general the low temperature current-voltage (I-V) relationship will be highly non-linear, and the conduction will not be thermally activated but rather dominated only by the driving strength of the applied electric field. In this regime, we can derive the electric field dependent hopping resistivity $\rho(F)$, where F is the electric field [57, 108, 92]. A simple way to obtain $\rho(F)$ is the following manner. First, we set the narrow energy interval $\epsilon_0 = eFr_{ij}$ (on average) since ϵ_0 cannot be smaller than the work done by an electron's hop. Then using Equation 5.10, we can obtain r_{ij} in the 3D case:

$$r_{ij} = \left(\frac{1}{2g(\mu)eF} \right)^{\frac{1}{4}} . \tag{5.15}$$

If we ignore numerical factors and apply Equation 5.15 to Equation 5.8 and ignore the term associated with thermally activated transport, we arrive at a set of equations describing the low-temperature, non-linear field driven transport:

$$\rho(F) = \rho_0 \exp\left[\left(\frac{F_0}{F}\right)^{\frac{1}{d+1}}\right] \text{ and } r(F) = \xi\left(\frac{F_0}{F}\right)^{\frac{1}{d+1}}, \text{ where: } F_0 = \frac{\beta_F}{eg(\mu)\xi^{(d+1)}}, \tag{5.16}$$

where $d = 2$ for 2D and $d = 3$ for 3D, and β_F is a numerical factor which is different for 2D and 3D.

5.2.4 The Coulomb Gap and Efros-Shklovskii Variable Range Hopping

In the derivation of Mott VRH in Subsection 5.2.3, we made the assumption that the DOS $g(\epsilon)$ is a constant within the narrow energy interval, and that electron-electron interactions could be ignored. However, this statement is not always true in the general case. According to computer simulation results from Efros and Shklovskii [113], the shape of DOS in a doped semiconductor near Fermi level varies as the ratio of the concentration of acceptors (N_A) to the concentration of donors (N_D) varies, i.e. $K = \frac{N_A}{N_D}$, and by definition $0 \leq K \leq 1$. This simulation takes electron-electron interactions into account, and the result shows at both $K \ll 1$ and $1 - K \gg 1$, the DOS near the Fermi level become bell-shaped. The Fermi level in both cases is at one of the wings of the DOS distribution (see Figure 5.3 (a) and (b)) [34]. But when K is an intermediate number between 0 and 1, the location of the Fermi level is not near the maximum of the DOS distribution as one might expect. For example, if we set $K = 0.5$ the DOS is minimal at the Fermi level (see Figure 5.3 (c)) [113]. The gap in the DOS in Figure 5.3 (c) around the Fermi level is called the "Coulomb gap". This gap is generally caused by the Coulomb interaction between electrons and results in a diminished DOS at the Fermi surface. The result from Efros and Shklovskii [113] demonstrate that in general we cannot treat the DOS $g(\epsilon)$ as a constant as we did in the case of Mott VRH. Next, we will present a method to construct the DOS function of the Coulomb gap and describe Efros-Shklovskii (E-S) VRH.

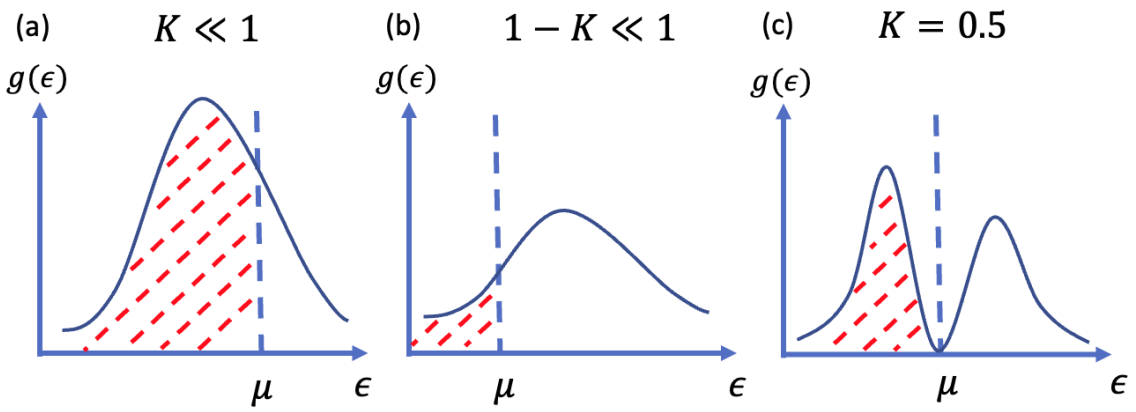

Figure 5.3: Schematic diagram of a more realistic DOS of a doped semiconductor according to computer simulations [113]. The simulation result shows DOS varies as the ratio $K = \frac{N_A}{N_D}$ varies. (a) $K \ll 1$, (b)$1 - K \gg 1$, (c) $K = 0.5$. The area shaded with red dashed lines shows occupied states. The blue dashed lines are Fermi levels.

We begin by considering that at sufficiently low temperatures, all electron states below the Fermi level μ are occupied while all the states above μ are empty. In a narrow energy interval $(\mu - \epsilon_0\,,\ \mu + \epsilon_0)$ around the Fermi level, the work associated with transferring an electron from occupied state E_i to empty state E_j can be written as [24]:

$$\Delta W_{i\to j} = E_j - E_i - \frac{e^2}{\kappa r_{ij}} > 0, \tag{5.17}$$

where r_{ij} is the hopping length between the two states and κ is the electrical permittivity of the material environment containing the electrons. This equation can be obtained in two steps. In the first step, we take an electron from a filled donor site i to infinity where the potential energy is taken to be zero. The amount of work done in this step is $-E_i$. In the second step, the amount of required work to move the electron to site j is E_j if the occupation of a donor corresponded to the ground state of the system. However, the donor site i is empty and should be treated as positive charge. Therefore, in the calculation, the attraction between the positive charged site i and the electron will diminish the required work by the amount of $-\frac{e^2}{\kappa r_{ij}}$ [113]. The total work $\Delta W_{i\to j}$ should be greater than zero otherwise the alternative configuration in which the state j is occupied and the state i is empty would be preferable. From Equation 5.17 and the condition $E_j - E_i < 2\epsilon_0$, we can derive

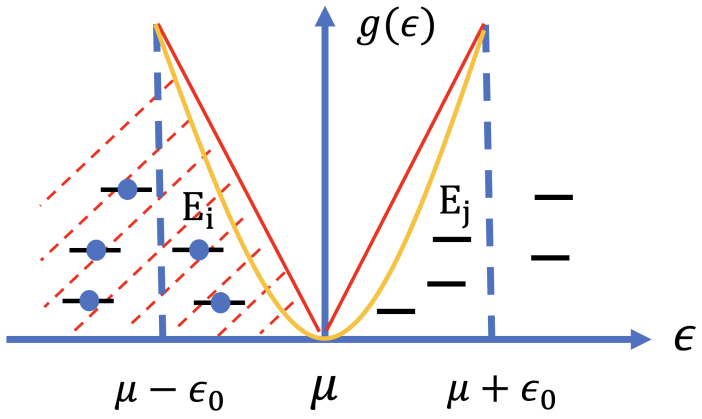

Figure 5.4: The Coulomb Gap in the DOS of a low carrier density material in 2D (linear red line) and in 3D (parabolic yellow curve). The red shaded area corresponds to occupied states.

the constraint for the total number of impurity states N in a d-dimensional (d=2 or 3) system:

$$N(\epsilon_0) = \frac{1}{r_{ij}^d} < \left(\frac{2\kappa\epsilon_0}{e^2}\right)^d . \tag{5.18}$$

Since ϵ_0 can be arbitrarily small, we can replace the inequality in Equation 5.18 with an equality [34]. The corresponding DOS function for this small interval of energy around Fermi level will be:

$$g(\epsilon_0) = \left|\frac{\partial N(\epsilon_0)}{\partial \epsilon_0}\right| \propto d\left(\frac{2\kappa}{e^2}\right)^d {\epsilon_0}^{d-1} . \tag{5.19}$$

Additionally, we can replace the small parameter ϵ_0 by $|\epsilon - \mu|$. In this case, the DOS function near the Fermi level becomes:

$$g(\epsilon) \propto d\left(\frac{2\kappa}{e^2}\right)^d |\epsilon - \mu|^{d-1}. \tag{5.20}$$

The DOS $g(\epsilon)$ that results from taking into account the Coulomb interaction is not a constant as in the case of Mott VRH. In a disordered 2D system with a low carrier concentration, $g(\epsilon)$ is linear in $|\epsilon - \mu|$, and in a disordered 3D system $g(\epsilon)$ is parabolic in $|\epsilon - \mu|$, as shown in Figure 5.4. From Equation 5.18 and the previous arguments, we find that the hopping length $r_{ij} = \frac{e^2}{2\kappa\epsilon_0}$. This hopping length can be inserted into Equation 5.8, where we can assume on average $\Delta E = \epsilon_0$, and obtain:

$$R_{ij} \propto \exp\left(\frac{e^2}{2\xi\epsilon_0\kappa} + \frac{\epsilon_0}{k_B T}\right) . \tag{5.21}$$

Equation 5.21 above shows that there is a minimal value of R_{ij} when:

$$\epsilon_0 = \left(\frac{e^2 k_B T}{2\xi\kappa} \right)^{\frac{1}{2}} . \tag{5.22}$$

Then, if we apply this value of ϵ_0 to Equation 5.21, we obtain the mathematical expressions for the E-S VRH model:

$$\rho(T) = \rho_0 \exp\left[\left(\frac{T_{ES}}{T} \right)^{\frac{1}{2}} \right] \quad \text{and} \quad r(T) = \xi \left(\frac{T_{ES}}{T} \right)^{\frac{1}{2}} , \quad \text{where: } T_{ES} = \frac{e^2 \beta_{ES}}{k_B \kappa \xi} . \tag{5.23}$$

The temperature-dependent resistivity $\rho(T)$ and hopping length $r(T)$ in the E-S VRH model are valid for both 2D and 3D, and β_{ES} is a numerical factor which was calculated (using the theory of percolation) to be 6.2 in 2D [99] and 2.8 in 3D [113].

5.2.5 Zabrodskii Method

In this section, we will describe a common method used to analyze the temperature dependence of the resistance of a device or system developed by Zabrodskii and Zinov'ewa [134], often referred as the "Zabrodskii method" (or the resistance curve derivative analysis (RCDA) method.) This method can help to determine the dominant transport mechanism of a system. As we shall see, the temperature-dependent resistivity $\rho(T)$ in most systems (such as in our $CsSnBr_3$ thin film devices) can take the following general phenomenological form:

$$\rho(T) = BT^{-a} \exp\left[\left(\frac{T_0}{T} \right)^{x} \right] , \tag{5.24}$$

where B, a, T_0 and x are all constants. The exponent x carriers information about which transport regime is dominant in a measured device. In the Zabrodskii method we define a quantity $\omega(T)$:

$$\omega(T) = -\frac{\partial \ln \rho}{\partial \ln T} . \tag{5.25}$$

By combining Equations 5.24 and 5.25, we get:

$$\omega(T) = a + x \left(\frac{T_0}{T} \right)^{x} , \tag{5.26}$$

When the system has an exponential (activated) $\rho(T)$ dependence, we have $\omega(T) = x\left(\frac{T_0}{T}\right)^x$, by taking the logarithm on both sides we have:

$$\ln(\omega) = \ln\left(xT_0^x\right) - x\ln(T). \tag{5.27}$$

The first term of the above equation is a constant, which means we can find the value of x by fitting a plot of $\ln(\omega)$ versus $\ln(T)$. We now provide a example to show how the Zabrodskii method works in practice based on measurement of GaGdN layers grown on semi-insulating 6H-SiC(0001) substrates [5]. By determing the value of x in different temperature ranges, one can determine the transition from E-S VRH to Mott VRH as the device's temperature is reduced.

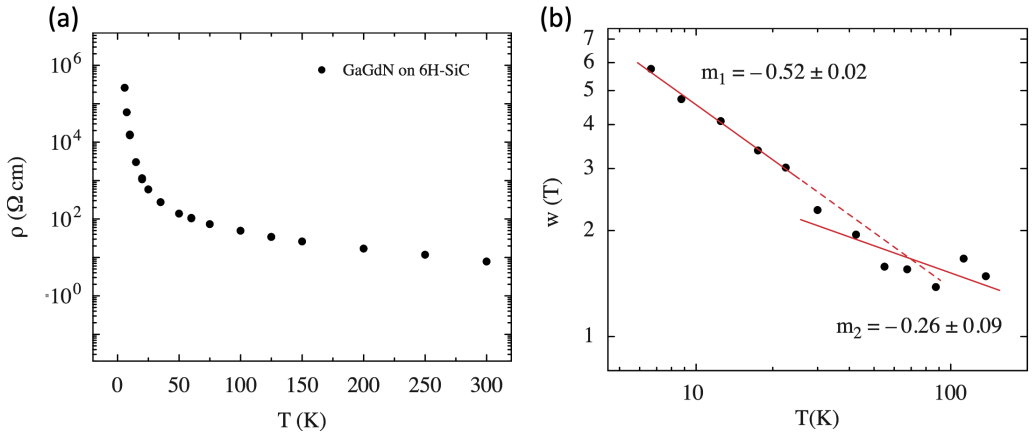

Figure 5.5: Application of the Zabrodskii method to transport measurements performed on GaGdN layers grown on semi-insulating 6H-SiC(0001) substrates by Bedoya-Pinto *et al*. [5]. (a) Temperature dependence of the resistivity of GaGdN on 6H-SiC. (b) Transition from E-S VRH to Mott VRH as determined by Zabrodskii method (m_1 and m_2 correspond to two different values of the exponent x shown in Equation 5.24). Note that data plotted on Figure (b) are on a logarithmic scale for both axes, which is equivalent to plotting $\ln(\omega)$ versus $\ln(T)$.

The successful analysis of the transport data using Zabrodskii method requires precise control and measurement of the device temperature, which is not possible over a wide range of temperature in our system. Thus, we are not able to apply Zabrodskii method in our data analysis.

5.3 Nguyen-Spivak-Shkovskii Model

In this section, we will discuss the role of quantum interference in 2D Mott VRH based on the so-called NSS theory developed by Nguyen Spivak and Shkovskii [97]. The contents of this section are based on the treatment in [114, 97, 50, 137]. The general idea of NSS theory is the following: Typically, each electron hop is accompanied by a phonon emission or absorption event and thus an electron loses phase information after each hop. However, as we will see below, interference can occur between different hopping (tunneling) trajectories connecting two fixed sites. Furthermore, this interference can be altered by the presence of a magnetic field which manifests as a giant negative magnetoresistance. This phenomena will be described below and we will see that it actually describes our data on epitaxial $CsSnBr_3$ thin films.

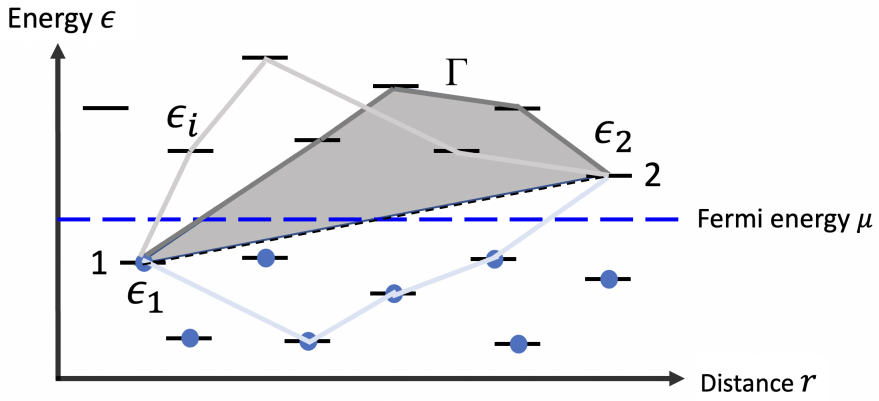

Figure 5.6: The diagram depicting the NSS model. Three (out of many possible) zigzag hopping paths are shown. All of these paths contribute to the probability amplitude of an electron hop from localized site 1 to 2 (having energy ϵ_1 and ϵ_2). The grey shaded area is the enclosed area S_Γ for the hopping path Γ. When an external magnetic field (normal to the plane of the 2D material) is applied, an additional phase term $\varphi_\Gamma = \frac{2\pi B S_\Gamma}{\Phi_0}$ will be introduced to the hopping path Γ, and the interference between different hopping paths leads to negative magnetoresistance. The short horizontal lines are localized states (impurities) where elastic scattering occurs during the electron's transit from 1 to 2.

From Equation 5.14, for 2D Mott VRH, the hopping length $r(T)$ is much greater than the average distance between nearest impurity sites (i.e. the localization length ξ). This provides the possibility for electrons to take multiple hopping paths between localized sites (see Figure 5.6). Along each

hopping path, there are many elastic scattering events that can affect the overall probability of electrons hopping from localized site 1 to 2. During these scattering events the electron maintains its phase coherence. Additionally, the phases of electrons on different hopping paths are different in general and can interfere. Electrons ultimately lose their phase information after arriving at site 2 once the hopping process is done.

If there is are impurities between site 1 and 2, the wavefunction describing an electron tunneling from site 1 to 2 takes the form [114]:

$$\psi_1^0(\vec{r}) \propto \frac{1}{|\vec{r}-\vec{r_1}|}\exp\left(-\frac{|\vec{r}-\vec{r_1}|}{\xi}\right). \tag{5.28}$$

Each impurity along a typical hopping path produces scattering, and scattering by impurity i (having energy ϵ_i, see Figure 5.6) results in a wavefunction of the form [76]:

$$\psi_{\text{scat}} = \psi_1^0(\vec{r_i})\frac{\mu_i}{4\pi|\vec{r}-\vec{r_i}|}\exp\left(-\frac{|\vec{r}-\vec{r_i}|}{\xi}\right) \quad \text{where:} \quad \mu_i \equiv \frac{8\pi\xi\epsilon_i}{\epsilon_1-\epsilon_i}, \tag{5.29}$$

where μ_i is the scattering amplitude associated with impurity i. Along the hopping path from site 1 to 2, the electron can be scattered elastically many times. All these waves contribute to the wave function $\psi_1(\vec{r_2})$ at site 2,

$$\begin{aligned}\psi_1(\vec{r_2}) = \psi_1^0(\vec{r_2}) &+ \sum_i \frac{\mu_i\psi_1^0(\vec{r_i})}{|\vec{r_2}-\vec{r_i}|}\exp\left(-\frac{|\vec{r_i}-\vec{r_2}|}{\xi}\right) \\ &+ \sum_{ij}\psi_1^0(\vec{r_i})\frac{\mu_i}{|\vec{r_j}-\vec{r_i}|}\exp\left(-\frac{|\vec{r_j}-\vec{r_i}|}{\xi}\right)\frac{\mu_i}{|\vec{r_j}-\vec{r_2}|} \\ &\times\exp\left(-\frac{|\vec{r_j}-\vec{r_2}|}{\xi}\right)+\ldots = \sum_{\{\Gamma\}}\psi_\Gamma(\vec{r_2}).\end{aligned} \tag{5.30}$$

The above expression includes all the contributions of possible hopping paths Γ connecting site 1 and 2. Since the scattering wavefunctions decay exponentially with increasing distance from an impurity and only forward scattering is relevant, the scattering paths are concentrated inside the cigar-shaped domain. An important aspect of Equation 5.30 is that all terms in this equation are real and can in general have either sign since the scattering amplitude μ_i can be positive or negative. It will be beneficial to recast the effect of scattering and interference on the transport in terms of a

new factor J:

$$\psi_1(\vec{r_2}) = J\psi_1^0(\vec{r_2}) \quad , \quad J \equiv \sum_{\{\Gamma\}} J_\Gamma \quad , \quad R_{12} = J^{-2} R_0 \exp\left(\frac{2r}{\xi}\right) . \tag{5.31}$$

The factor J represents the total amplitude of the tunneling wavefunction and it is the sum of amplitudes of the individual paths J_Γ. In the NSS model, J is a random real number that depends on ϵ_1, ϵ_2 and the hopping length r ($r \equiv r_{12}$), and it depends on the random coordinates and energies of all impurities that are located in the system. The resistance R_{12} is that between site 1 and 2 and it is associated with value of J and not with the temperature of the system [114] at sufficiently low temperatures. In the presence of a small magnetic field normal to the 2D system, the wavefunction between two scattering centers introduce a phase factor $\exp(i\varphi_\Gamma)$ to each path Γ and results in a complex J [114]:

$$J = \sum_{\{\Gamma\}} J_\Gamma \exp(i\varphi_\Gamma) \quad \text{where:} \quad \varphi_\Gamma = \frac{2\pi B S_\Gamma}{\Phi_0} . \tag{5.32}$$

In Equation 5.32, Φ_0 is the flux quantum and S_Γ is the area enclosed by a scattering path and a straight line connecting site 1 and 2 (see grey shaded area in Figure 5.6).

The next part of the question is how can transport in the 2D Mott VRH regime be understood in the context of the NSS model of coherent hopping. Methods developed from percolation theory can be used to answer this quesition [113, 114]. Percolation theory (which is beyond the scope of this dissertation) describes the behavior of a network when additional nodes or links are added [28]. In physics, it is often used to calculate the electrical conductivity of a system by building a resistor network model that reflects a material with certain lattice structure and impurity concentration (for more detail see [113, 114]). From percolation theory, the magnetoconductance is determined by a logarithmic average L over realizations of the impurity distribution [113, 137]:

$$L \equiv \ln\left[\frac{\sigma(B)}{\sigma(0)}\right] = \left\langle \ln\left[\frac{\sigma_{ij}(B)}{\sigma_{ij}(0)}\right]\right\rangle = \left\langle \ln\left[\left|\frac{J(B)}{J(0)}\right|^2\right]\right\rangle . \tag{5.33}$$

By building up a percolating network in the hopping transport regime with various concentration of impurities and distribution of scattering amplitude μ_i, and using Equation 5.33, the authors in [137] found the following formula for L, which as we shall see below, leads to negative magnetoresistance

[137, 87]:

$$L = \gamma \frac{r(T)}{l_B} . \tag{5.34}$$

Note that both side of this equation is unitless, $l_B = \left(\frac{\hbar}{eB}\right)^{\frac{1}{2}}$ is the magnetic length and γ is a universal numerical coefficient and it is estimated to be $\gamma \approx \frac{0.1}{\sqrt{2}}$ [137]. The quantum interference between multiple hopping paths between two localized states creates fluctuation in hopping probability, and a large negative magnetoresistance can be achieved by averaging these fluctuations over different hopping processes in the system [98]. If we consider Equation 5.33 and 5.34, and the magnetic length l_B, we obtain:

$$\ln\left[\frac{R(B)}{R(0)}\right] = -\gamma r(T) \left(\frac{e}{\hbar}\right)^{\frac{1}{2}} B^{\frac{1}{2}} . \tag{5.35}$$

Equation 5.35 clearly shows the dependence of the logarithm of normalized magnetoresistance $\ln\left[\frac{R(B)}{R(0)}\right]$ as a function of $B^{\frac{1}{2}}$. More details regarding this equation will be provided when we present the negative magnetoresistance data from our $CsSnBr_3$ thin films in Subsection 5.4.3.

NSS physics has been realized in various systems in the 2D VRH regime including GaAs field-effect transistors [65], fluorinated graphene [47], Ge films [90], In_2O_{3-x} films [89] and GaAs/AlGaAs heterostructures [52]. All of these systems show large negative magnetoresistance when the systems are at low temperatures, and Figure 5.7 shows an example from [52] on GaAs/AlGaAs heterostructures. The magnetoresistance of this sample shows the characteristic linear dependence versus $B^{\frac{1}{2}}$ predicted by Equation 5.35.

5.4 Coherent Hopping Transport in $CsSnBr_3$

5.4.1 Temperature-Dependent Electrical Properties of Epitaxial $CsSnBr_3$

Before presenting the result on hopping transport, in this subsection we will first discuss the temperature-dependent resistance observed in epitaxial $CsSnBr_3$ devices. Evidence for a structural phase transition observed in the temperature-dependent resistance data will also be discussed.

Figure 5.8 shows the resistance of $CsSnBr_3$ epitaxial thin film devices versus temperature as they are cooled from room temperature to 2.4 K in the absence of a magnetic field. In each of

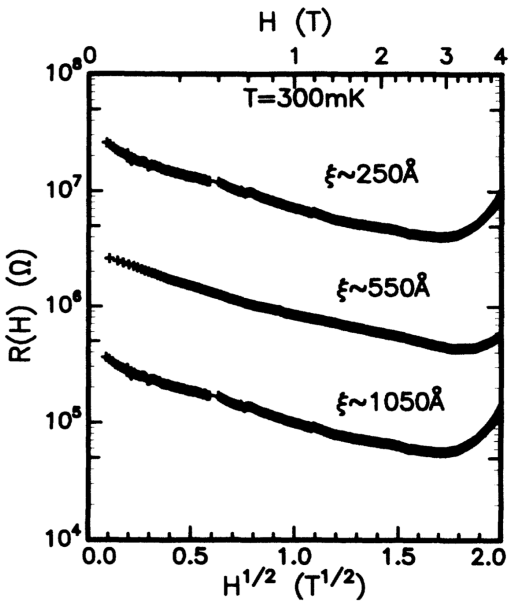

Figure 5.7: Data from [52], semilogarithmic plot of the magnetoresistance as a function of $H^{\frac{1}{2}}$ at a fixed temperature of T=300 mK for a low-dimensional electron systems in a molecular-beam-epitaxy grown GaAs/AlGaAs heterostructure at three different localization lengths (controlled a by gate voltage to tune the charge carrier density) of ξ = 250, 550, and 1050 Å.

the two devices, we observe that the resistance increases as the temperature decreases and reaches many tens of kΩ at the lowest temperatures. While previous work has reported Ohmic contact between $CsSnBr_3$ and gold at room temperature [127], our two-terminal resistance measurements cannot preclude a contribution from a contact resistance between the evaporated gold contacts and the $CsSnBr_3$ epilayer. Nevertheless, we emphasize that such a contact resistance would not change the conclusions we draw regarding coherent hopping transport. We also note that recent theoretical work has indicated the potential role of electrode induced impurities in $CsSnBr_3$ [75], which could be investigated with future four-terminal devices. Finally, we note that all measurements reported here were performed in a regime of linear response, which was ensured by performing device IV characteristics at the lowest temperatures.

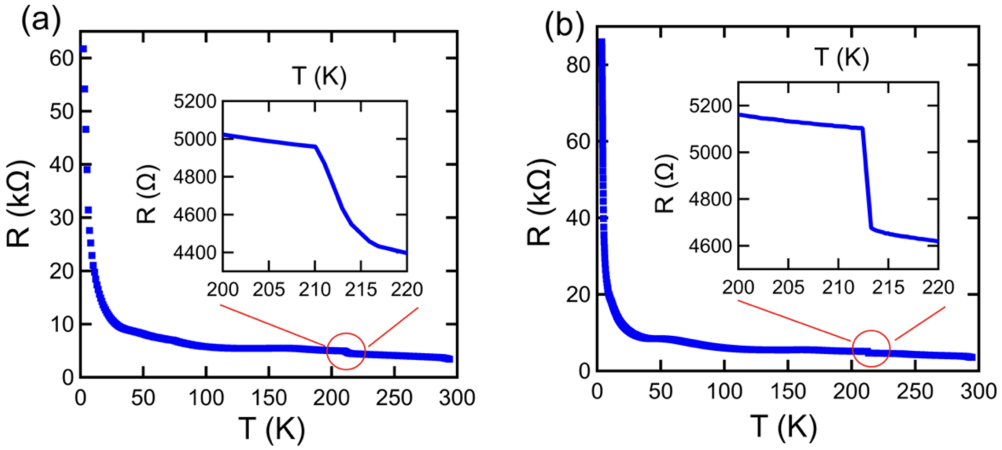

Figure 5.8: (a) Resistance versus temperature of $CsSnBr_3$ device. (b) Additional $CsSnBr_3$ device for comparison. Insets: Data zoomed in near 215 K, highlighting the observed kink in $R(T)$, which is indicative of a structural phase transition upon cooling.

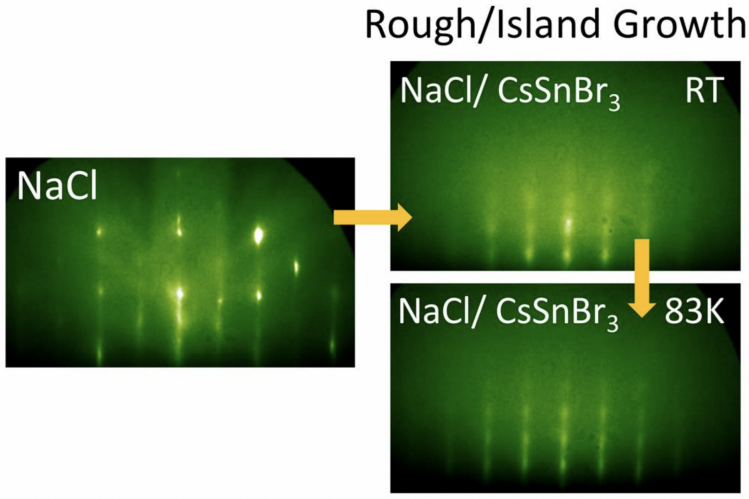

Figure 5.9: *In situ* RHEED data of rough $CsSnBr_3$ grown epitaxially on NaCl (left) and cooled from room temperature (top, right) to just above liquid nitrogen temperature (bottom, right).

In the resistance data, we observe a repeatable small kink that appears at 215 K in all of the samples we have measured (see insert of Figure 5.8 (a) and (b)). The kink is likely associated with a structural phase transition in the epilayer. In fact, structural phase transitions have been reported previously in bulk $CsSnBr_3$ [91]. Moreover, our *in situ* RHEED diffraction measurements on

rough $CsSnBr_3$ show an increase in the c/a lattice ratio of 7 ± 2% (based on the change in the spot spacing in the dz/dx directions) as the sample is cooled from room temperature to 83 K, confirming the presence of a cubic to tetragonal phase transition (see Figure 5.9).

5.4.2 2D Mott Variable Range Hopping in $CsSnBr_3$

In the previous section, we have showed that the $CsSnBr_3$ device we have is consistent with that of a lightly doped semiconductor (see Figure 5.8). Moreover, the data at low-temperature range (15 K to 125 mK, see Figure 5.10) is consistent with the 2D Mott VRH,

$$\ln[R(T)] = \ln(R_0) + \left(\frac{T_0}{T}\right)^{\frac{1}{3}} \tag{5.36}$$

The above equation (derived from Equation 5.14) gives a clear picture regarding the temperature dependence of the measured resistance in our devices and 2D Mott VRH. The characteristic temperature $T_0 = 32$ K and $T_0 = 44$ K for device A and B (A and B has same geometry which can be found in Subsection 3.4.2) are obtained from fits to $R(T)$. The fact that we observe 2D Mott VRH in epitaxial $CsSnBr_3$ thin film devices implies that the electrons in $CsSnBr_3$ undergo phonon-assisted tunneling between different localized states and that the tunneling distance of electron is much larger than the distance between impurities at low temperatures, as depicted in Figure 5.1.

As describe above, the regime of variable range hopping (VRH) will only appear at a sufficiently low temperature. As the temperature increases, thermally activated NNH will onset and dominate the hopping transport between localized sites. NNH here is characterized by a dependence $\ln[R(T)] \propto \frac{1}{T}$, as shown by Equation 5.7. In Figure 5.11 (a) and (c) we present measurements of the resistance of two devices at higher temperature (35 K to 15 K), showing this expected $\frac{1}{T}$ dependence for our epitaxial $CsSnBr_3$ devices. Additionally we observe a saturation of the device resistance roughly below 125 mK as shown in Figure 5.11 (b) and (d). This deviation is likely associated with a thermal decoupling of the device from the mixing chamber as the primary source of electronic heat exchange between the sample and the cryostat decreases with increasing device resistance leaving the device at an elevated temperature relative to the mixing chamber.

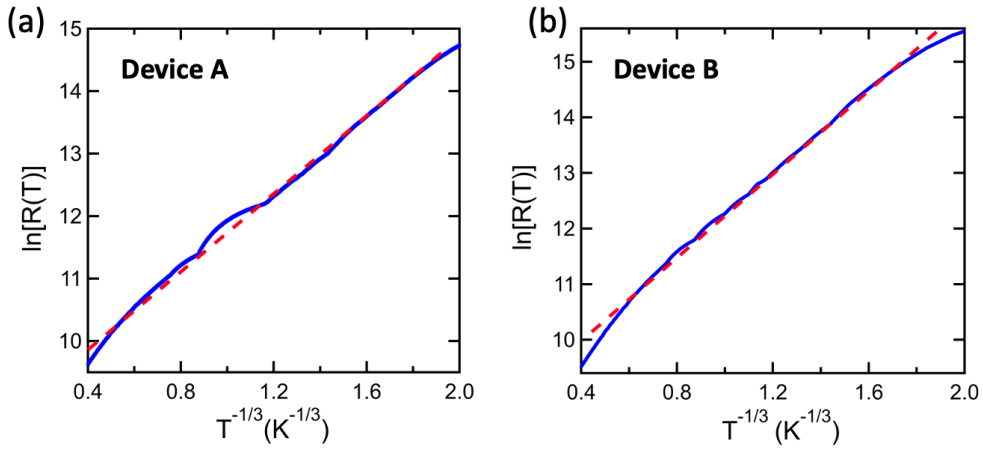

Figure 5.10: Logarithm of the low-temperature (15 K to 125 mK) resistance a function of $T^{-\frac{1}{3}}$ for $CsSnBr_3$ epitaxial thin films. (a) data from $CsSnBr_3$ device A, (b) $CsSnBr_3$ device B. The red dashed lines are fits to the data based on the temperature dependence of 2D Mott VRH transport.

Additionally, in Figure 5.12, we plot the temperature-dependent resistance data of our $CsSnBr_3$ devices at low temperatures (15 K to 100 mK) for various power laws to compare with other models. Figure 5.12 (a) and (d) are for NNH (T^{-1}), (b) and (e) compare with E-S VRH ($\ln[R(T)] \propto T^{-\frac{1}{2}}$, derived from Equation 5.23), and (c) and (f) are for 3D Mott VRH ($\ln[R(T)] \propto T^{-\frac{1}{4}}$, derived from Equation 5.13). These plots show that our low-temperature resistance data do not match the NNH and E-S VRH models since these data show non-linear dependences. In contrast, transport in our devices could be interpreted in the context of 3D Mott VRH (see Figure 5.12 (c) and (f)). The possibility of 3D Mott VRH can be ultimately ruled out by our observation of a large negative magnetoresistance as well as clear signatures of NSS physics from the $CsSnBr_3$ samples as will be discussed in Subsection 5.4.3 and 5.4.4.

5.4.3 Giant Negative Magnetoresistance in $CsSnBr_3$

To further reveal the coherent hopping transport of the charge carriers in our epitaxial single-crystal $CsSnBr_3$ thin film devices, we performed magnetoresistance measurements at different low temperatures up to large magnetic fields (i.e. up to ±13.5 T). In these measurements the applied

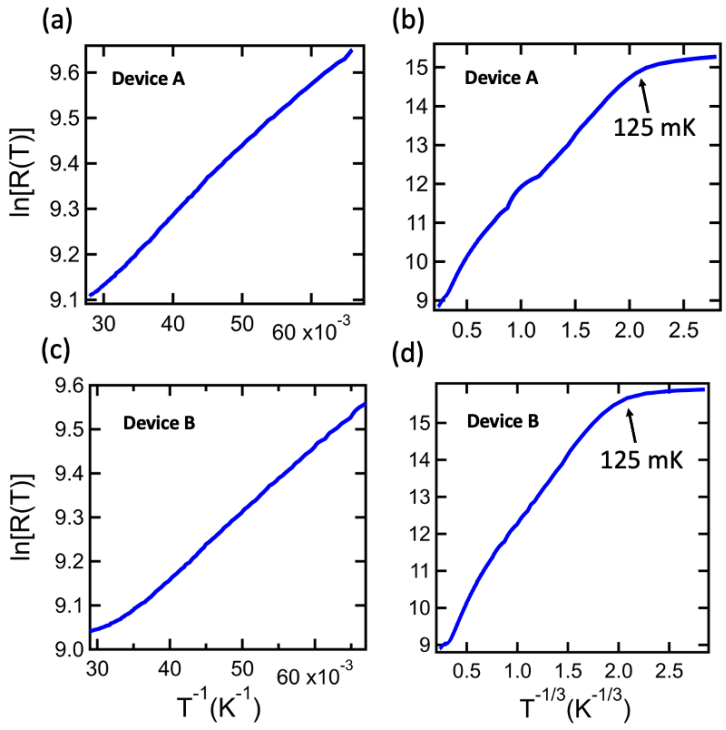

Figure 5.11: Power law temperature dependence of $CsSnBr_3$ device outside the 2D Mott VRH regime. (a) and (b) data are from $CsSnBr_3$ device A. (c) and (d) data are from $CsSnBr_3$ device B. (a) and (c) At high temperatures (35 K to 15 K), the $CsSnBr_3$ devices show thermally activated transport (NNH, and its characteristic temperature dependence of resistance is $\ln[R(T)] \propto T^{-1}$, converted from Equation 5.7). (b) and (d) At low temperatures (15 K to 125 mK), the devices show 2D Mott VRH transport as described in the main manuscript. Below 125 mK we find that the device resistance saturates, a phenomenon that is likely associated with thermal decoupling of the device from the cryostat. The data is from $CsSnBr_3$ sample A, and $CsSnBr_3$ sample B shows similar behavior.

magnetic field is normal to the epitaxial film. The result of the magnetoresistance for both devices are shown in Figure 5.13. We find a giant negative magnetoresistance with no sign of saturation over the full field range at low temperatures, and at $T = 0.5$ K, the ratio of $\frac{R(0)}{R(B)} > 2$. This is in contrast to WL (WAL) where the magnetoresistance only decreases by a few percent [10]. This is consistent with results shown in reports for GaAs/AlGaAs heterojunctions (see Figure 5.7 [52]) and In_2O_{3-x} films in the 2D VRH regime [89] and is consistent with the predictions of the NSS model. We find that the negative magnetoresistance peak is weakened as the device temperature is increased indicating a possible reduction in the length scale associated with phase-coherent hopping, which

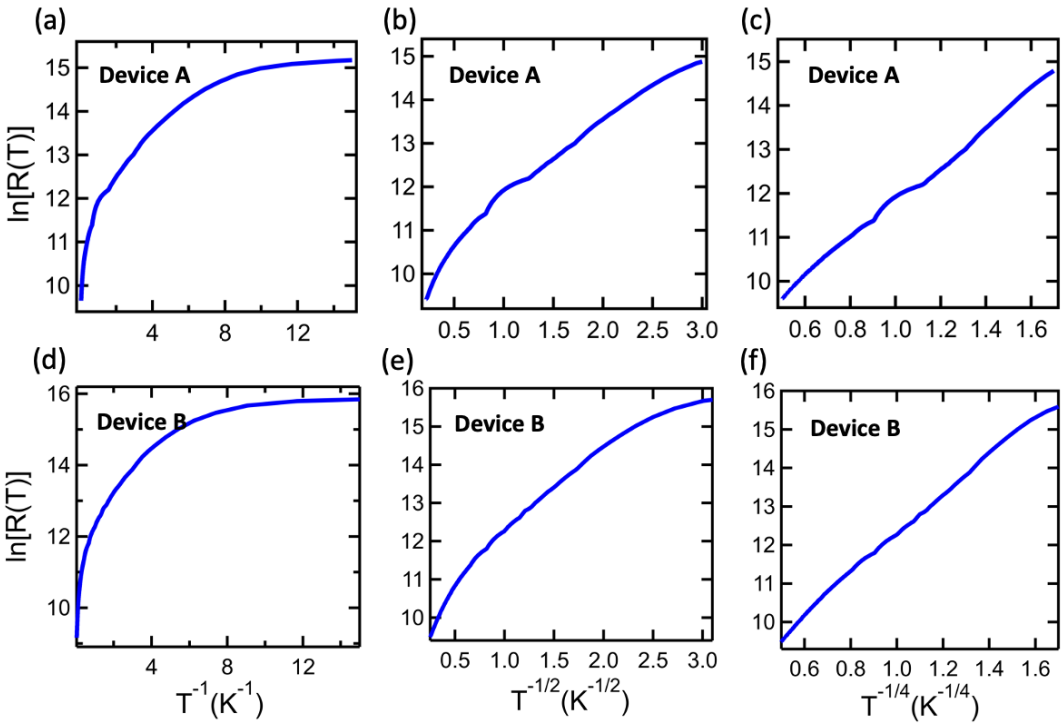

Figure 5.12: Checking of the temperature-dependence power law of $CsSnBr_3$ devices outside the VRH-regime at low temperatures (15 K to 100 mK) (a), (b), (c) are data from $CsSnBr_3$ device A. (d), (e), (f) are data from $CsSnBr_3$ device B. (a) and (d) are for checking NNH ($\ln[R(T)] \propto T^{-1}$), (b) and (e) are for checking E-S VRH ($\ln[R(T)] \propto T^{-\frac{1}{2}}$), (c) and (f) are for checking 3D Mott VRH ($\ln[R(T)] \propto T^{-\frac{1}{4}}$). Note that data from both samples do not fit to NNH and E-S VRH model.

could be caused by increased inelastic scattering from phonons or charge carriers. The weakening of the peak may also potentially result from a contribution from positive orbital magnetoresistance as the device temperature is increased.

5.4.4 Analysis of Different Length Scales in $CsSnBr_3$

We have plotted the magnetoresistance data in the form of natural logarithm of normalized magnetoresistance $\ln\left[\frac{R(B)}{R(0)}\right]$ as a function of $B^{\frac{1}{2}}$ in Figure 5.14, which clearly demonstrates the expected functional dependence as we discussed in NSS model (see Equation 5.35). The observation of the NSS physics further proves that our devices exhibit 2D rather than 3D Mott VRH behavior. The

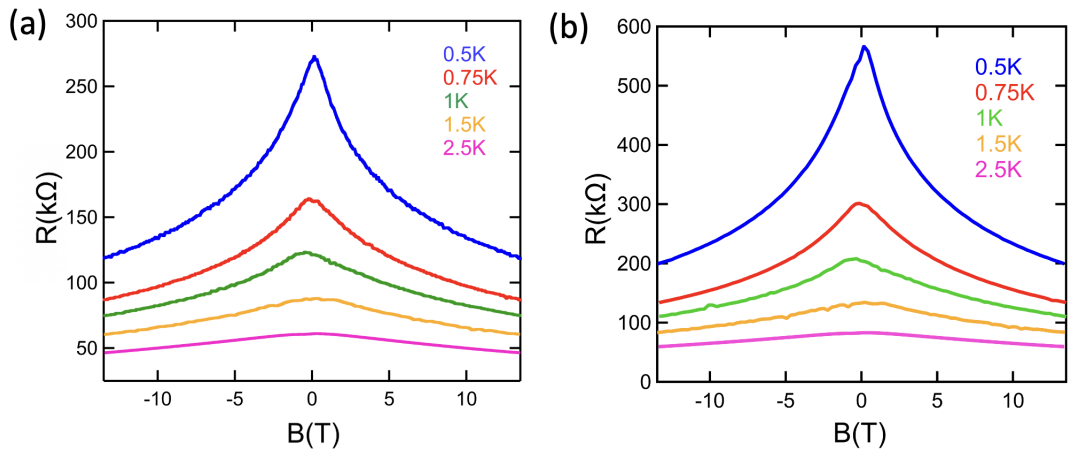

Figure 5.13: Magnetoresistance of two $CsSnBr_3$ epitaxial thin films at different low temperatures. (a) data from $CsSnBr_3$ device A. (b) data from $CsSnBr_3$ device B. Both devices show giant negative magnetoresistance with no sign of saturation. The applied magnetic field is normal to the $CsSnBr_3$ film. The peak of the magnetoresistance weakens as the temperature increases, indicating that the length scale associated with phase-coherent hopping is reduced. Note that at $T = 0.5$ K the ratio of $\frac{R(0)}{R(B)} > 2$ for both samples, which is significantly exceeding unity.

temperature-dependent hopping length $r(T)$ can be obtained from the slope of the linear regime in Figure 5.14, which yields $r(T) \cong 94$, 81, 67, 59 and 46 nm at 0.5, 0.75, 1, 1.5 and 2.5 K for $CsSnBr_3$ device A (128, 107, 87, 72 and 61 nm at 0.5, 0.75, 1, 1.5 and 2.5 K for $CsSnBr_3$ device B). According to Equation 5.14, in low-temperature 2D Mott VRH regime, $r(T)$ should have the following temperature dependence $r(T) = \xi \left(\frac{T_0}{T}\right)^{\frac{1}{3}}$. In the insets of Figure 5.14, we plot $r(T)$ as a function of $T^{-\frac{1}{3}}$, which show good agreement with this expected behavior for 2D Mott VRH and is independently consistent with our temperature-dependent resistance measurements at zero magnetic field. We also note that the corresponding localization length for charge carriers ξ can be determined from the slope of $r(T)$, from which we find $\xi \approx 30$ nm for $CsSnBr_3$ device A ($\xi \approx 37$ nm for device B).

Our measurements and analysis also allow us to place a lower bound on the phase coherence length for charge carriers in $CsSnBr_3$ In particular, the NSS model is applicable when the phase coherence length l_ϕ is longer than $r(T)$. In this limit the hopping paths retain phase coherence. Equation 5.35 also requires that the magnetic length l_B be shorter than the hopping length $r(T)$, so that there

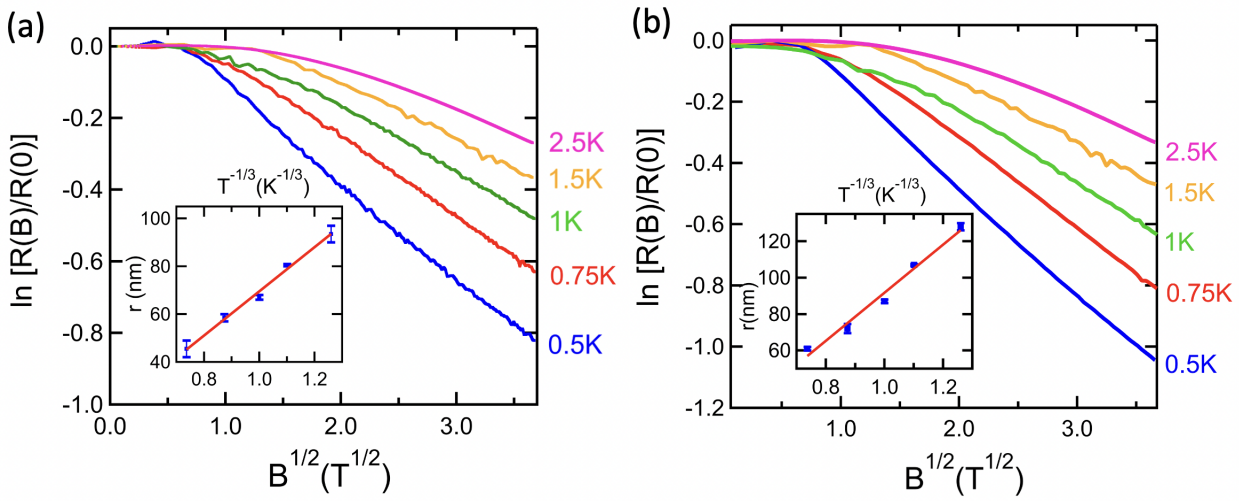

Figure 5.14: Logarithm of the normalized magnetoresistance $\ln\left[\frac{R(B)}{R(0)}\right]$ as a function of the square root of the magnetic field $B^{\frac{1}{2}}$ at different temperatures as indicated. (a) Data from $CsSnBr_3$ device A. (b) Data from $CsSnBr_3$ device B. Inset: temperature-dependent hopping length $r(T)$ as a function of $T^{-\frac{1}{3}}$.

are multiple quanta of magnetic flux through a typical closed-loop hopping path, and the magnetic field strongly alters the phase of the charge carrier trajectories. Our observations in aggregate indicate good agreement with the NSS model suggesting that both conditions are fulfilled, and the hierarchy of length scales $l_B \leq r(T) \leq l_\phi$ is achieved. In Figure 5.14 at $T = 0.5$ K, from both devices, we observe linear dependence of $\ln\left[\frac{R(B)}{R(0)}\right]$ on $B^{\frac{1}{2}}$ for all values of $B^{\frac{1}{2}} \geq 0.6\,T^{\frac{1}{2}}$ with a weaker dependence at smaller fields. This high-field regime corresponds to $l_B \leq 40$ nm, and the condition $l_B \leq r(T = 0.5\text{ K})$ is satisfied. While we cannot directly measure the phase coherence length l_ϕ in the VRH regime, the requirement that l_ϕ is greater than $r(T = 0.5\text{ K})$ implies a phase coherence length significantly larger than at least ~ 100 nm for both of $CsSnBr_3$ devices. This is consistent with the notably high phase coherence length measured in our epitaxial $CsSnI_3$ thin film device [94].

5.5 The Resemblance of Nguyen Spivak and Shkovskii Model and Weak (Anti-) Localization in Epitaxial Halide Perovskites

This section serves as a summary of the NSS model discussed in 5.3 and discusses its similarities and differences to the theory of WL (WAL) discussed in Section 4.4.

In Figure 5.15 we present a qualitative picture of these two modes of quantum coherent transport, where WL (WAL) is observed in our epitaxial $CsSnI_3$ device and NSS is observed in our epitaxial $CsSnBr_3$ device. A schematic of the corresponding transport regimes for both models are shown, along with the different scattering paths and scattering centers. The various relevant length scales, including the temperature-dependent typical hopping length $r(T)$, the charge carrier localization length at zero magnetic field ξ, and the phase coherence length l_ϕ, are also shown in Figure 5.15 along with their sizes relative to each other.

In the quantum diffusive transport regime, which arises at a higher charge carrier density relative to the VRH regime, the coherence among multiple elastic scattering paths of a single electron can lead to an enhancement of backscattering, as shown in Figure 5.15 (a). An externally applied magnetic field introduces relative phase shifts between different scattering paths and thus leads to relatively small negative magnetoresistance, which is the hallmark of WL [10]. WAL has the same physical nature as WL, but with the additional phase imparted on the electron spin via spin-orbit interaction. This spin-orbit effect in WAL leads to relative small positive magnetoresistance near $B = 0$. In analogy to WL (WAL), coherent transport can also appear at significantly lower charge carrier density in the Mott VRH regime and can also be modified by an externally applied magnetic field. To understand the magnetoresistance in the hopping regime, the NSS model considers the overall hopping amplitude between localized sites as the sum of amplitudes of different tunneling trajectories, each of which involves an electron or hole passing virtually through multiple localized impurity states, as depicted in Figure 5.15 (b). When an external magnetic field is applied, a phase shift is introduced that can coherently modify the overall hopping amplitude and lead to a large negative magnetoresistance [137, 115]. So, in a nutshell the NSS physics we observe in epitaxial $CsSnBr_3$ films is a analog of WL (WAL) in the Mott 2D VRH regime. The fact

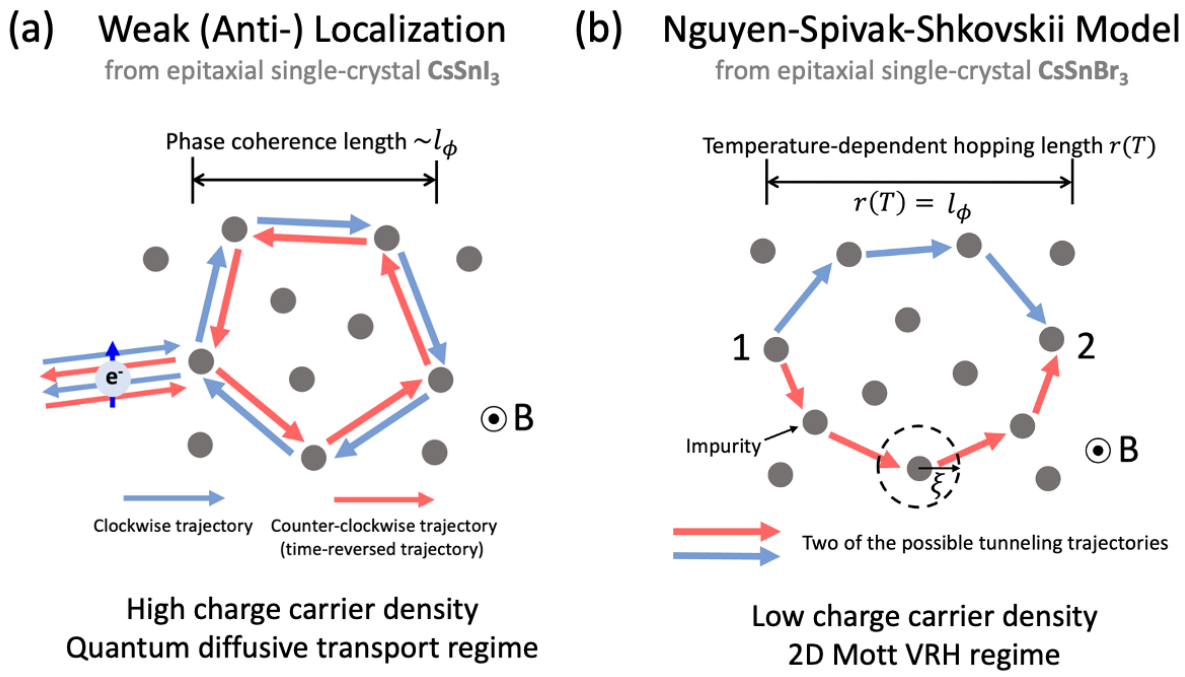

Figure 5.15: Qualitative picture of two modes of quantum coherent transport in 2D systems. The gray dots represent impurities (sites of elastic scatterings). Three different length scales, the phase coherence length l_ϕ, the temperature-dependent hopping length $r(T)$, and the localization length ξ, are indicated. (a): Model of WL (WAL) in a conductor. Blue (red) arrows show clockwise (counterclockwise (time-reversed)) diffusive trajectories. The electron spin is only considered in WAL. (b) NSS model based on 2D Mott VRH in an insulator. A charge carrier tunnels from site 1 to an energetically favorable site 2. The red path and the blue path represent two possible tunneling trajectories, which contribute to the overall hopping amplitude from site 1 to 2.

that we can observe different coherent transport effects in our halide perovskite devices adds to the growing body of evidence demonstrating that epitaxial halide perovskite thin film devices are emerging as an exciting new class of low-dimensional quantum electronic materials. As the quality of epitaxial halide perovskite materials continues to improve via advances in growth, doping, and strain engineering, one can expect the emergence of ever more subtle and exotic electronic states of matter (such as the quantum Hall and fractional quantum Hall states discussed in Chapter 1) in these materials at low temperatures. Additionally, leveraging the advances of halide perovskite epitaxy opens the door for developing high-quality devices exhibiting symmetry-broken collective states.

CHAPTER 6

CONCLUSIONS AND FUTURE DIRECTIONS

In conclusion, we have presented quantum coherent transport in epitaxial single-crystal halide perovskites thin films. In particular, we have observed WAL in $CsSnI_3$ in the quantum diffusive regime, and a large negative magnetoresistance in $CsSnBr_3$ which can be explain using NSS model for 2D coherent Mott VRH. These coherent quantum transport phenomena demonstrate the great potential that halide perovskites have as a new class of materials for making future quantum electronic devices. The following are several future directions that could be explored with these materials.

Effects of Doping and Thickness

In magnetoresistance measurements on epitaxial single-crystal $CsSnI_3$ samples, we found that

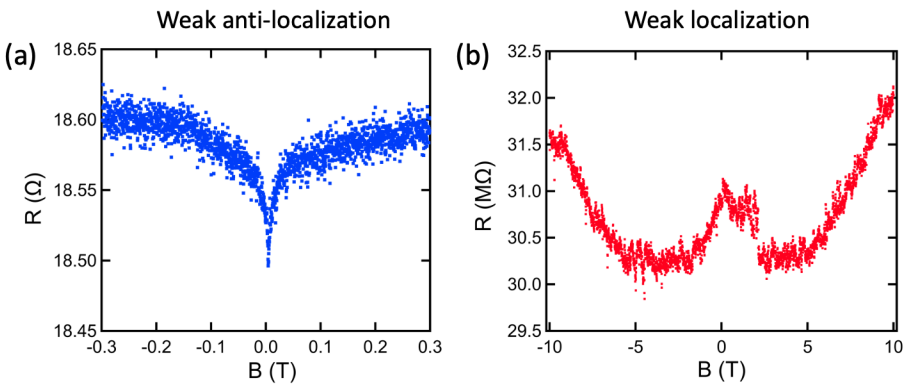

Figure 6.1: (b) Magnetoresistance of one $CsSnI_3$ epitaxial thin film at T = 250 mK showing WAL. (b) Measurement on another $CsSnI_3$ epitaxial thin film at T = 10 mK showing WL.

most samples show WAL and have relatively low resistance at low temperatures as shown in Figure 6.1 (a). However, some $CsSnI_3$ samples exhibited high resistance at low-temperatures and showed behavior resembling WL, as shown in Figure 6.1 (b). These differences could be caused by difference in sample thickness and variations in doping. Thus, the systematic investigation of the transport properties on halide perovskite with varying film thickness could be performed to explore

the transition from 2D-to-3D quantum transport as a function of vertical confinement. Additionally, systematic studies with variable doping could be performed to investigate the conducting properties of these semiconductor materials.

Four-Terminal Measurements on van der Pauw Device

Another future direction would be to develop four-point quantum transport measurements on

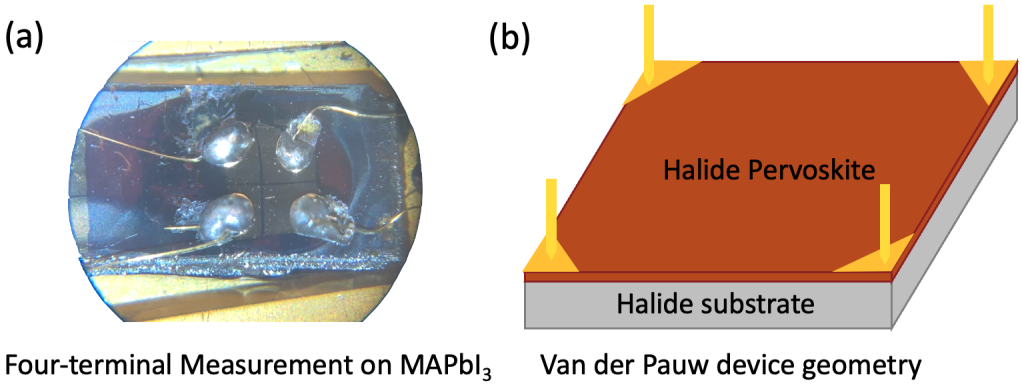

Figure 6.2: (a) Photo of a $MAPbI_3$ thin film in a four-terminal measurement. (b) Schematic figure of a halide perovskite device with van der Pauw device geometry.

halide perovskite thin films and van der Pauw and Hall bar device geometries (see Figure 6.2 (b)). Four-point measurements would enable measurements to systematically characterize the charge mobility, density, and carrier type in these materials over an wide range of growth parameters including doping and disorder. Additionally, we have already made progress in this direction and have realized conventional four-terminal measurements on methylammonium lead iodine ($MAPbI_3$) thin films (see Figure 6.2 (a)).

Surface Acoustic Wave Measurements on Halide Perovskites Thin Films

Inspired by our previous work, in which we demonstrated that the charge carriers in graphene can be driven by surface acoustic waves (SAWs) [68], one could perform acoustoelectric measurements on halide perovskites, especially single-crystal $CsSnI_3$ devices which have demonstrated high charge carrier density. A SAW is an elastic wave that propagates along the surface of a piezoelectric material, and have been used to studying 2DESs. SAWs can be generated (and detected) using

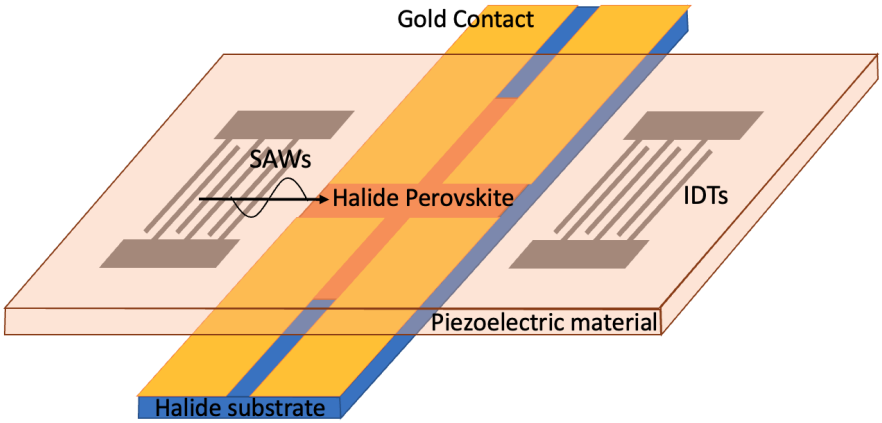

Figure 6.3: Schematic figure of a proposed "flip-chip" device. The top layer is a piezoelectric material, where interdigitated transducers (IDTs) are fabricated onto the bottom side. A surface acoustic wave (SAW) can be generated from either pair of IDTs. The bottom layer is a halide perovskite thin film device with four gold contacts.

interdigitated transducers (IDTs) fabricated on the piezoelectric substrate. A new halide perovskite device based on a "flip-chip" geometry is shown in Figure 6.3.

High Magnetic Field (45 T) Magnetotransport Measurements

As discussed in Chapter 1, an exciting possibility would be to observe the IQHE or even the FQHE in epitaxial halide perovskite 2DES. As device quality increases, samples could be taken to the US National High Magnetic Field Laboratory to perform magnetoresistance measurement up to 45 T. This significantly larger field could reveal the presence of quantum oscillation (i.e. Shubnikov–de Haas effect), which is a precursor to the quantum Hall effects introduced in Chapter 1.

APPENDICES

APPENDIX A

STUDYING BI-LAYER GRAPHENE USING RESISTIVELY DETECTED MICROWAVE METHODS

In this appendix, we will first give a brief introduction to 2DESs based on bi-layer graphene (BLG). Then we will discuss the van der Waals assembling technique, and how to reveal unique properties of different types of BLG systems subject to an electric displacement field. Finally, we will present our preliminary experimental efforts to study resistively detected microwave absorption on BLG heterostructures. The data presented in this section is based on experiments on a high-quality **twisted bi-layer graphene (tBLG)** device, which was fabricated by collaborators in the group of Professor Jia Li at Brown University.

Twisted and A-B Stacked Bi-Layer Graphene

Monolayer graphene (MLG) consists of a single layer of carbon atoms with a honeycomb crystal structure. BLG consists of two layers of MLG. The electrical properties of different BLGs are distinct from each other due to the orientation of the stacking of the two MLG layers. Here, we will describe two of the common stackings, namely tBLG and Bernal-stacked or A-B stacked bi-layer graphene (AB-BLG).

The crystal structure of tBLG is shown in Figure A.1 (a), where two MLGs are stacked onto each other with a relative twist angle θ between the layers. In momentum space, this angle θ causes a decoupling of the Dirac cones of each layer of MLG, which leads to many of the unique properties of the tBLG [42]. When $\theta \approx 1.1^{\circ}$, tBLG tends to exhibit an intrinsic superconductivity and the system is referred to as magic angle tBLG [13]. We note that, our tBLG is not magic angle graphene.

In MLG, each unit cell contains two carbon atoms and the positions of the two atoms are not equivalent. The unit cell of AB-BLG contains four atoms, which are labeled as A1, B1 on the top layer and A2, B2 on the bottom layer (see Figure A.1). The two layers are arranged so that the the

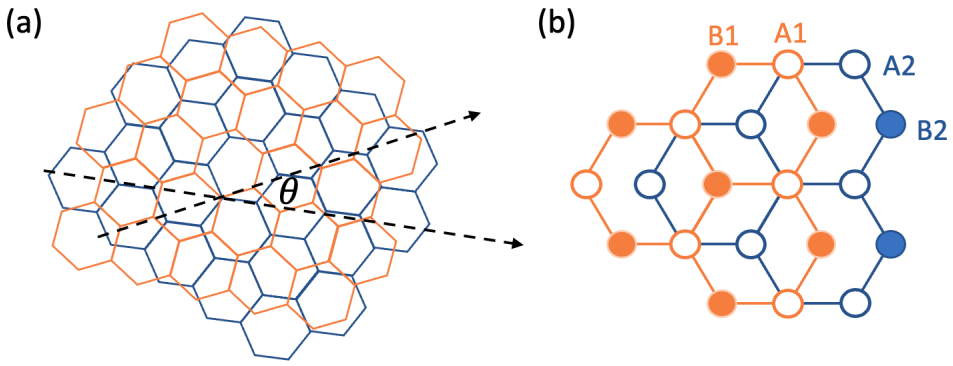

Figure A.1: Schematic representation of two BLG crystal structures, orange and blue indicate top and bottom layers of MLG. (a) Twisted bi-layer graphene (tBLG): Two graphene layers are rotated relative to each other by angle θ. (b) Bernal-stacked bi-layer graphene (AB-BLG): Atoms A1(A2) and B1(B2) on the top(bottom) layer are shown as empty and solid circles.

atom A1 in the top layer is directly above the atom B2 in the bottom layer. These two atomic sites are often referred as "dimer" sites because the electronic orbitals on them are coupled together by a relatively strong interlayer coupling. The other two atoms, B1 and A2, do not have a counterpart on the other layer that is directly above or below, and these atomic sites are often referred to as 'non-dimer' sites [86].

Van der Waals Assembing Technique and Device Geometry

Here we will briefly discusse the fabrication techniques used to produce tBLG device studied in this dissertation. Without special fabrication, the electrons in a graphene device are exposed to disturbances and fluctuations that come from the surrounding substrate onto which a device is produced. Consequently, experimental efforts to study electron states in graphene 2DESs can be limited by poor device quality. The van der Waals heterostructure has emerged as a successful technique that provides the flexibility in assembling more complex structures, which help the resulting devices to achieve higher quality and allow for more intricate device functions [128, 20].

Recently it has been demonstrated that the van der Waals assembly technique can be used to create high device quality 2D electron layers in graphene (MLG, BLG, etc.) and other 2D materials by isolating the 2DESs from outside influences with hexagonal boron nitride (hBN) and

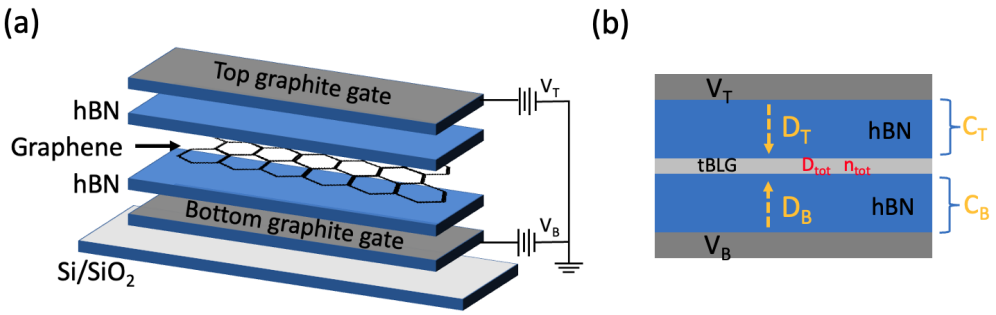

Figure A.2: (a) Schematic of a high-quality graphene heterostructure fabricated using van der Waals assembly technique, where the graphene (MLG, BLG, etc.) layer is encapsulated by dual graphite and hexagonal boron nitride (hBN) crystals. In the final device structure, the graphite crystals serve as top and bottom gate electrodes with hBN as the gate dielectric. (b) Schematic drawing of the cross section of an encapsulated tBLG device. D_T and D_B are the displacement fields in top and bottom hBN layers. Notice that in general, the capacitance C_T and C_B have different values.

graphite encapsulation. The layout of the encapsulation is shown in Figure A.2. With similar lattice structure as graphene and most other 2D materials, hBN serves as an ideal lattice matched substrate and the graphite layers are an atomically flat gate electrode capable of tuning charge carrier with high homogeneity [20]. This van der Waals technique has enabled in the discovery of exotic even-denominator fractional quantum Hall (QH) states in bilayer graphene [73], which is regarded as one of the most fragile collective electron states in 2D systems.

The tBLG discussed in this appendix was fabricated using the van der Waals technique and its device geometry is shown in an optical microscope image in Figure A.3. The Hall bar geometry of this device allows for four-terminal measurements. In Figure A.3 the top graphite gate and bottom graphite gate (not shown) are used to control the total charge carrier density and apply a displacement field to the tBLG layer. A contact gate surrounds the tBLG and is not physically connected to any other electrodes. This contact gate is used to induce a large carrier density in the contact to reduce its contact resistance.

Displacement Field on Bi-Layer Graphene

In the following, we will discuss the charge neutrality point (CNP) of MLG and the effect of the

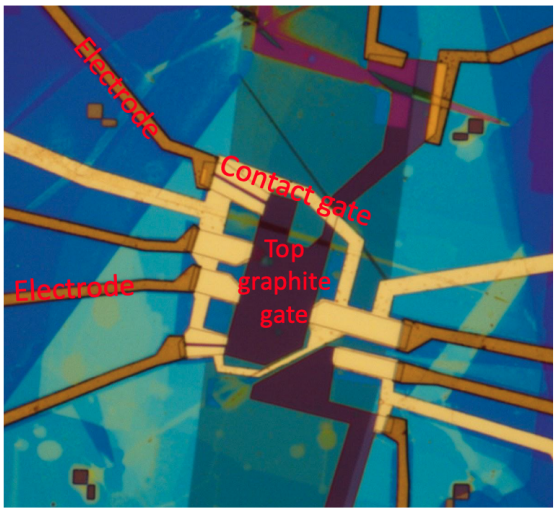

Figure A.3: The optical microscope photo of the tBLG device. The tBLG is beneath the top graphite gate. The contact gate and multiple electrodes are also indicated in this figure.

displacement field that can be applied to our tBLG device. At low temperatures, the electronic band structure of MLG at the vertices of the hexagonal Brillouin zone form linearly dispersing Dirac cones. Without the application of the external electric field, the Fermi level will reside at the CNP (also called the Dirac point) where the MLG device will have the largest resistance. In an ideal device, neither the holes nor electrons will be present as charge carriers [96] at the CNP, and the MGL device will have its lowest charge carrier density. Similar behavior can be observed from a tBLG device as shown in Figure A.4 (a). As discussed earlier, the tBLG device was assembled using van der Waals technique and allows for independent control of V_T and V_B. In the initial resistance characterization measurement of the tBLG device, we fix the voltage of the bottom graphite gate $V_B = 0$ V and sweep the voltage applied to the top graphite gate V_T. This measurement leads to a similar result to that from MLG. The maximum resistance occurs at $V_T = 0$ V where the Fermi level is at the CNP. The narrow Dirac peak also demonstrates the high quality of the tBLG device.

The next measurement we performed on the tBLG device was to sweep V_T and V_B independently and to create a map of R_{xx} (see Figure A.4 (b)). This measurement reveals more features of electrical transport in the tBLG device and helps to characterize device parameters. In this map, the high resistance regions in bright colors is due to the CNP. In the ideal case, this region should go from

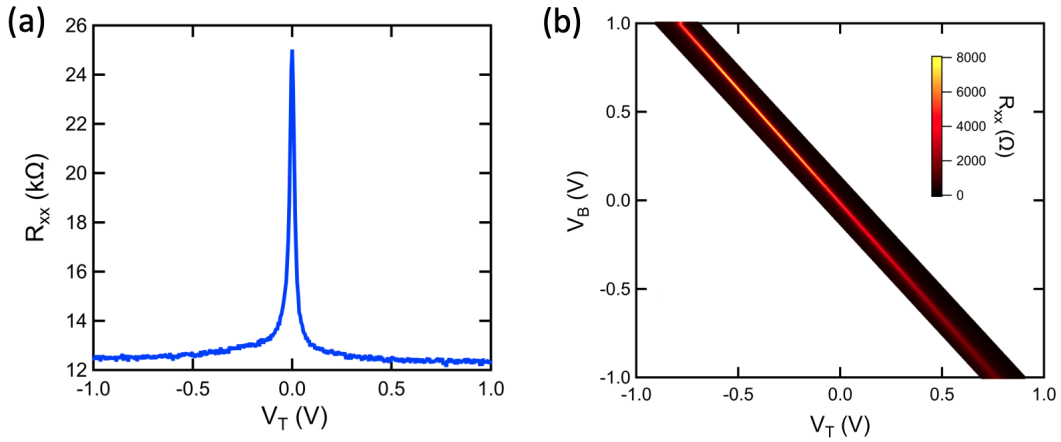

Figure A.4: (a) R_{xx} of the tBLG device as a function of V_T at 3 K, V_B is fixed at 0 V. (b) Partial displacement field map of R_{xx} of tBLG device, the horizontal and vertial axes shows V_T and V_B. The value of R_{xx} in the white regions in this map are close to 0.

($V_T = -1$ V,$V_B = 1$ V) to ($V_T = 1$ V,$V_B = -1$ V). The discrepancy between the data in Figure A.4 (b) and the expectation from an ideal device is caused by the difference in capacitance of top and bottom layer of hBN (see Figure A.2 (b)). Additionally, the total displacement field D applied to the tBLG and total charge carrier density n_{tot} of the tBLG can be calculated as the follows:

$$D = \frac{C_T V_T - C_B V_B}{2\epsilon_0} \tag{A.1}$$

$$n_{\text{tot}} = \frac{C_T V_T + C_B V_B}{e} - n_0\,, \tag{A.2}$$

where ϵ_0 and e are the vacuum permittivity and elementary charge. C_T (C_B) is the geometric capacitance between the top (bottom) graphite gate and the tBLG. The parameter n_0 is the intrinsic doping of the tBLG, and D is the total displacement field. From Equation A.2 and the charge neutrality line in Figure A.4 (b), we can easily determine the ratio of $\frac{C_T}{C_B} = 1.28$ for our tBLG device. The value of C_T and C_B can be obtained by properly aligning the Landau filling factor to the quantum Hall (QH) features in Figure A.6, which results in $C_T = 0.63$ mF and $C_B = 0.49$ mF.

Another notable feature in Figure A.4 (b) is the variation in the Dirac peak as a function of gate voltage. To show this variation more clearly, we fix V_B at different values while sweeping V_T, as shown in Figure A.5 (a). In this figure, the top horizontal axis shows the total displacement field

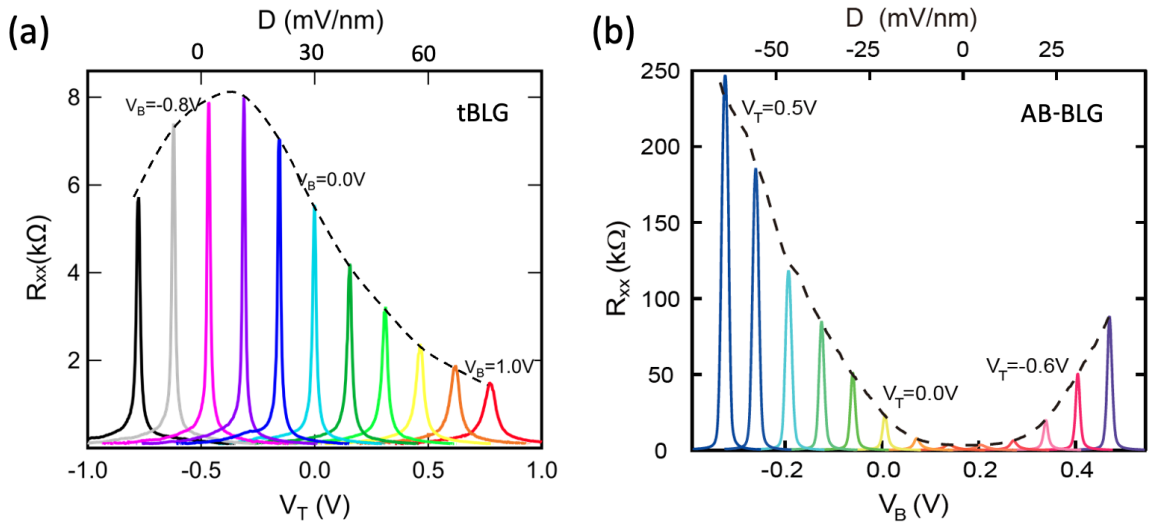

Figure A.5: (a) Data from tBLG, R_{xx} is measured as a function of top gate voltage V_T at different fixed bottom gate voltage V_B. (b) For comparison, data from Ref. [73] is shown for AB-BLG

which is calculated from V_T and V_B using Equation A.1. Different colors correspond to different values of V_B. As one can see, the peak of R_{xx} at different values of V_B decreases as $|D|$ increases. This observation can be explained by the following: tBLG remains overall charge neutral at CNP, but as $|D|$ increases, electrons start to populate one graphene layer and holes start to populate the other layer. As a consequence, the device becomes less resistive at CNP. This unique behavior reflects the interlayer coupling of the tBLG. For comparison, data from a AB-BLG sample is shown on Figure A.5 (b) [73], in which a large value of $|D|$ breaks the inversion symmetry between the layers and opens a gap near CNP [96], leading to an increase in resistance with increasing $|D|$.

By independently controlling V_T and V_B and calculating D and the Landau filling factor ν using Equation A.1, A.2 and 1.17, we can obtain a map of σ_{xx} as a function of D and ν, as shown in Figure A.6. Multiple IQHE and FQHE features are observed, such as the fractional states at $\nu = -\frac{4}{3}$ and $-\frac{5}{3}$ near $\nu = -\frac{3}{2}$, and $\nu = -\frac{7}{3}$ and $-\frac{8}{3}$ centered around $\nu = -\frac{5}{2}$.

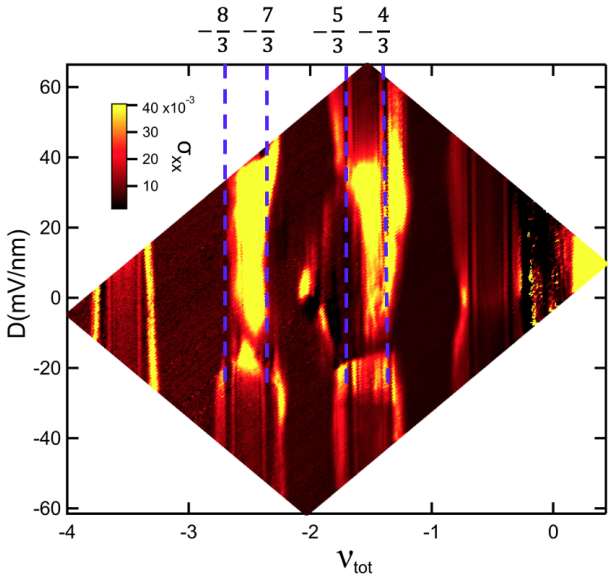

Figure A.6: A map of σ_{xx} versus filling factor ν and displacement field D. The data is taken from a tBLG device at $T = 13$ mK and $B = 13.2$ T. The contact gate voltage V_c is at -4V.

Electron Spin Resonance in Graphene Heterostructures and Attempt to Measure Microwave Electron Spin Resonance in Bi-layer Graphene

In this section, we discuss an attempted measurement of resistively detected electron spin resonance (ESR) in high quality tBLG devices and show the preliminary results.

tBLG has multiple electronic degrees of freedom (DOF). Application of microwave radiation onto tBLG can induce transitions with resonant DOFs. In particular, applying a magnetic field to graphene, the energy level of electrons will split due to the Zeeman effect.

$$\Delta E = E_{+1/2} - E_{-1/2} = g\mu_B B \tag{A.3}$$

The equation above describes the energy difference between the spin-up and down states. In this equation, g is the Lande g-factor, $\mu_B = \frac{e\hbar}{2m_e} = 9.274 \times 10^{-24}$ J·T^{-1} is the Bohr magneton, and m_e is the electron mass.

$$\Delta E = hf, \quad g = \frac{hf}{\mu_B B} \tag{A.4}$$

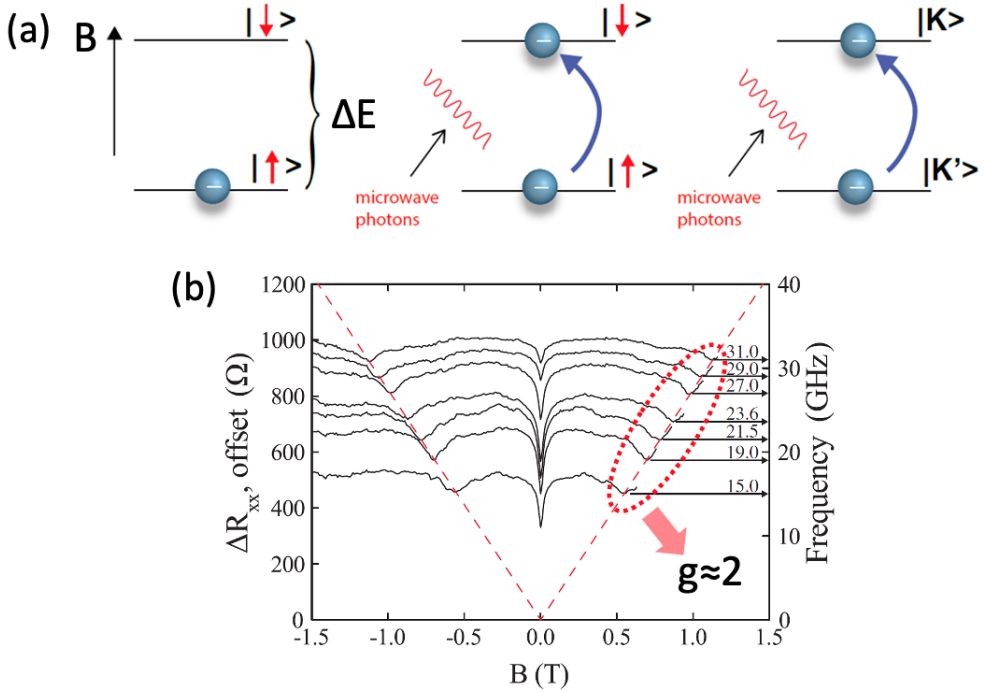

Figure A.7: (a) **Left:** In an external magnetic field, electrons with differing spin are separated by the Zeeman energy, resulting in an ensemble of two level systems. **Middle:** When microwave photons match this Zeeman splitting, electrons in the lower energy branch can absorb a photon and hop into the higher energy branch, creating a resonance detectable in transport measurements. **Right:** Similar resonances can also be induced when the photon energy matches an energy gap associated with a different quantum number, such as valley isospin K and K' (b) Example of resistive detected ESR measurement on CVD graphene. The data is from Ref. [81]. The measurement showed ΔR_{xx} (which is the difference in R_{xx} with microwaves on and off) for different microwave frequencies at the CNP, with offsets to emphasize ESR peak shift due to a g-factor equals to 2. The traces are offset to make the peak value in resistance coincide with the microwave frequency at which the magnetoresistance curve was recorded.

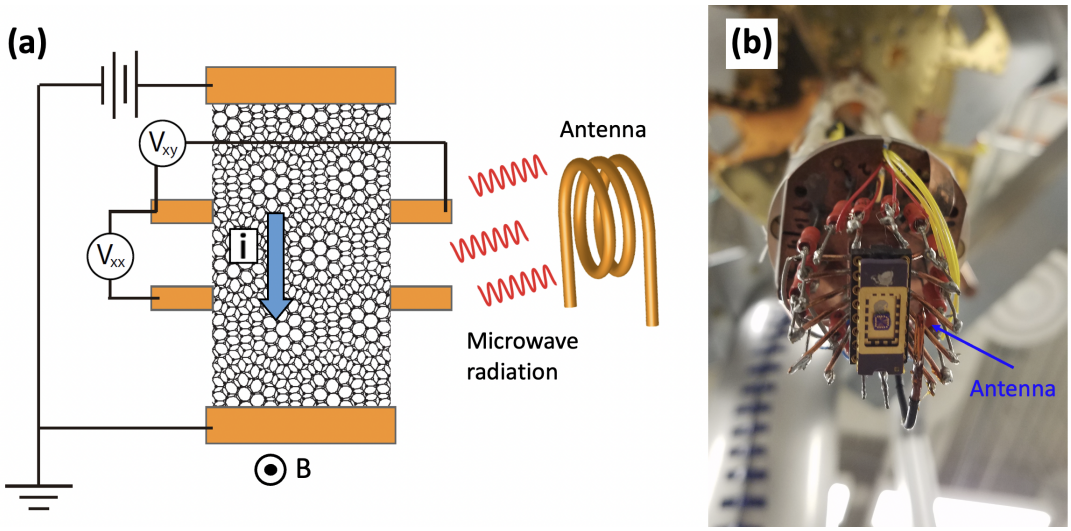

Figure A.8: (a) Schematic of the measurement setup for performing low-frequency transport in the presence of microwave radiation in a tBLG device. (b) Photo of the tBLG device on a chip carrier with microwave antenna attached independently on the right.

As shown in Equation A.4, relative population between different spin orientations can be reversed under the influence of microwave radiation, when the energy of a microwave photon (with frequency f) matches the energy cost to flip an electron spin (shown in Figure A.7 (a)). Such population reversal is potentially detectable as changes in the sample resistance. Figure A.7 (b) is an example of resistively detected ESR measurements performed on chemical vapor deposition (CVD) grown graphene. Similar effects have also been reported from monolayer and trilayer epitaxial graphene [84]. From these measurements, one can derive the Lande-g factor (shown in Equation A.4). The measurements in Ref. [81, 84] were performed using relatively disordered graphene samples, where the resonance frequency and external magnetic field correspond to a gyromagnetic ratio of $g \approx 2$. This value of the g factor is consistent with non-interacting free electrons in graphene. Similar measurements performed on high-quality tBLG could unveil information about interactions and spin textures.

Measurements and Preliminary Results

Figure A.8 shows how we performed the microwave ESR measurements on a high-quality

tBLG device. The measurements performed are four-terminal lock-in measurements of the device resistance with a microwave antenna attached independently near the device so that microwave irradiation can be applied. We first tested if we could couple microwave power to the tBLG at a temperature $T = 20$ mK. As shown in Figure A.9, we observed microwave induced electron heating, since the QH plateaus disappeared as we increased the microwave power from -20 dBm to +4 dBm. There was no noticeable change of the mixing chamber temperature during this measurement, which indicates the transfer of the microwave energy to the electrons in the device, and the disappear of the QH plateaus is caused by the electron-electron scattering due to the heating effect.

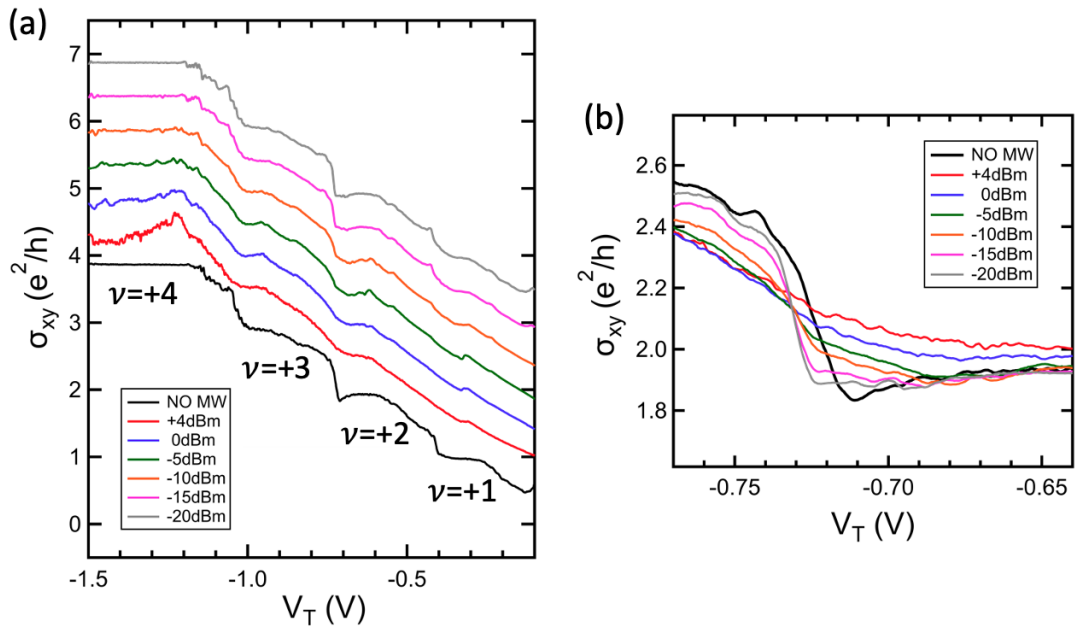

Figure A.9: Quantum Hall (QH) measurements on the tBLG device with microwaves applied. The four QH plateaus disappear when high microwave power is applied, which indicates the electron heating effect. (a) σ_{xy} data with offset in unit of $\frac{e^2}{h}$ versus top gate voltage (-1.5 V $\leq V_T \leq -0.1$ V) with different microwave powers applied. The measurement is performed at applied magnetic field $B = 5$ T, microwave frequency $f = 1$ GHz, mixing chamber temperature $T = 20$ mK and contact gate voltage $V_c = -4$ V. (b) Same σ_{xy} data as shown in (a) without offset at $\nu = +2$.

Next, we performed a Landau fan measurement on the tBLG while sweeping the magnetic field B and top gate voltage V_T, and simultaneously measuring the longitudinal resistance R_{xx}.

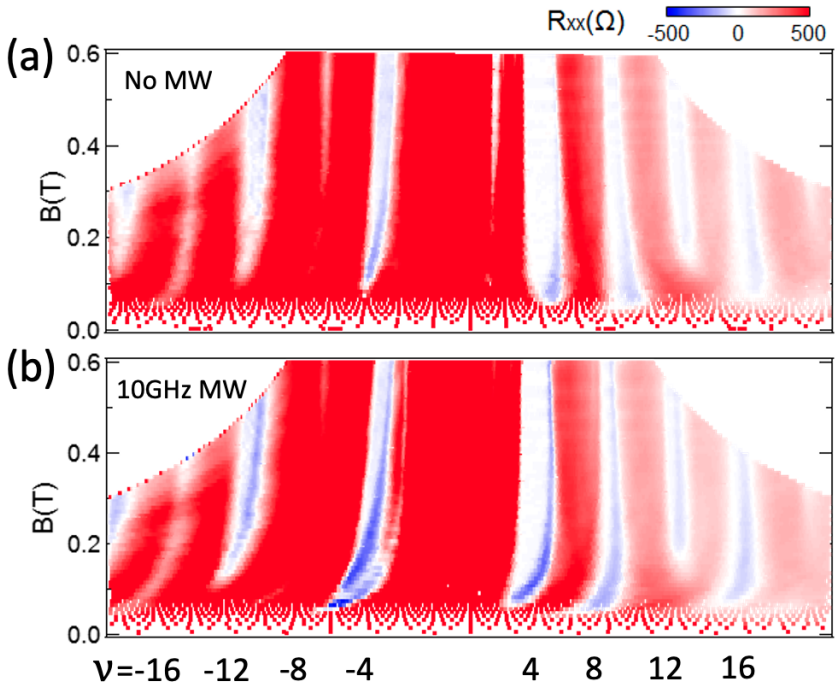

Figure A.10: Landau fan diagram of the magnetoresistance R_{xx} as a function of Landau filling factor ν and magnetic field B. Data is measured from a tBLG device at $T = 13$ mK. The contact gate voltage $V_c = -4$ V. (a) R_{xx} without applying microwave. (b) R_{xx} shows negative resistance features (in blue color) when -20 dBm microwave is applied. These features followed with Landau filling factors indicated in this figure.

Figure A.10 (a) is the resulting Landau fan without application of microwaves, multiple vertical stripes correspond to different Landau filling factors can be seen distinctly. When we applied microwaves, in Figure A.10 (b), negative resistance features (in blue color) appeared and near different Landau filling factors. The origin of the negative resistance features has not been identified, but they may be produced by changes in the contact resistance produced by heating.

We attempted to see evidence of microwave ESR in two different BLG devices. Figure A.11 (a) is a measurement of R_{xx} from one tBLG device (called Drag074), in which we adjusted the total charge carrier density n_{tot} and microwave frequency as two variables. Furthermore, we performed a measurement on another high quality encapsulated AB-BLG device (called BL002). The measurement result from this AB-BLG is shown in Figure A.11 (b), which is a map of ΔR_{xx} ($\Delta R_{xx} = R_{xx}(\text{microwave power=+15 dBm}) - R_{xx}(\text{microwave power=-30 dBm})$) with B and

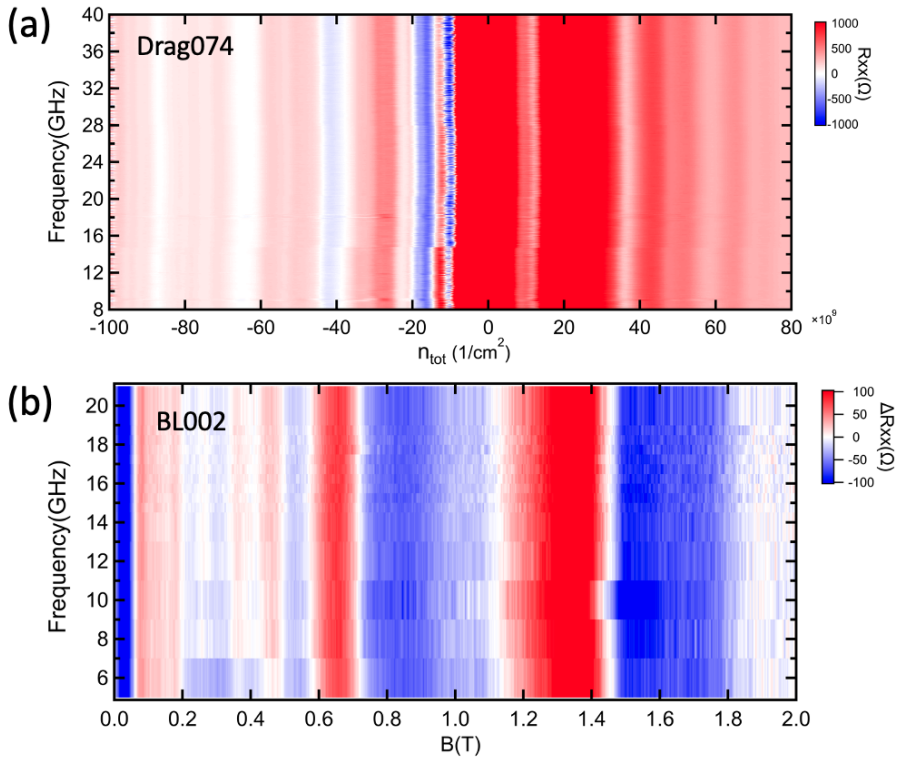

Figure A.11: (a)Measurement of R_{xx} on tBLG device (Drag074) as a function of microwave frequency and total charge carrier density n_{tot}. Microwave frequency is from 8 GHz to 40 GHz in 2 GHz increments with power of -30 dBm. Measurement is performed at T = 13 mK and $B = -0.1$ T. (b) ΔR_{xx} measurement on a AB-BLG device (BL002) as a function of microwave frequency and B. $\Delta R_{xx} = R_{xx}(\text{microwave power=+15 dBm}) - R_{xx}(\text{microwave power=-30 dBm})$. Microwave frequency is from 6 GHz to 20 GHz in 2 GHz increments. Measurement is performed at T = 13 mK.

microwave frequency as the two adjustable variables. This measurement is similar to what is shown in Figure A.7 (b) from Ref. [81]. The results from these two BLG devices show no noticeable sign of microwave ESR, this may indicate that the ESR features previously seen in other graphene devices might arise from different sources, as discussed in Ref. [81].

APPENDIX B

WEAK ANTI-LOCALIZATION FITTING

In this appendix, we present codes for obtaining the phase coherence length l_ϕ and α from fitting low-temperature magnetotransport measurements on epitaxial single-crystal $CsSnI_3$ thin film devices. The fitting function is the simplified empirical HLN formula, as shown in Equation 4.25. These codes are executed in Wolfram Mathematica. The input data are the measured voltage drop across the two gold contacts on the $CsSnI_3$ thin film, and the measured voltage drop across a resistor in series with the magnet winding. The output file includes fitted l_ϕ, fitted α, original data trace (magnetic field B versus difference in device conductivity $\sigma(B) - \sigma(0)$) and the fitted data trace. Other important comments are listed alongside the following codes.

```
In[ ]:= e=1.6×10^-19;
h=6.62607004×10^-34;
hbar=h/2π;
W=2×10^-3; (*Length and width of the gap between two gold pads*)
L=5×10^-5;

(*Function for processing raw data and convert it to unfitted [B; σ(B) - σ(B=0)]*)
normdata[data_,window_]:=Module[{output,dataB,DataSigma,m,data2,Sigma0},
  m=Length[data];        (*Convert measured voltage to magnetic field B*)
  dataB= data[[All, 2]]*1000*3*0.1313;        (*Convert measured voltage to conductivity σ*)
  DataSigma=(4.6×10^-6 /data[[All, 3]])*(L/W)*(h/e^2);
  data2 = Table[{ dataB[[i]],DataSigma[[i]]},{i, 1,m}];
  Sigma0=Max[Select[data2,-0.01<#[[1]]<0.01&][[All, 2]]]; (*Find the σ(B=0)*)
  output= Select[Thread[{ dataB,DataSigma-Sigma0}],
    Abs[#[[1]]]<window&]; (*Output: unfitted [B; σ(B) - σ(B=0)] *)
  output];

SetDirectory[
  "/Users/liangjizhang/Desktop/Data/Halide perovskites/CsSnI3/CsSnI3
    new fitting/Fitting 16mk different contact resistance/"];
Clear[data1,data,data2,str,data0,data4];
allFiles=FileNames["*.txt"];
mm=Length[allFiles];
allData=Import[#,"Table",HeaderLines→15]&/@allFiles; (*Remove the header and description from raw data*)
ListPlot[normdata[allData[[1]], 0.30],PlotRange→Automatic]
data1=Table[0,{ii,1,mm},{i, 1, 3}]; (*Call normdata function and plot [B; σ(B) - σ(B=0)] *)

For[ii=1,ii<mm+1,ii++,
  str=FileBaseName[allFiles[[ii]]];
  data2=normdata[allData[[ii]], 0.29];
  model= (*HLN fitting function*)
   α1 (PolyGamma[1/2+hbar/(4 e Abs[bb] Lfi^2)]-Log[hbar/(4 e Abs[bb] Lfi^2)])+
    offset;
  sol=FindFit[data2,model,{{Lfi, 10^-5}, {α1, -0.2},{offset, -0.1}},
    bb,MaxIterations→10000, Method→"QuasiNewton"];
  data1[[ii,1]]=str;
  data1[[ii,2]]=Lfi/.sol;
  data1[[ii,3]]=(α1*π)/.sol;
  Print[offset/.sol];
  newfile=StringJoin[str,"_fita.txt"];
  FitData=Map[(model/.sol)/.bb→#&,data2[[All,1]]]; (*Apply unfitted [B; σ(B) - σ(B=0)]
                                                    to HLN fitting function*)
  outputdata=Thread[{data2[[All,1]],data2[[All,2]], FitData}];
  Export[newfile, outputdata, "Table"]]; (*Output: Unfitted [B; σ(B) - σ(B=0)]
                                          Fitted [B; σ(B) - σ(B=0)]
                                          L_Φ; α*)
Export["fitdata.txt",data1, "Table"]
```

APPENDIX C

UNLOCKING THE COMPRESSOR

This appendix describes how to unlock the pulse-tube helium compressor (Cryomech CP1000 series, PT415). Throughout operation, overheating may cause the compressor to automatically shut off and turn on several times and eventually lead to the locking of the compressor ("CONTACT FACTORY SYSTEM LOCKOUT 1") as shown in Figure C.1 (b).

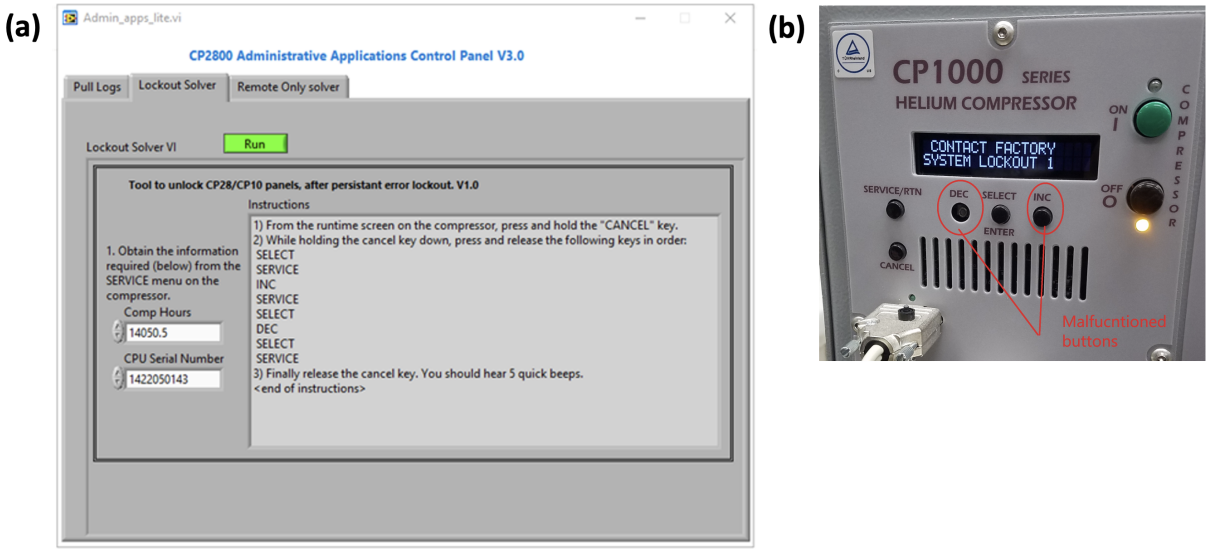

Figure C.1: (a) CP2800 Administrative Application Control Panel V3.0. We need to put compressor hours and CPU series number (**1422050143**) in this panel to get the instructions about unlock the compressor. (b) The front panel of a locked compressor where the malfunctioned buttons are indicated.

To unlock the compressor, we need to first check the compressor hours, which is converted from minutes shown in "Compressor elapsed time" in "Valve Control 4.0.4". The CPU series number of our PT415 compressor is **1422050143**. We can put the CPU series number and compressor hours (with decimal) into "CP2800 Administrative Application Control Panel V3.0" to get the unlock instructions (see Figure C.1 (a)). These instructions show how the compressor can be unlocked by pressing buttons on the front panel of the compressor in a specific order.

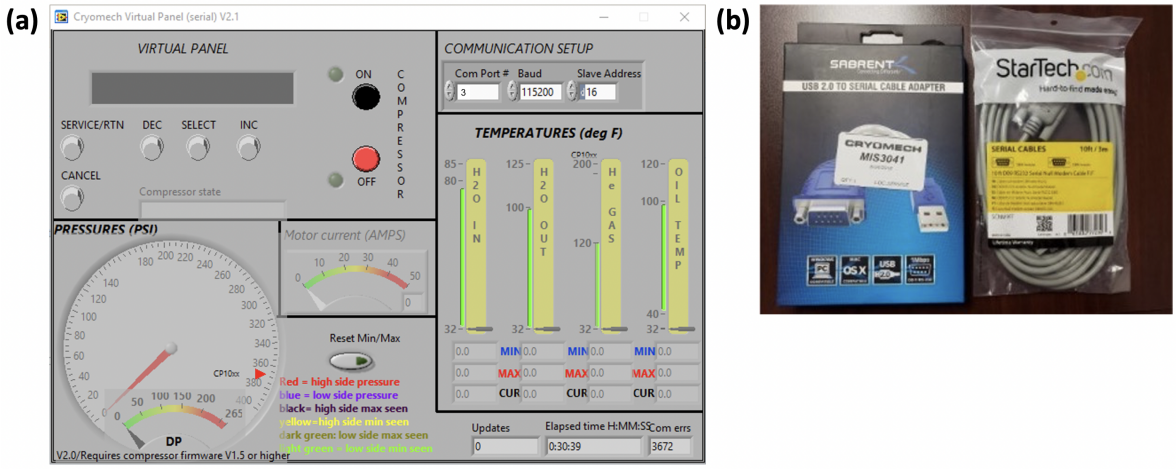

Figure C.2: (a) Cryomech Virtual Panel (serial) V2.1, where the ComPort# is 3, Baud Rate is 115200 and Slave Address is 16. The virtual buttons can be seen from this panel. (b) A null modem cable and the adapter cable.

However, the buttons on the front panel are malfunctioning and broken as shown in Figure C.1 (b). To overcome this issue, we use “Cryomech Virtual Panel (serial) V2.1” to remotely unlock the compressor (see Figure C.2 (a)). To launch this virtual panel, we connect a null modem cable and the adapter (see Figure C.2 (b)) to “RS232 Null Modem port" on the compressor and on a Windows PC. To do so, first disconnect the cable which has already been plugged into the RS232 port on the compressor. Once the compressor is unlocked, the cable can be plugged back. By clicking the virtual buttons on the virtual panel, we can unlock the compressor.

Other important information:

(1) The installation package of CP2800 Administrative Application Control Panel V3.0 shown in Figure C.1 (a) can be downloaded from: “LHQS backups > Liangji Zhang > Unlocking the compressor > Admin_apps_lite_2012.exe”.

(2) The installation package of Cryomech Virtual Panel (serial) V2.1 shown in Figure C.2 (a) can be downloaded from: “LHQS backups > Liangji Zhang > Unlocking the compressor > Control Panel Computer Interface Package > setup_cmapps_public (rev 2009 NOV).exe”. After the installation, there should be a folder created in Windows Startup menu and run **“Virtual Panel"**

(not the "Virtual Panel with login").

(3) The null modem cable and the adapter shown in Figure C.2 (b) are stored in a box (labeled as “How to unlock the compressor”) in the right of the three cabinets in subbasement.

(4) We have an extra compressor motherboard to replace the malfunction one, which is stored in the middle of the three cabinets in subbasement. To get it, one needs to first get the key of this cabinet.

(5) Other important information, such as emails and photocopy of original correspondence with Cryomech can also be found at “LHQS backups > Liangji Zhang > Unlocking the compressor”.

APPENDIX D

MAGNET OPERATION

This appendix provides some important notes about how to properly install and operate the AMI 14T integrated superconducting magnet (other than what have been wirtten in manual), and these notes are the followings:

(1) We need a lifter to load and unload the magnet, the lifter is usually stored in the elevator room in basement.

(2) When loading the magnet onto the 4K interface tube, one should apply sufficient amount of thermal grease (Apiezon N Grease) to the magnet and both side of 4K interface tube. All the bolts connected to the magnet should be firmly tightened.

(3) Connect the temperature sensor and current lead, and tape both of the current leads to 4K interface tube.

(4) The correct order of operating the power supply system of the magnet is the following: First turn on the power supply programmer and wait sufficient time (20 seconds), then turn on the power supply (see Figure 3.5 (b)). Additionally, before turning off the power supply system, one should first turn off the power supply and then power supply programmer.

(5) Before ramping the magnetic field, one should first turn on the persistence switch heater. When measurement is finished and the magnetic field is at zero field, one should first turn off the persistence switch heater and then turn off power supply system.

(6) The way to start ramping the field is as follows: **(i)** Set the target field. **(ii)** Set the ramp rate (SHIFT, then "1", then ▹ or ◃ to check sweep rate of each stage, and use the number keys to change the value of the rate). **(iii)** Pressing RAMP/PAUSE or RAMP TO ZERO.

(7) When magnet is quenched, one should quickly turn off the turbo, open the valve which connects the helium-3 circulation loop and the mixture tank so that all the mixture can go back to tank. Then reset quench (SHIFT, then "3") in order to turn the magnet back to normal.

(8) Do not move anything contains that iron around the magnet when it is in operation, for

example: stool, lock-in and other electronics. Additionally, one should find hard covers for power switches on power supply programmer and for power supply to prevent accidentally turning of the power (and prevent quench).

BIBLIOGRAPHY

BIBLIOGRAPHY

[1] Anderson, P. W. 1958. Absence of diffusion in certain random lattices. *Physical Review* 109(5). 1492.

[2] Andrei, E. Y. 2012. *Two-dimensional electron systems: On helium and other cryogenic substrates*, vol. 19. Springer Science & Business Media.

[3] Ashcroft, N. W. & N. D. Mermin. 1976. Solid state physics.

[4] Baker, A. M. R., J. A. Alexander-Webber, T. Altebaeumer, T. J. B. M. Janssen, A. Tzalenchuk, S. Lara-Avila, S. Kubatkin, R. Yakimova, C. Lin, L. Li & R. J. Nicholas. 2012. Weak localization scattering lengths in epitaxial, and CVD graphene. *Physical Review B* 86(23). 235441.

[5] Bedoya-Pinto, A., J. Malindretos, M. Roever, D. D. Mai & A. Rizzi. 2009. Variable range hopping transport in ferromagnetic GaGdN epitaxial layers. *Physical Review B* 80(19). 195208.

[6] Beenakker, C. W. J. & H. van Houten. 1991. Quantum transport in semiconductor nanostructures. *Solid State Physics* 44. 1–228.

[7] Benmessaoud, I. R., A. Mahul-Mellier, E. Horváth, B. Maco, M. Spina, H. A Lashuel & L. Forró. 2016. Health hazards of methylammonium lead iodide based perovskites: Cytotoxicity studies. *Toxicology Research* 5(2). 407–419.

[8] Bergmann, G. 1982. Inelastic life-time of the conduction electrons in some noble metal films. *Zeitschrift für Physik B Condensed Matter* 48(1). 5–16.

[9] Bergmann, G. 1982. Weak anti-localization — An experimental proof for the destructive interference of rotated spin 1/2. *Solid State Communications* 42(11). 815–817.

[10] Bergmann, G. 1984. Weak localization in thin films: A time-of-flight experiment with conduction electrons. *Physics Reports* 107(1). 1–58.

[11] Bychkov, Y. A. & E. I. Rashba. 1984. Properties of a 2D electron gas with lifted spectral degeneracy. *Journal of Experimental and Theoretical Physics Letters* 39(2). 78–81.

[12] Byeon, Heejun. 2020. *Studying electrons on helium via surface acoustic wave techniques*: Michigan State University dissertation.

[13] Cao, Y., V. Fatemi, S. Fang, K. Watanabe, T. Taniguchi, E. Kaxiras & P. Jarillo-Herrero. 2018. Unconventional superconductivity in magic-angle graphene superlattices. *Nature* 556(7699). 43–50.

[14] Chen, P. 2029. *The growth of organic small molecule and inorganic halide perovskite crystalline thin films*: Michigan State University dissertation.

[15] Chen, Z., J. J. Wang, Y. Ren, C. Yu & K. Shum. 2012. Schottky solar cells based on $CsSnI_3$ thin-films. *Applied Physics Letters* 101(9). 093901.

[16] Chickering, W. E. 2016. *Thermopower in two-dimensional electron systems*. California Institute of Technology.

[17] Cohen, R. E. 1992. Origin of ferroelectricity in perovskite oxides. *Nature* 358(6382). 136–138.

[18] Cotleţ, O., S. Zeytinoğlu, M. Sigrist, E. Demler & A. Imamoğlu. 2016. Superconductivity and other collective phenomena in a hybrid Bose-Fermi mixture formed by a polariton condensate and an electron system in two dimensions. *Physical Review B* 93(5). 054510.

[19] Davies, J. H. 1998. *The physics of low-dimensional semiconductors: An introduction*. Cambridge University Press.

[20] Dean, C. R., A. F. Young, I. Meric, C. Lee, L. Wang, S. Sorgenfrei, P. Kim, K. L. Shepard & J. Hone. 2010. Boron nitride substrates for high-quality graphene electronics. *Nature Nanotechnology* 5(10). 722–726.

[21] Dou, L., Y M. Yang, J. You, Z. Hong, W. Chang, G. Li & Y. Yang. 2014. Solution-processed hybrid perovskite photodetectors with high detectivity. *Nature Communications* 5(1). 1–6.

[22] Dresselhaus, G. 1955. Spin-orbit coupling effects in zinc blende structures. *Physical Review* 100(2). 580.

[23] Drude, P. 1900. Zur elektronentheorie der metalle; ii. teil. galvanomagnetische und thermomagnetische effecte. *Annalen der Physik* 308(11). 369–402.

[24] Efros, A. L. & B. I. Shklovskii. 1975. Coulomb gap and low temperature conductivity of disordered systems. *Journal of Physics C: Solid State Physics* 8(4). L49.

[25] Ehrenreich, H. & D. Turnbull. 1991. *Advances in research and applications: Semiconductor heterostructures and nanostructures*. Academic Press.

[26] Eisenstein, J. P., H. L. Stormer, V. Narayanamurti, A. Y. Cho, A. C. Gossard & C. W. Tu. 1985. Density of states and De Haas—Van Alphen effect in two-dimensional electron systems. *Physical Review Letters* 55(8). 875.

[27] Elias, J. A. & E. A. Henriksen. 2017. Electronic transport and scattering times in tungsten-decorated graphene. *Physical Review B* 95(7). 075405.

[28] Essam, J. W. 1980. Percolation theory. *Reports on Progress in Physics* 43(7). 833.

[29] Faggionato, A. 2017. Mott's law for the critical conductance of Miller-Abrahams random resistor network. *arXiv preprint arXiv:1712.07980* .

[30] Fang, F. F. & P. J. Stiles. 1983. Quantized magnetoresistance in two-dimensional electron systems. *Physical Review B* 27(10). 6487.

[31] Feynman, R. P., A. R. Hibbs & D. F. Styer. 2010. *Quantum mechanics and path integrals*. Courier Corporation.

[32] Feynman, R. P., R. B. Leighton & M. Sands. 1965. *The feynman lectures on physics: Volume III: Quantum mechanics*.

[33] Frohna, K., T. Deshpande, J. Harter, W. Peng, B. A. Barker, J. B. Neaton, S. G. Louie, O. M. Bakr, D. Hsieh & M. Bernardi. 2018. Inversion symmetry and bulk Rashba effect in methylammonium lead iodide perovskite single crystals. *Nature Communications* 9(1). 1–9.

[34] Gantmakher, V. F. & F. R. Gantmacher. 2005. *Electrons and disorder in solids* 130. Oxford University Press.

[35] Geim, A. K. 2009. Graphene: status and prospects. *science* 324(5934). 1530–1534.

[36] Goerbig, M. O. 2009. Quantum Hall effects. *arXiv preprint arXiv:0909.1998* .

[37] Goldman, V. J., M. Santos, M. Shayegan & J. E. Cunningham. 1990. Evidence for two-dimentional quantum Wigner crystal. *Physical Review Letters* 65(17). 2189.

[38] Grätzel, M. 2014. The light and shade of perovskite solar cells. *Nature Materials* 13(9). 838–842.

[39] Groom, C. R., I. J. Bruno, M. P. Lightfoot & S. C. Ward. 2016. The cambridge structural database. *Acta Crystallographica Section B: Structural Science, Crystal Engineering and Materials* 72(2). 171–179.

[40] Gupta, S., T. Bendikov, G. Hodes & D. Cahen. 2016. $CsSnBr_3$, a lead-free halide perovskite for long-term solar cell application: insights on SnF_2 addition. *ACS Energy Letters* 1(5). 1028–1033.

[41] van Hapert, J. J. 2002. *Hopping conduction and chemical structure: A study on silicon suboxides*: University Utrecht dissertation.

[42] Havener, R. W., H. Zhuang, L. Brown, R. G. Hennig & J. Park. 2012. Angle-resolved Raman imaging of interlayer rotations and interactions in twisted bilayer graphene. *Nano Letters* 12(6). 3162–3167.

[43] He, Ho., G. Wang, T. Zhang, I. Sou, G. K. L. Wong, J. Wang, H. Lu, S. Shen & F. Zhang. 2011. Impurity effect on weak antilocalization in the topological insulator Bi_2Te_3. *Physical Review Letters* 106(16). 166805.

[44] Herman, F., C. D. Kuglin, K. F. Cuff & R. L. Kortum. 1963. Relativistic corrections to the band structure of tetrahedrally bonded semiconductors. *Physical Review Letters* 11(12). 541.

[45] Hikami, S., A. I. Larkin & Y. Nagaoka. 1980. Spin-orbit interaction and magnetoresistance in the two dimensional random system. *Progress of Theoretical Physics* 63(2). 707–710.

[46] Hofmann, P. 2015. *Solid state physics: An introduction*. John Wiley & Sons.

[47] Hong, X., S. Cheng, C. Herding & J. Zhu. 2011. Colossal negative magnetoresistance in dilute fluorinated graphene. *Physical Review B* 83(8). 085410.

[48] Hoye, R. L. Z., M. R. Chua, K. P. Musselman, G. Li, M. Lai, Z. Tan, N. C. Greenham, J. L. MacManus-Driscoll, R. H. Friend & D. Credgington. 2015. Enhanced performance in fluorene-free organometal halide perovskite light-emitting diodes using tunable, low electron affinity oxide electron injectors. *Advanced Materials* 27(8). 1414–1419.

[49] Ichimiya, A., P. I. Cohen & P. I. Cohen. 2004. *Reflection high-energy electron diffraction*. Cambridge University Press.

[50] Ioffe, L. B. & B. Z. Spivak. 2013. Giant magnetoresistance in the variable-range hopping regime. *Journal of Experimental and Theoretical Physics* 117(3). 551–569.

[51] Jain, J. K. 2007. *Composite fermions*. Cambridge University Press.

[52] Jiang, H. W., C. E. Johnson & K. L. Wang. 1992. Giant negative magnetoresistance of a degenerate two-dimensional electron gas in the variable-range-hopping regime. *Physical Review B* 46(19). 12830.

[53] Kazim, S., M. K. Nazeeruddin, M. Grätzel & S. Ahmad. 2014. Perovskite as light harvester: A game changer in photovoltaics. *Angewandte Chemie International Edition* 53(11). 2812–2824.

[54] Kepenekian, M. & J. Even. 2017. Rashba and Dresselhaus couplings in halide perovskites: Accomplishments and opportunities for spintronics and spin-orbitronics. *The Journal of Physical Chemistry Letters* 8(14). 3362–3370.

[55] Keshavarz, M., S. Wiedmann, H. Yuan, E. Debroye, M. Roeffaers & J. Hofkens. 2017. Light- and temperature-modulated magneto-transport in organic-inorganic lead halide perovskites. *ACS Energy Letters* 3(1). 39–45.

[56] Ki, D., D. Jeong, J. Choi, H. Lee & K. Park. 2008. Inelastic scattering in a monolayer graphene sheet: A weak-localization study. *Physical Review B* 78(12). 125409.

[57] Kim, K. H., S. Lara-Avila, H. He, H. Kang, S. J. Hong, M. Park, J. Eklöf, K. Moth-Poulsen, S. Matsushita, K. Akagi, S. Kubatkin & Y. W. Park. 2018. Probing variable range hopping lengths by magneto conductance in carbonized polymer nanofibers. *Scientific Reports* 8(1). 1–7.

[58] Kittel, C. & C. Fong. 1963. *Quantum theory of solids*, vol. 5. Wiley New York.

[59] Kittel, C. & P. McEuen. 2018. *Kittel's introduction to solid state physics*. John Wiley & Sons.

[60] Klass, U., W. Dietsche, K Von Klitzing & K. Ploog. 1991. Imaging of the dissipation in quantum-Hall-effect experiments. *Zeitschrift für Physik B Condensed Matter* 82(3). 351–354.

[61] Klitzing, K. V., G. Dorda & M. Pepper. 1980. New method for high-accuracy determination of the fine-structure constant based on quantized Hall resistance. *Physical Review Letters* 45(6). 494.

[62] Kojima, A., K. Teshima, Y. Shirai & T. Miyasaka. 2009. Organometal halide perovskites as visible-light sensitizers for photovoltaic cells. *Journal of the American Chemical Society* 131(17). 6050–6051.

[63] Kozuka, Y., A. Tsukazaki, D. Maryenko, J. Falson, S. Akasaka, K. Nakahara, S. Nakamura, S. Awaji, K. Ueno & M. Kawasaki. 2011. Insulating phase of a two-dimensional electron gas in $Mg_xZn_{1-x}O$/ZnO heterostructures below $\nu = \frac{1}{3}$. *Physical Review B* 84(3). 033304.

[64] Kumar, M. H., S. Dharani, W. L. Leong, P. P. Boix, R. R. Prabhakar, T. Baikie, C. Shi, H. Ding, Ra. Ramesh, M. Asta, M. Graetzel, S. G. Mhaisalkar & N. Mathews. 2014. Lead-free halide perovskite solar cells with high photocurrents realized through vacancy modulation. *Advanced Materials* 26(41). 7122–7127.

[65] Laiko, E. .I, A. O. Orlov, A. K. Savchenko, E. A. Il'ichev & E. A. Poltoratskii. 1987. Negative magnetoresistance and oscillations of the hopping conductance of a short n-type channel in a GaAs field-effect transistor. *Journal of Experimental and Theoretical Physics* 66. 1258.

[66] Landau, L. D. & E. M. Lifshitz. 2013. *Quantum mechanics: Non-relativistic theory*, vol. 3. Elsevier.

[67] Lane, J. R. 2021. *Integrating superconducting qubits with quantum fluids and surface acoustic wave devices*: Michigan State University dissertation.

[68] Lane, J. R., L. Zhang, M. A. Khasawneh, B. N. Zhou, E. A. Henriksen & J. Pollanen. 2018. Flip-chip gate-tunable acoustoelectric effect in graphene. *Journal of Applied Physics* 124(19). 194302.

[69] Lang, M., L. He, X. Kou, P. Upadhyaya, Y. Fan, H. Chu, Y. Jiang, J. H. Bardarson, W. Jiang, E. S. Choi, Y. Wang, N. Yeh, J. Moore & K. L. Wang. 2013. Competing weak localization and weak antilocalization in ultrathin topological insulators. *Nano Letters* 13(1). 48–53.

[70] Laughlin, R. B. 1983. Anomalous quantum Hall effect: An incompressible quantum fluid with fractionally charged excitations. *Physical Review Letters* 50(18). 1395.

[71] Lee, P. A & T. V. Ramakrishnan. 1985. Disordered electronic systems. *Reviews of Modern Physics* 57(2). 287.

[72] Lee, P. A. & A. D. Stone. 1985. Universal conductance fluctuations in metals. *Physical Review Letters* 55(15). 1622.

[73] Li, JIA, C. Tan, S. Chen, Y. Zeng, T. Taniguchi, K. Watanabe, J. Hone & C. R. Dean. 2017. Even-denominator fractional quantum Hall states in bilayer graphene. *Science* 358(6363). 648–652.

[74] Li, JIA, T. Taniguchi, K. Watanabe, J. Hone & C. R. Dean. 2017. Excitonic superfluid phase in double bilayer graphene. *Nature Physics* 13(8). 751–755.

[75] Liang, Y., X. Cui, F. Li, C. Stampfl, S. P. Ringer & R. Zheng. 2021. Electrode-induced impurities in tin halide perovskite solar cell material $CsSnBr_3$ from first principles. *npj Computational Materials* 7(1). 1–9.

[76] Lifshitz, I. M. & V. Kirpichenkov. 1979. Tunnel transparency of disordered systems. *Journal of Experimental and Theoretical Physics* 77(3). 989–1016.

[77] Lin, J. & J. P. Bird. 2002. Recent experimental studies of electron dephasing in metal and semiconductor mesoscopic structures. *Journal of Physics: Condensed Matter* 14(18). R501.

[78] Liu, M., J. Zhang, C. Chang, Z. Zhang, X. Feng, K. Li, K. He, L. Wang, X. Chen, X. Dai, Z. Fang, Q. Xue, X. Ma & Y. Wang. 2012. Crossover between weak antilocalization and weak localization in a magnetically doped topological insulator. *Physical Review Letters* 108(3). 036805.

[79] López-Fraguas, E., S. Masi & I. Mora-Seró. 2019. Optical characterization of lead-free Cs_2SnI_6 double perovskite fabricated from degraded and reconstructed $CsSnI_3$ films. *ACS Applied Energy Materials* 2(12). 8381–8387.

[80] Lu, H. & S. Shen. 2014. Weak localization and weak anti-localization in topological insulators. In *Spintronics vii*, vol. 9167, 91672. International Society for Optics and Photonics.

[81] Lyon, T. J., J. Sichau, A. Dorn, A. Centeno, A. Pesquera, A. Zurutuza & R. H. Blick. 2017. Probing electron spin resonance in monolayer graphene. *Physical Peview Letters* 119(6). 066802.

[82] Mailly, D. 1987. Weak localization and interaction corrections in microstrips of GaAs. *Europhysics Letters* 4(10). 1171.

[83] Manchon, A., H. C. Koo, J. Nitta, S. M. Frolov & R. A. Duine. 2015. New perspectives for Rashba spin-orbit coupling. *Nature Materials* 14(9). 871–882.

[84] Mani, R. G, J. Hankinson, C. Berger & W. A. De Heer. 2012. Observation of resistively detected hole spin resonance and zero-field pseudo-spin splitting in epitaxial graphene. *Nature Communications* 3(1). 1–6.

[85] Mani, R. G., J. H. Smet, K. von Klitzing, V. Narayanamurti, W. B. Johnson & V. Umansky. 2002. Zero-resistance states induced by electromagnetic-wave excitation in GaAs/AlGaAs heterostructures. *Nature* 420(6916). 646–650.

[86] McCann, E. & M. Koshino. 2013. The electronic properties of bilayer graphene. *Reports on Progress in Physics* 76(5). 056503.

[87] Medina, E., M. Kardar, Y. Shapir & X. Wang. 1990. Magnetic-field effects on strongly localized electrons. *Physical Review Letters* 64(15). 1816.

[88] Miller, A. & E. Abrahams. 1960. Impurity conduction at low concentrations. *Physical Review* 120(3). 745.

[89] Milliken, F. P. & Z. Ovadyahu. 1990. Observation of conductance fluctuations in large In_2O_{3-x} films. *Physical Review Letters* 65(7). 911.

[90] Mitin, V. F., V. K. Dugaev & G. G. Ihas. 2007. Large negative magnetoresistance in Ge films at ultralow temperatures and low magnetic fields. *Applied Physics Letters* 91(20). 202107.

[91] Mori, M. & H. Saito. 1986. An x-ray study of successive phase transitions in $CsSnBr_3$. *Journal of Physics C: Solid State Physics* 19(14). 2391.

[92] Mott, N. F. 1968. Conduction in glasses containing transition metal ions. *Journal of Non-Crystalline Solids* 1(1). 1–17.

[93] Nagai, H. 1974. Structure of vapor-deposited $Ga_xIn_{1-x}As$ crystals. *Journal of Applied Physics* 45(9). 3789–3794.

[94] Nasyedkin, K., I. King, L. Zhang, P. Chen, L. Wang, R. J. Staples, R. R. Lunt & J. Pollanen. 2021. Extraordinary phase coherence length in epitaxial halide perovskites. *iScience* 24(8). 102912.

[95] Neamen, D. A. 2003. *Semiconductor physics and devices: Basic principles*. McGraw-hill.

[96] Neto, A. H. C., F. Guinea, N. M. R. Peres, K. S. Novoselov & A. K. Geim. 2009. The electronic properties of graphene. *Reviews of Modern Physics* 81(1). 109.

[97] Nguyen, V. L., B. Z. Spivak & B. I. Shklovskii. 1985. Tunnel hopping in disordered systems. *Journal of Experimental and Theoretical Physics* 62(5). 1021–1029.

[98] Nguyen, V. L., B. Z. Spivak & B. I. Shklovskii. 1986. Hopping-conductivity fluctuations in small samples. *Journal of Experimental and Theoretical Physics* 43(1). 35.

[99] Nyguen, V. L. 1984. Two-dimensional hopping conduction in a magnetic field. *Soviet Physics Semiconductors* 18(2). 207–210.

[100] Ohtomo, A. & H. Y. Hwang. 2004. A high-mobility electron gas at the $LaAlO_3/SrTiO_3$ heterointerface. *Nature* 427(6973). 423–426.

[101] Peedikakkandy, L. & P. Bhargava. 2016. Composition dependent optical, structural and photoluminescence characteristics of cesium tin halide perovskites. *Rsc Advances* 6(24). 19857–19860.

[102] Percher, I. M. 2018. *2d mott hopping of vortices in an amorphous indium oxide film*: University of Minnesota dissertation.

[103] Peshkin, M. & A. Tonomura. 1989. *The Aharonov-Bohm effect*, vol. 340. Springer.

[104] Pobell, F. 2007. *Matter and methods at low temperatures*, vol. 2. Springer.

[105] Pollak, M. & I. Riess. 1976. A percolation treatment of high-field hopping transport. *Journal of Physics C: Solid State Physics* 9(12). 2339.

[106] Protesescu, L., S. Yakunin, M. I. Bodnarchuk, F. Krieg, R. Caputo, C. H. Hendon, R. X. Yang, A. Walsh & M. V. Kovalenko. 2015. Nanocrystals of cesium lead halide perovskites ($CsPbX_3$, X=Cl, Br, and I): Novel optoelectronic materials showing bright emission with wide color gamut. *Nano letters* 15(6). 3692–3696.

[107] Reyren, N., S. Thiel, A. D. Caviglia, L. F. Kourkoutis, G. Hammerl, C. Richter, C. W. Schneider, T. Kopp, A. Rüetschi, D. Jaccard, M. Gabay, D. A. Muller, J. M. Triscone & J. Mannhart. 2007. Superconducting interfaces between insulating oxides. *Science* 317(5842). 1196–1199.

[108] Rntzsch, R., I. S. Slimak & H. Brger. 1979. Hopping conductivity of undoped ZnSe thin films. *Physica Status Solidi (a)* 54(2). 487–492.

[109] Russell, P. A., F. F. Ouali, N. P. Hewett & L. J. Challis. 1990. Power dissipation in the quantum Hall regime. *Surface Science* 229(1-3). 54–56.

[110] Sabba, D., M. H. Kumar, L. H. Wong, J. Barber, M. Gratzel & N. Mathews. 2015. Perovskite–hematite tandem cells for efficient overall solar driven water splitting. *Nano Letters* 15(6). 3833–3839.

[111] Schubert, E. F. 2015. *Physical foundations of solid-state devices*. E. Fred Schubert.

[112] Schultz, I. 2015. *Electrical conduction and magnetoresistance of silver-stannic oxide composite nanotubes*: Texas A&M University dissertation.

[113] Shklovskii, B. I. & A. L. Efros. 2013. *Electronic properties of doped semiconductors*, vol. 45. Springer Science & Business Media.

[114] Shklovskii, B. I. & B. Z. Spivak. 1991. Scattering and interference effects in variable range hopping. *Hopping Transport in Solids* 28. 271.

[115] Shklovskii, B. I. & B. Z. Spivak. 1991. Scattering and interference effects in variable range hopping conduction. In *Hopping transport in solids*, vol. 28 Modern Problems in Condensed Matter Sciences, 271–348. Elsevier. doi:https://doi.org/10.1016/B978-0-444-88037-6.50015-4. https://www.sciencedirect.com/science/article/pii/B9780444880376500154.

[116] Skachko, I., X. Du, F. Duerr, A. Luican, D. A. Abanin, L. S. Levitov & E. Y. Andrei. 2010. Fractional quantum Hall effect in suspended graphene probed with two-terminal measurements. *Philosophical Transactions of the Royal Society A: Mathematical, Physical and Engineering Sciences* 368(1932). 5403–5416.

[117] Skall, A. S. & B. I. Shklovsky. 1974. Mott equation for low temperature edge conductivity. *Soviet Physics-Solid State* 16(6). 1190.

[118] Stormer, H. L. 1999. Nobel lecture: The fractional quantum Hall effect. *Reviews of Modern Physics* 71(4). 875.

[119] Sun, Z., B. Cai, X. Chen, W. Wei, X. Li, D. Yang, C. Meng, Y. Wu & H. Zeng. 2020. Prediction and observation of defect-induced room-temperature ferromagnetism in halide perovskites. *Journal of Semiconductors* 41(12). 122501.

[120] Sutherland, B. R., S. Hoogland, M. M. Adachi, C. T. Wong & E. H. Sargent. 2014. Conformal organohalide perovskites enable lasing on spherical resonators. *ACS nano* 8(10). 10947–10952.

[121] Tikhonenko, F. V., D. W. Horsell, R. V. Gorbachev & A. K. Savchenko. 2008. Weak localization in graphene flakes. *Physical Review Letters* 100(5). 056802.

[122] Tong, D. 2016. Lectures on the quantum Hall effect. *arXiv preprint arXiv:1606.06687* .

[123] Tracy, L. A. 2008. *Studies of two dimensional electron systems via surface acoustic waves and nuclear magnetic resonance techniques*: California Institute of Technology dissertation.

[124] Tsui, D. C., H. L. Stormer & A. C. Gossard. 1982. Two-dimensional magnetotransport in the extreme quantum limit. *Physical Review Letters* 48(22). 1559.

[125] Von K., K. 1986. The quantized Hall effect. *Reviews of Modern Physics* 58(3). 519.

[126] Wang, L., P. Chen, P. S. Kuttipillai, I. King, R. Staples, K. Sun & R. R. Lunt. 2019. Epitaxial stabilization of tetragonal cesium tin iodide. *ACS applied materials & interfaces* 11(35). 32076–32083.

[127] Wang, L., P. Chen, N. Thongprong, M. Young, P. S. Kuttipillai, C. Jiang, P. Zhang, K. Sun, P. M. Duxbury & R. R. Lunt. 2017. Unlocking the single-domain epitaxy of halide perovskites. *Advanced Materials Interfaces* 4(22). 1701003.

[128] Wang, L., I. Meric, P. Y. Huang, Q. Gao, Y. Gao, H. Tran, T. Taniguchi, K. Watanabe, L. M. Campos, D. A. Muller, J. Gun, P. Kim, J. Hone, K. L. Shepard & C. R. Dean. 2013. One-dimensional electrical contact to a two-dimensional material. *Science* 342(6158). 614–617.

[129] Wang, Y., X. Li, J. Song, L. Xiao, H. Zeng & H. Sun. 2015. All-inorganic colloidal perovskite quantum dots: A new class of lasing materials with favorable characteristics. *Advanced Materials* 27(44). 7101–7108.

[130] Wang, Y., X. Sun, Z. Chen, Y. Sun, S. Zhang, T. Lu, E. Wertz & J. Shi. 2017. High-temperature ionic epitaxy of halide perovskite thin film and the hidden carrier dynamics. *Advanced Materials* 29(35). 1702643.

[131] Wang, Y., Z. Wan, Q. Qian, Y. Liu, Z. Kang, Z. Fan, P. Wang, Y. Wang, C. Li, C. Jia, Z. Lin, J. Guo, I. Shakir, M. Goorsky, X. Duan, Y. Zhang, Y. Huang & X. Duan. 2020. Probing photoelectrical transport in lead halide perovskites with van der Waals contacts. *Nature Nanotechnology* 15(9). 768–775.

[132] Waser, R. 2008. *Nanotechnology: volume 3: Information technology i*. John Wiley & Sons.

[133] Yun, Y., Y. Ma, S. Tao, W. Xing, Y. Chen, T. Su, W. Yuan, J. Wei, X. Lin, Q. Niu, X. C. Xie & W. Han. 2017. Observation of long phase-coherence length in epitaxial La-doped CdO thin films. *Physical Review B* 96(24). 245310.

[134] Zabrodskii, A. & K. Zinov'eva. 1984. Low-temperature conductivity and metal-insulator transition in compensate n-Ge. *Journal of Experimental and Theoretical Physics* 86(2). 727–742.

[135] Zhang, L., I. King, K. Nasyedkin, P. Chen, B. Skinner, R. R. Lunt & J. Pollanen. 2021. Coherent hopping transport and giant negative magnetoresistance in epitaxial $CsSnBr_3$. *ACS Applied Electronic Materials* 3(7). 2948–2952.

[136] Zhang, X., Q. Liu, J. Luo, A. J. Freeman & A. Zunger. 2014. Hidden spin polarization in inversion-symmetric bulk crystals. *Nature Physics* 10(5). 387–393.

[137] Zhao, H., B. Z. Spivak, M. P. Gelfand & S. Feng. 1991. Negative magnetoresistance in variable-range-hopping conduction. *Physical Review B* 44(19). 10760.